

Exact numerical and analytical results  
for correlated lattice electrons  
in one dimension

Dissertation

zur Erlangung des  
Doktorgrades der Naturwissenschaften  
(Dr. rer. nat.)  
dem Fachbereich Physik  
der Philipps-Universität Marburg  
vorgelegt von

Satoshi Ejima  
aus Chiba, Japan



Marburg an der Lahn, Februar 2006



Exakte numerische und analytische Ergebnisse  
für korrelierte Elektronen  
in einer Dimension

Dissertation

zur Erlangung des  
Doktorgrades der Naturwissenschaften  
(Dr. rer. nat.)  
dem Fachbereich Physik  
der Philipps-Universität Marburg  
vorgelegt von

Satoshi Ejima  
aus Chiba, Japan



Marburg an der Lahn, Februar 2006

Vom Fachbereich Physik der Philipps-Universität Marburg  
als Dissertation angenommen am: 20.03.2006

Erstgutachter: Prof. Dr. F. Gebhard  
Zweitgutachter: Prof. Dr. P. Thomas

Tag der mündlichen Prüfung: 30.03.2006

## Zusammenfassung

Seit der Entdeckung der Hochtemperatur-Supraleitung in Kupratverbindungen im Jahr 1986 sind die stark korrelierten Elektronensysteme eines der wichtigsten Forschungsgebiete der theoretischen Festkörperphysik. Diese Kupratmaterialien bestehen aus stark anisotropen, quasi-zweidimensionalen Kupferoxidschichten. Daher sind niedrigdimensionale Elektronensysteme in das Zentrum der theoretischen Aufmerksamkeit gerückt. Insbesondere in eindimensionalen Modellen kann man exakte analytische und numerische Ergebnisse erlangen, die ein umfassendes und tiefes Verständnis der korrelierten Vielteilchensysteme erlauben.

Im ersten Teil dieser Arbeit verwenden wir exakte numerische Methoden, um die Eigenschaften der Tomonaga–Luttinger Flüssigkeit zu untersuchen, welche den generischen metallischen Zustand in einer Dimension darstellt. Numerische Methoden dieser Untersuchung sind die *Exakte Diagonalisierung* und die *Dichtematrix-Renormierungsgruppe*. Insbesondere untersuchen wir, wie sich der sogenannte Tomonaga–Luttinger Exponent  $K_\rho$  gewinnen läßt, durch den der kritische Exponent  $\alpha$  bestimmt werden kann. Dieser Exponent beschreibt das Verhalten der lokalen Zustandsdichte an der Fermikante. Einige dieser Experimente liefern  $\alpha \gtrsim 1$  bzw.  $K_\rho \lesssim 0.17$ , was sich nicht mit  $\alpha_H \lesssim 1/8$  bzw.  $K_\rho^H \geq 0.5$  im eindimensionalen Hubbard Modell vereinbaren läßt. In dieser Arbeit entwickeln wir neue numerische Zugänge, um  $K_\rho$  zu bestimmen, und erklären, wie man die kleinen experimentellen Werte theoretisch durch schwache Dotierung von Ladungsdichtewelle-Isolatoren erreichen kann.

Im zweiten Teil dieser Arbeit untersuchen wir das Hubbard Modell mit dem analytisch exakten *Thermodynamischen Bethe Ansatz* in einem Parameterbereich, der die Bewegung von Ladungen in einem ungeordnetem Spinhintergrund beschreibt. Die Temperatur muß dazu groß sein im Vergleich zu der charakteristischen Energieskala für magnetische Anregungen und zugleich klein gegenüber der Mott-Lücke. Diese Untersuchung wird durch die bestehende Kontroverse über den Mott–Hubbard Übergang in unendlichen Dimensionen motiviert, wo der Grundzustand ebenfalls Spinunordnung aufweist. Die kritische Wechselwirkung  $U_c$ , bei der sich die Mott–Hubbard Lücke schließt, ist bis heute nicht zuverlässig bekannt. Es ist daher eine Aufgabe dieser Arbeit, ein Beispiel für ein spinungeordnetes Hubbard Modell zu untersuchen, das exakt gelöst werden kann. Die thermodynamischen Eigenschaften dieses Modells werden durch Ladungsanregungen beschrieben, die eine effektive Dispersion und eine endliche Lücke aufweisen. Diese Anregungen sind von den Spinfreiheitsgraden entkoppelt, die ihrerseits nur einen entropischen Beitrag zur Thermodynamik des Systems liefern. Dieses Szenario läßt sich durch ein hypothetisches wechselwirkendes Elektronensystem am Temperatur-Nullpunkt interpretieren, bei dem der Metall–Isolator Übergang bei endlicher Wechselwirkungsstärke erfolgt, oberhalb derer sich die Lücke linear öffnet. Unsere exakten Resultate weisen darauf hin, daß eine Entwicklung der Grundzustandsenergie bei starker Kopplung nicht geeignet ist, um  $U_c$  zu bestimmen. Verwendet man hingegen eine Entwicklung der Einteilchenlücke, so erhält man eine gute Extrapolation für die kritische Kopplung.



## Abstract

Since the advent of high- $T_c$  cuprate superconductors in 1986, strongly correlated electron systems have attracted much attention. Since the cuprates are essentially two-dimensional, low-dimensional systems have moved into the focus of condensed-matter theory. From a theoretical point of view, one-dimensional systems are of particular interest because there are exact numerical and analytical methods which permit detailed studies and deep insights into the many-body problem.

In the first part of this thesis, using the numerically exact methods *Exact Diagonalization* and the *Density-Matrix Renormalization Group* (DMRG), we investigate the properties of the Tomonaga–Luttinger liquid which is the generic metallic state of matter in one dimension. In particular, we concentrate on the investigation of the so-called Tomonaga–Luttinger liquid parameter  $K_\rho$  which determines the critical exponent  $\alpha$  for the density of states near the Fermi energy. Experimental results for some quasi one-dimensional materials report  $\alpha \gtrsim 1$ , which would imply  $K_\rho \lesssim 0.17$ , a value which cannot be reconciled with the bare Hubbard model where  $K_\rho \geq 0.5$ , i.e.,  $\alpha_H \leq 1/8$ . We develop new accurate numerical methods to obtain  $K_\rho$  and investigate how to obtain such small values for  $K_\rho$  for slightly doped charge-density-wave insulators.

In the second part of this thesis, using the *Thermodynamic Bethe Ansatz* (TBA) as exact analytical method, we investigate the one-dimensional Hubbard model in the spin-disordered regime, which is characterized by the temperature being much larger than the magnetic energy scale but small compared to the Mott–Hubbard gap. Our study is motivated by the controversy about the Mott–Hubbard insulator in infinite dimensions whose ground state is also spin-disordered. In this system the determination of the precise value of the critical interaction strength  $U_c$  where the Mott–Hubbard gap closes is still unsolved. Therefore, we provide an example of a Hubbard-type model with a disordered spin background which can be solved exactly. The thermodynamics of our model can be understood in terms of gapped charged excitations with an effective dispersion which are decoupled from the spin degrees of freedom; the latter contribute only entropically. An interpretation of this regime in terms of a putative interacting-electron system at zero temperature leads to a metal-insulator transition at a finite interaction strength above which the gap opens linearly. Our exact results indicate that the strong-coupling expansion of the ground-state energy cannot be used to locate  $U_c$ . However, the strong-coupling expansion of the gap permits a reliable extrapolation of the critical interaction strength.



# Contents

<b>1</b>	<b>Introduction</b>	<b>1</b>
1.1	Why are we interested in correlated electrons in one dimension? . . . . .	1
1.2	Outline of the thesis . . . . .	2
1.3	Related publications . . . . .	3
<b>I</b>	<b>Solution of the <math>K_\rho</math>-problem</b>	<b>5</b>
<b>2</b>	<b>Correlated electrons in one dimension</b>	<b>7</b>
2.1	Models for lattice electrons . . . . .	7
2.1.1	Hubbard model . . . . .	7
2.1.2	Extended Hubbard model . . . . .	9
2.1.3	(Extended) Peierls–Hubbard model . . . . .	10
2.2	Luttinger liquids . . . . .	10
2.2.1	Generic properties . . . . .	11
2.2.2	Correlation functions . . . . .	15
2.2.3	Commensurabilities . . . . .	16
2.3	Experimental results . . . . .	18
2.3.1	Metallic single-wall carbon nanotubes . . . . .	18
2.3.2	Bechgaard salts . . . . .	19
2.3.3	TTF-TCNQ . . . . .	20
<b>3</b>	<b>Numerical methods</b>	<b>23</b>
3.1	Exact Diagonalization (ED): Lanczos method . . . . .	23
3.2	Density-Matrix Renormalization Group (DMRG) . . . . .	24
3.2.1	Density matrix projection . . . . .	25
3.2.2	DMRG algorithms . . . . .	27
3.2.3	Measurements . . . . .	29
3.3	Summary . . . . .	29
<b>4</b>	<b>Critical exponents from combined ED and DMRG</b>	<b>31</b>
4.1	Defining equations . . . . .	31
4.1.1	Charge velocity and compressibility . . . . .	31
4.1.2	Drude weight . . . . .	33
4.1.3	Summary . . . . .	33
4.2	Application to the $t$ - $U$ - $V_1$ - $V_2$ model . . . . .	33
4.2.1	Phase diagram at quarter filling . . . . .	33
4.2.2	Absence of a tricritical point . . . . .	36
4.2.3	Spin gap . . . . .	37
4.2.4	Summary . . . . .	37

<b>5</b>	<b>Critical exponents from DMRG</b>	<b>39</b>
5.1	Defining equations and tests . . . . .	39
5.1.1	Density-density correlation function . . . . .	39
5.1.2	Infinitesimal doping . . . . .	40
5.1.3	Comparison with exact results for the Hubbard model for all fillings	41
5.1.4	Comparison with exact results for spinless fermions . . . . .	42
5.1.5	Summary . . . . .	42
5.2	Application to the $t$ - $U$ - $V$ model . . . . .	43
5.2.1	Spinless fermions with nearest-neighbor repulsion . . . . .	44
5.2.2	Comparison with field theory . . . . .	45
5.2.3	Phase diagram at quarter filling . . . . .	45
5.2.4	Doped Mott insulator . . . . .	46
5.2.5	Summary . . . . .	47
5.3	Application to the $t$ - $U$ - $V_1$ - $V_2$ model . . . . .	47
5.3.1	Commensurate filling . . . . .	48
5.3.2	Infinitesimal doping . . . . .	48
5.3.3	Summary . . . . .	49
5.4	Application to the Peierls–Hubbard model . . . . .	49
5.4.1	Comparison with field theory . . . . .	50
5.4.2	Effect of dimerization on $K_\rho$ . . . . .	51
5.4.3	Summary . . . . .	53
<b>6</b>	<b>Conclusions</b>	<b>55</b>
<b>II</b>	<b>Charges in a spin-disordered background</b>	<b>57</b>
<b>7</b>	<b>Motivation: disordered spin background</b>	<b>59</b>
7.1	Mott–Hubbard insulator in infinite dimensions . . . . .	59
7.1.1	Dynamical Mean-Field Theory (DMFT) . . . . .	59
7.1.2	Ground-state properties . . . . .	61
7.1.3	Mott–Hubbard transitions . . . . .	63
7.2	Exact results for the Harris–Lange model . . . . .	65
7.2.1	Hamiltonian . . . . .	65
7.2.2	Optical absorption and optical conductivity in an array of chains . .	66
7.2.3	Optical absorption in the Harris–Lange model . . . . .	67
<b>8</b>	<b>Thermodynamic Bethe ansatz equations</b>	<b>69</b>
8.1	Lieb–Wu equations for the one-dimensional Hubbard model . . . . .	69
8.1.1	Ground-state energy at half band-filling . . . . .	71
8.1.2	Mott transition at zero temperature . . . . .	72
8.2	Takahashi equations . . . . .	73
8.2.1	String hypothesis . . . . .	74
8.2.2	Setup of the Takahashi equations . . . . .	75
8.3	Thermodynamic Bethe Ansatz (TBA) equations . . . . .	77
8.4	Ha’s solution to lowest order . . . . .	82

<b>9</b>	<b>Solution in the spin-disordered limit</b>	<b>85</b>
9.1	Defining equations . . . . .	85
9.1.1	Definition of the limit . . . . .	85
9.1.2	Dressed energy of the charge degrees of freedom . . . . .	88
9.1.3	Dressed momentum of the charge degrees of freedom . . . . .	89
9.1.4	Effective dispersion for strong coupling . . . . .	90
9.1.5	Internal energy . . . . .	93
9.2	Zero-temperature interpretation . . . . .	94
9.2.1	Mott–Hubbard transition . . . . .	94
9.2.2	Average double occupancy . . . . .	95
9.2.3	Strong-coupling expansions . . . . .	95
<b>10</b>	<b>Conclusions</b>	<b>99</b>
<b>11</b>	<b>Summary and Outlook</b>	<b>101</b>
11.1	Summary . . . . .	101
11.2	Outlook . . . . .	101
11.2.1	$K_\rho$ -problem . . . . .	101
11.2.2	Charges in a spin-disordered system . . . . .	102
<b>A</b>	<b>Mathematical Appendices</b>	<b>103</b>
A.1	Symmetric integration . . . . .	103
A.2	Fourier transforms . . . . .	103
A.3	Identities involving the integral kernels . . . . .	103
A.4	Bessel functions . . . . .	104
A.5	Useful relations . . . . .	104
A.6	$k$ - $\Lambda$ string for two electrons . . . . .	104
	<b>Bibliography</b>	<b>107</b>
	<b>Danksagung</b>	<b>113</b>
	<b>Curriculum Vitae</b>	<b>115</b>



## List of Figures

2.1	Schematic representation of charge-density-wave states at various fillings. . . . .	9
2.2	Scattering processes in a one-dimensional electron gas. . . . .	13
2.3	Schematic representation of Mott insulators for commensurate densities. . . . .	17
2.4	Photoemission spectra of single-wall carbon nanotubes near the Fermi energy. . . . .	18
2.5	Frequency dependence of the conductivity in (TMTSF) <sub>2</sub> X salts. . . . .	19
2.6	Temperature dependence of the photoemission spectra of TTF-TCNQ. . . . .	20
3.1	Schematic representation of superblock. . . . .	25
3.2	Superblock configuration for the DMRG infinite-system algorithm. . . . .	27
3.3	Schematic representation of the DMRG infinite-system algorithm. . . . .	28
3.4	Schematic representation of the DMRG finite-system algorithm. . . . .	29
4.1	Scaling of the inverse compressibility and of the charge velocity in the $t$ - $U$ - $V_1$ - $V_2$ model. . . . .	32
4.2	Charge gap $\Delta_c$ and Tomonaga–Luttinger parameter $K_\rho$ for the $t$ - $U$ - $V_1$ - $V_2$ model at quarter filling. . . . .	34
4.3	Phase diagram of the one-dimensional $t$ - $U$ - $V_1$ - $V_2$ model. . . . .	35
4.4	Tomonaga–Luttinger parameter $K_\rho$ for the $t$ - $U$ - $V_1$ - $V_2$ model at quarter filling as a function of $V_1 = 2V_2$ . . . . .	35
4.5	Charge gap for spinless fermions at $V_1/t = 20$ and $V_1/t = 40$ . . . . .	36
5.1	$K_\rho$ for the infinitesimally doped Mott–Hubbard insulator. . . . .	41
5.2	$K_\rho(L)$ as a function of the inverse system size and $K_\rho$ as a function of the density for the Hubbard model. . . . .	42
5.3	$K_\rho$ for the $t$ - $U$ - $V$ model at $U/t = \infty$ , $V \leq 2t$ . . . . .	43
5.4	$K_\rho$ in the slightly doped Mott insulator ( $n \simeq 1/2$ ) for spinless fermions. . . . .	44
5.5	$K_\rho$ for the $t$ - $U$ - $V$ model at quarter filling in comparison with $g$ -ology and functional renormalization group methods. . . . .	45
5.6	Contour map for $K_\rho$ in the $U$ - $V$ plane for the $t$ - $U$ - $V$ model at quarter filling. . . . .	46
5.7	$K_\rho$ for the $t$ - $U$ - $V$ model as a function of $V/t$ at filling $n = 11/24$ . . . . .	47
5.8	Charge gap $\Delta_c$ and $K_\rho$ for the $t$ - $U$ - $V_1$ - $V_2$ model at $n_c = 1/3$ . . . . .	48
5.9	$K_\rho(L)$ for the infinitesimally doped Mott–Hubbard insulator at $n_c = 1/3$ . . . . .	49
5.10	$K_\rho$ for the Peierls–Hubbard model (PHM) from the DMRG and $g$ -ology. . . . .	50
5.11	$K_\rho$ for the PHM for various dimerizations. . . . .	52
5.12	Comparison of $K_\rho$ for the PHM and the reduced single-band Hubbard model. . . . .	53
7.1	Star geometry for the single-impurity Anderson model. . . . .	60
7.2	Ground-state energy of the Mott–Hubbard insulator in infinite dimensions . . . . .	62
7.3	Average double occupancy of the Mott–Hubbard insulator in infinite dimensions . . . . .	62

7.4	Single-particle gap of the Mott insulator in infinite dimensions . . . . .	64
7.5	Band structure of the Harris–Lange model . . . . .	66
7.6	Optical conductivity in the Harris–Lange model . . . . .	68
8.1	Mott–Hubbard gap for the one-dimensional Hubbard model at half filling . .	72
9.1	Internal energy for the Hubbard model at half band-filling and large inter- actions. . . . .	86
9.2	Density of states of the lower Hubbard band in the spin-disordered regime.	92
9.3	Single-particle gap for the putative interacting-electron system with a dis- ordered spin background. . . . .	95
9.4	Average double occupancy for the putative interacting-electron system with a spin-disordered background. . . . .	96

# 1 Introduction

## 1.1 Why are we interested in correlated electrons in one dimension?

When we look at the order of magnitude of the Coulomb interaction in solids, we notice that it is neither dominant nor negligible compared to the kinetic energy. This makes interactions so difficult to treat. However, the effects of interactions in three-dimensional systems have been successfully explained by Landau's Fermi liquid theory. In a Fermi gas the occupation number of a state has a *discontinuity* at the Fermi surface, whose amplitude is unity. Surprisingly, as interactions are switched on in the system, its properties remain qualitatively similar to those of the non-interacting system. The elementary single-particle excitations are the so-called *quasiparticles*, i.e., electrons dressed by the density fluctuations around them. The occupation number still has a discontinuity at the Fermi energy but with an amplitude smaller than unity.

How much of this successful Fermi liquid theory survives in one dimension? We can easily see that interactions have more drastic effects as compared to higher dimensions: in one dimension, due to the restricted geometry, an electron that propagates pushes all its neighbors because of the electron-electron interactions. In other words, no individual motion is possible in one dimension, and only collective excitations remain. This is the essential difference between one-dimensional and higher-dimensional systems.

The physical properties of the one-dimensional electron gas are indeed drastically different from the ones of a free electron gas. For instance, a single fermionic excitation splits into a collective excitation carrying charge and a collective excitation carrying spin, which have, in general, different velocities ('spin-charge separation'). Because such properties have first been found in the Tomonaga-Luttinger model, we call the one-dimensional electron gas a Tomonaga-Luttinger liquid (TLL).

From a theoretical point of view, one-dimensional systems offer big advantages because some one-dimensional models are exactly solvable by Bethe ansatz. In addition, for more complicated models which cannot be solved exactly, we can carry out very accurate numerical calculations. Furthermore, thanks to recent remarkable developments of the experimental techniques, there are some quasi one-dimensional materials in which the properties of a TLL have been measured. Thus, in one dimension we have the unique opportunity to compare directly the accurate, or sometimes exact, theoretical results for many-particle Hamiltonians with experiment.

A characteristic quantity for one-dimensional metallic systems is the so-called TLL exponent  $K_\rho$  which determines the algebraic decay of the density-density correlation function. For example,  $K_\rho$  gives the critical exponent for the slope of the density of states near the Fermi energy. Therefore, it is a natural task to calculate  $K_\rho$  for TL liquids and to compare it with experimental findings. However, it is by no means trivial to calculate  $K_\rho$  for a given many-particle Hamiltonian. The solution of this ' $K_\rho$ -Problem' is the topic of part I of this thesis.

Bethe-ansatz solutions make it possible to examine a model not only at zero temperature but also at finite temperatures. However, the investigations at finite temperature require the solution of a complicated set of coupled integral equations which are called *Thermodynamic Bethe Ansatz* (TBA) equations. From the low-temperature and high-temperature expansions we know much about the properties of the Hubbard model in these temperature regimes, but much less is known about elementary excitations for intermediate temperatures. One temperature range which can be addressed analytically is the spin-disordered regime at half band-filling. For large Coulomb interactions, the energy scales for the spin degrees of freedom and the charge degrees of freedom separate. This opens a temperature corridor where the spin degrees of freedom are thermally disordered so that they only contribute entropically. At the same time there are exponentially few thermally activated charge degrees of freedom in the Mott–Hubbard insulator. The Mott–Hubbard insulator in infinite dimensions also displays a spin-disordered background. In this model the critical interaction strength  $U_c$  is unknown, with conflicting results about its precise value. Therefore, it is desirable to have an example of a Hubbard-type model with a disordered spin background which can be solved exactly. This is done in part II of the thesis.

## 1.2 Outline of the thesis

This thesis contains two parts. In part I we discuss reliable numerical schemes to calculate the TL parameter  $K_\rho$ . In part II we derive new analytical results for the thermodynamics of the one-dimensional Hubbard model in the spin-disordered regime.

**Part I** The low-energy physics of gapless one-dimensional correlated electron systems can be described by the Tomonaga–Luttinger liquid (TLL) theory. In general, the Green function and various correlation functions show a power-law behavior as a function of momentum  $k$  and frequency  $\omega$ . The decay of the correlation functions is determined by the so-called TLL parameter  $K_\rho$  which depends on the strength of the interactions. In this part, we describe the behavior of  $K_\rho$  in various Hubbard-type models. To see the special features of one-dimensional systems we discuss Luttinger-liquid properties and the characteristic TLL parameter  $K_\rho$  in chapter 2.

For a numerical calculation of  $K_\rho$ , we start with a synopsis of exact diagonalization (ED), the most popular numerical method. However, we can treat only small lattices with at most 20 sites using ED. Therefore, it is difficult to determine  $K_\rho$  reliably in complicated many-body models. Fortunately, we have a powerful numerical method, the density-matrix renormalization group (DMRG), which overcomes these limitations. We introduce the basic ideas and algorithms of ED and DMRG in chapter 3.

In chapter 4, we introduce a method to obtain the TL parameter  $K_\rho$  using the ED and DMRG methods. We apply this method to the extended Hubbard model at quarter filling with nearest-neighbor and next nearest-neighbor Coulomb repulsions, and investigate its physical properties. Then, we discuss the merits and limitations of this technique.

In chapter 5, we present a more accurate and general approach to obtain  $K_\rho$  using the DMRG method only. We demonstrate its accuracy comparing with exact results from the Bethe ansatz. Then, we apply this method to various Hubbard-type models and investigate the behavior of the TL parameter  $K_\rho$ .

We conclude part I in chapter 6.

**Part II** In this part we analyze the Thermodynamic Bethe Ansatz (TBA) equations of the one-dimensional half-filled Hubbard model in the spin-disordered regime, which is characterized by the temperature being much larger than the magnetic energy scale but small compared to the Mott–Hubbard gap.

In chapter 7, we introduce two examples for a system in the spin-disordered regime. The first example is the one-band Hubbard model at half band-filling in infinite dimensions. In this system the precise value of the critical interaction strength  $U_c$  where the Mott–Hubbard gap closes is still a matter of debate. The equations from Dynamical Mean-Field Theory need to be solved numerically and the best available treatments using the Dynamical Density-Matrix Renormalization Group method lead to conflicting results. As a second example, we treat the Harris–Lange model which corresponds to the first order expansion in  $W/U$  of the one-dimensional Hubbard model, where  $W$  is the band width. We summarize the physical properties and the results of the optical conductivity in this model.

In chapter 8, we recall the TBA equations from the Lieb–Wu and Takahashi equations, and introduce the strong-coupling expansion of the TBA equations by Ha. Here, we merely recall the derivations in the literature which provides the necessary insight into the formalism and permits us to fix the notations.

Based on Ha’s approach we examine the TBA equations in the spin-disordered regime in chapter 9 where the internal energy and the effective quasi-particle dispersion become essentially independent of temperature. An interpretation of this regime in terms of a putative interacting-electron system at zero temperature leads to a metal-insulator transition at a finite interaction strength above which the gap opens linearly.

We conclude part II in chapter 10.

A summary and outlook in chapter 11 close the scientific part of the thesis.

### 1.3 Related publications

Some parts of this thesis are contained in the following publications:

#### Part I

- *Accurate calculation of the Tomonaga–Luttinger parameter  $K_\rho$  using the density-matrix renormalization group method*  
S. Ejima, F. Gebhard, and S. Nishimoto,  
accepted for publication in Physica B
- *Tomonaga–Luttinger parameters for doped Mott insulators*  
S. Ejima, F. Gebhard, and S. Nishimoto,  
Europhysics Letters **70**, 492 (2005), cond-mat/0507508
- *Phase diagram of the  $t$ - $U$ - $V_1$ - $V_2$  model at quarter filling*  
S. Ejima, F. Gebhard, S. Nishimoto, and Y. Ohta,  
Physical Review B **72**, 033101 (2005), cond-mat/0411151

**Part II**

- *Thermodynamics of the one-dimensional half-filled Hubbard model in the spin-disordered regime*  
S. Ejima, F. H. L. Essler, and F. Gebhard,  
Journal of Physics A: Mathematical and General **39** 4845 (2006), cond-mat/0602310

## **Part I**

### **Solution of the $K_\rho$ -problem**



## 2 Correlated electrons in one dimension

In order to investigate real quantum many-particle systems with  $10^{23}$  particles, we always start from model Hamiltonians. Even for these simplifying models, it is almost always impossible to find an exact solution in dimensions larger than one. In contrast, some one-dimensional systems can be solved exactly and general model systems in one dimension can also be treated successfully by recently developed numerical methods. These investigations confirm that in the low-energy limit all one-dimensional metallic systems belong to the generic class of Tomonaga–Luttinger liquids (TLL). Thanks to the recent significant development of the experimental techniques, signatures of TLL have been found in real materials as well.

In this chapter, we introduce Hubbard-type Hamiltonians in one dimension to investigate the properties of TLL in the following chapters. Then, we give a review of the Tomonaga–Luttinger theory. Lastly, we collect some experimental results for the signatures of the TLL, which motivate our investigations in part I of this thesis.

### 2.1 Models for lattice electrons

The discovery of high- $T_c$  cuprate superconductors in 1986 [1] has renewed the interest in strongly correlated systems. It is generally believed that the Hubbard model and its generalizations capture the physics of the two-dimensional high- $T_c$  superconductors. In one dimension, Hubbard-type models are believed to be a good description of various materials such as carbon nanotubes, transition-metal oxide chains, and Bechgaard salts.

In this section, we introduce microscopic Hamiltonians for correlated electron in one dimension. We discuss the trivial limits of the model parameters. Lastly, we summarize well-known results for each model which we will further investigate later in this thesis.

#### 2.1.1 Hubbard model

The Hubbard model [2] is the conceptually simplest paradigm for strongly correlated electron systems. As such it has attracted a massive amount of research effort so far. For details we refer the interested reader to Refs. [3–5]. The one-dimensional Hubbard model with  $L$  lattice sites ( $L$  even) is given by

$$\hat{\mathcal{H}} = -t \sum_{j=1}^L \sum_{\sigma=\uparrow,\downarrow} (\hat{c}_{j,\sigma}^\dagger \hat{c}_{j+1,\sigma} + \hat{c}_{j+1,\sigma}^\dagger \hat{c}_{j,\sigma}) + U \sum_{j=1}^L \hat{n}_{j\uparrow} \hat{n}_{j\downarrow} \quad (2.1)$$

where  $\hat{c}_{j,\sigma}^\dagger$  ( $\hat{c}_{j,\sigma}$ ) is the creation (annihilation) operator of an electron with spin  $\sigma = \uparrow, \downarrow$  on site  $j$ ,  $\hat{n}_{j,\sigma} = \hat{c}_{j,\sigma}^\dagger \hat{c}_{j,\sigma}$  is the number operator, and  $\hat{n}_j = \hat{n}_{j,\uparrow} + \hat{n}_{j,\downarrow}$ . The electron transfer matrix element between neighboring sites is denoted by  $t$ , and  $U$  parametrizes the purely local Coulomb interaction. In this thesis, we set  $\hbar = 1$  and set the lattice spacing  $a$  equal to unity.

The Fermi creation and annihilation operators  $\hat{c}_{j,\sigma}^\dagger$  and  $\hat{c}_{j,\sigma}$  fulfill the canonical anticommutation relations ( $\{\hat{A}, \hat{B}\} = \hat{A}\hat{B} + \hat{B}\hat{A}$ )

$$\{\hat{c}_{j,\sigma}, \hat{c}_{j',\sigma'}\} = \{\hat{c}_{j,\sigma}^\dagger, \hat{c}_{j',\sigma'}^\dagger\} = 0 \quad (2.2)$$

$$\{\hat{c}_{j,\sigma}^\dagger, \hat{c}_{j',\sigma'}\} = \delta_{j,j'}\delta_{\sigma,\sigma'}. \quad (2.3)$$

In a tight-binding model of noninteracting electrons ( $U = 0$  in (2.1)), the spectrum is readily determined by means of Fourier transformation. We introduce the electron creation and annihilation operators in momentum space as

$$\hat{c}_{k_l,\sigma}^\dagger = \frac{1}{\sqrt{L}} \sum_j e^{ij k_l} \hat{c}_{j,\sigma}^\dagger, \quad \hat{c}_{k_l,\sigma} = \frac{1}{\sqrt{L}} \sum_j e^{-ij k_l} \hat{c}_{j,\sigma}. \quad (2.4)$$

where  $k_j = 2\pi n_j/L$  and  $n_j = -L/2, \dots, L/2-1$  for periodic boundary conditions,  $\hat{c}_{L+l,\sigma} = \hat{c}_{l,\sigma}$ . In momentum space the tight-binding Hamiltonian  $\hat{\mathcal{H}}_0$  takes the form

$$\hat{\mathcal{H}}_0 = \sum_{k_j,\sigma} \epsilon(k_j) \hat{c}_{k_j,\sigma}^\dagger \hat{c}_{k_j,\sigma}, \quad (2.5)$$

where the band structure  $\epsilon(k)$  is

$$\epsilon(k) = -2t \cos(k). \quad (2.6)$$

In the Hamiltonian (2.1) the particle number and the  $z$ -component of the total spin are conserved

$$[\hat{\mathcal{H}}, \hat{N}] = [\hat{\mathcal{H}}, \hat{S}^z] = 0, \quad (2.7)$$

where the particle number operator  $\hat{N} = \hat{N}_\uparrow + \hat{N}_\downarrow$  is defined by

$$\hat{N} = \sum_{j=1}^L (\hat{n}_{j,\uparrow} + \hat{n}_{j,\downarrow}), \quad (2.8)$$

and the operator of the  $z$ -component of the total spin is given by

$$\hat{S}^z = \frac{1}{2} \sum_{j=1}^L (\hat{n}_{j,\uparrow} - \hat{n}_{j,\downarrow}). \quad (2.9)$$

The band filling is  $n = N/L = \langle \hat{N} \rangle / L$ . Moreover, under an *electron-hole transformation* for all band-fillings with fixed electron numbers the Hubbard model transforms as

$$\hat{\mathcal{H}}(N_\uparrow, N_\downarrow, U, t) \mapsto \hat{\mathcal{H}}(L - N_\uparrow, L - N_\downarrow, U, -t) - U(L - N_\uparrow - N_\downarrow). \quad (2.10)$$

Adding a term  $-2U\hat{N}/2 + LU/4$  to (2.1), the Hamiltonian can be rewritten without affecting its eigenfunctions in a convenient form as

$$\hat{\mathcal{H}}' = -t \sum_{j=1}^L \sum_{\sigma=\uparrow,\downarrow} (\hat{c}_{j,\sigma}^\dagger \hat{c}_{j+1,\sigma} + \text{h.c.}) + U \sum_{j=1}^L \left( \hat{n}_{j,\uparrow} - \frac{1}{2} \right) \left( \hat{n}_{j,\downarrow} - \frac{1}{2} \right), \quad (2.11)$$

so that the band is half-filled at all temperatures for  $\mu(T) = 0$ . Here, 'h.c.' means hermitian conjugate.

As we will discuss in Chapter 8, the one-dimensional Hubbard model is exactly solvable for all band-fillings and interaction strengths. At half-band filling it displays a metal-insulator transition.

### 2.1.2 Extended Hubbard model

In order to obtain Mott transitions at other commensurate fillings than half band-filling, we need to introduce longer-range Coulomb interactions in the basic Hubbard Hamiltonian (2.1) as follows:

$$\begin{aligned} \hat{\mathcal{H}}_{\text{ext}} = & -t \sum_{j,\sigma} (\hat{c}_{j,\sigma}^\dagger \hat{c}_{j+1,\sigma} + \hat{c}_{j+1,\sigma}^\dagger \hat{c}_{j,\sigma}) + U \sum_j \hat{n}_{j\uparrow} \hat{n}_{j\downarrow} \\ & + \sum_{s=1}^{s_{\text{max}}} V_s \sum_{j=1}^L \sum_{\sigma,\sigma'} (\hat{n}_{j,\sigma} - n_c)(\hat{n}_{j+s,\sigma'} - n_c), \end{aligned} \quad (2.12)$$

where  $V_s$  is the strength of the longer-range Coulomb interaction between fermions on sites of separation  $s$ . In this thesis we call the model as the  $t$ - $U$ - $V$  model ( $V \equiv V_1$ ) when  $s_{\text{max}} = 1$ ,  $t$ - $U$ - $V_1$ - $V_2$  model when  $s_{\text{max}} = 2$ , and so on.

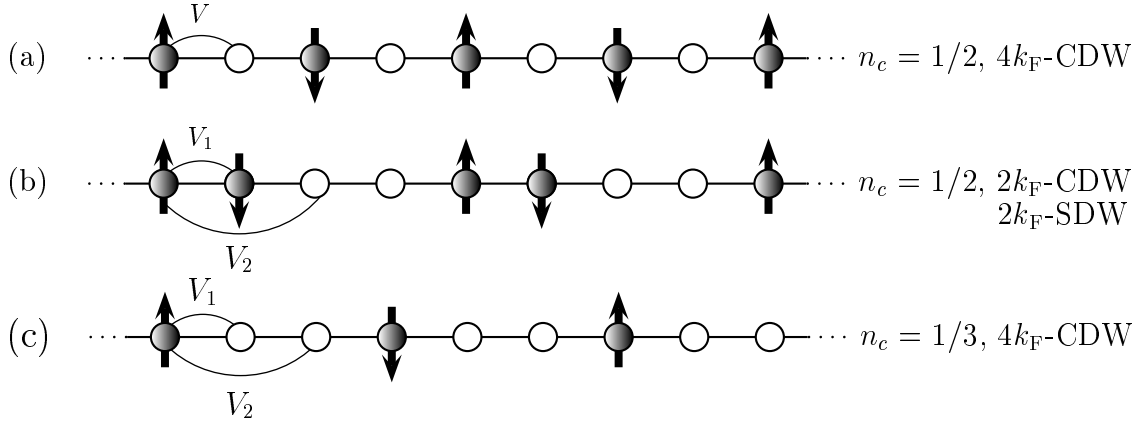


Fig. 2.1: Schematic representation of charge-density-waves at various fillings.

In the  $t$ - $U$ - $V$  model at half filling, we have a bond-order-wave (BOW) phase between the spin-density-wave (SDW) and the charge-density-wave (CDW) phases [6–9]. In the case of quarter filling, because of the nearest neighbor interaction  $V$  we can expect an ordered structure where electrons are spaced by one site as shown in Fig. 2.1 (a). One can easily see that for  $U = \infty$  and  $V = \infty$  a quarter-filled system is a CDW insulator. So far, phase diagrams of the  $t$ - $U$ - $V$  model at quarter filling have been obtained by several groups [10, 11].

The  $t$ - $U$ - $V_1$ - $V_2$  model at quarter filling exhibits an even richer phase diagram. For this reason, several theoretical studies have been made on this and similar models. In the ground state there exist two types of CDW phases, the so-called  $4k_F$ -CDW, Fig. 2.1 (a), and the  $2k_F$ -CDW, Fig. 2.1 (b). Between the two CDW phases there appears a wide region of a vanishing charge gap that results from the geometrical frustration of the long-range Coulomb interactions. If we assumed the intersite Coulomb repulsions to be inversely proportional to the intersite distance, we would find  $V_1 = 2V_2$ , so that neither of the two CDW instabilities dominates in the atomic limit,  $t = 0$ . Hence, one can easily imagine that the phase diagram contains a metallic region as soon as a finite  $t$  is introduced. However,

little is known about the physical properties of this metallic state. We will investigate this metallic region more precisely in Chap. 4.

At filling  $n_c = 1/6$ , the CDW structure of Fig. 2.1 (c) could be realized. It also requires the introduction of a next nearest-neighbor Coulomb interaction  $V_2$ . For large enough values of  $U$ ,  $V_1$  and  $V_2$ , the charge gap opens and the system displays a  $4k_F$ -CDW. Schmitteckert *et al.* have investigated a spinless fermion model with longer-range Coulomb interactions  $V_1$  and  $V_2$  [12] and derived its phase diagram. In Chap. 5, we will study a similar system of spin-1/2 fermions.

### 2.1.3 (Extended) Peierls–Hubbard model

In order to investigate the effect of a lattice distortion, we need to consider the Hubbard model with dimerization. The (extended) Peierls Hubbard model is defined by the Hamiltonian

$$\begin{aligned} \hat{\mathcal{H}} = & -t_1 \sum_{j=1}^{L/2} \sum_{\sigma} (\hat{c}_{2j-1,\sigma}^{\dagger} \hat{c}_{2j,\sigma} + \hat{c}_{2j,\sigma}^{\dagger} \hat{c}_{2j-1,\sigma}) - t_2 \sum_{j=1}^{L/2} \sum_{\sigma} (\hat{c}_{2j,\sigma}^{\dagger} \hat{c}_{2j+1,\sigma} + \hat{c}_{2j+1,\sigma}^{\dagger} \hat{c}_{2j,\sigma}) \\ & + U \sum_{j=1}^L \hat{n}_{j\uparrow} \hat{n}_{j\downarrow} + V \sum_{j=1}^L \sum_{\sigma, \sigma'} (\hat{n}_{j,\sigma} - n_c)(\hat{n}_{j+1,\sigma'} - n_c), \end{aligned} \quad (2.13)$$

where  $t_1$  and  $t_2 < t_1$  are the alternating electron transfer integrals. The bare band structure consists of the bonding and antibonding bands, i.e., the dispersion relation for  $U = V = 0$  is given by

$$\epsilon(k) = \pm \sqrt{t_1^2 + t_2^2 + 2t_1 t_2 \cos k} \quad \text{for } |k| < \pi/2. \quad (2.14)$$

The band width is  $W = 2(t_1 + t_2)$ . It reduces to that of the single-band Hubbard model,  $W = 4t$ , when there is no dimerization  $t_1 = t_2 = t$ . In this thesis we consider  $N$  interacting spin-1/2 electrons on a chain with  $L$  sites ( $= L/2$  dimers), and choose  $L/2$  to be even.

The Bechgaard salts, such as  $(\text{TMTSF})_2X$ , can be regarded as essentially one-dimensional systems above a crossover temperature  $T_x$  of the order of 30 K [13]. From stoichiometry it is known that there are three electrons in the highest occupied molecular orbital for each pair  $(\text{TMTSF})_2$ , so that the system is 3/4-filled in terms of electrons or quarter-filled in terms of holes. Therefore, the (extended) Peierls–Hubbard model at quarter filling can be considered as the minimal model for charge transfer salts.

## 2.2 Luttinger liquids

The effects of interactions in three-dimensional systems have been successfully explained by Landau's Fermi liquid theory. The important characteristics of the excitations of a free electron gas are as follows. All states up to the Fermi energy are occupied at  $T = 0$ . So the occupation  $n(k)$  of a state with momentum  $k$  has a *discontinuity* at the Fermi surface. For free electrons the amplitude of the discontinuity is unity. When interactions are switched on in the system, the remarkable result of Fermi liquid theory is that not much changes and that the properties of the system remain quantitatively the same as for free

fermionic particles. The occupation number  $n(k)$  of a state with momentum  $k$  still has a *discontinuity* at the Fermi surface. However, the amplitude of this discontinuity is not unity any more: the larger the interaction the smaller the discontinuity. Moreover, the elementary particles are not the individual electrons any more but so-called “quasiparticles”, i.e., the electrons are dressed by density fluctuations around them. At low energies, these individual quasiparticles can be considered as essentially free.

In one-dimensional models of interacting fermions, however, this quasiparticle concept breaks down. Generically, the properties of the system do not resemble those of a Fermi liquid. Instead, the space and time dependent correlation functions display unusual power-law decays. The exponents are not universal but depend on the strength of the interaction. Such systems belong to the generic class of Tomonaga–Luttinger liquids (TLL). The name derives from the exactly solvable Tomonaga–Luttinger model where such an anomalous behavior has first been found. Systems such as the one-dimensional XXZ Heisenberg model or the Hubbard model display similar properties. In this section, we will use this model to introduce the TLL concept. Then, we review recent experimental results of quasi one-dimensional materials.

### 2.2.1 Generic properties

As introduced in Sec. 2.1, the kinetic energy term  $\hat{T}$  is given by

$$\hat{T} = \sum_k \sum_{s=\uparrow,\downarrow} \epsilon(k) \hat{c}_{k,s}^\dagger \hat{c}_{k,s}, \quad (2.15)$$

where  $\epsilon(k)$  is the single-particle band structure. In a tight-binding model one would have  $\epsilon(k) = -2t \cos k$ . The Fermi surface consists just of the two points,  $k = \pm k_F$ .

For weak interactions between the particles, only states in the immediate vicinity of the Fermi points are important. For these states, one may linearize the electronic dispersion relation around the Fermi points, and the kinetic energy term  $\hat{T}$  takes the form

$$\hat{T} = \sum_{k,s} v_F [(k - k_F) \hat{c}_{k,s}^{\text{R}\dagger} \hat{c}_{k,s}^{\text{R}} + (-k - k_F) \hat{c}_{k,s}^{\text{L}\dagger} \hat{c}_{k,s}^{\text{L}}]. \quad (2.16)$$

Here the  $\hat{c}^{\text{R}}$  ( $\hat{c}^{\text{L}}$ ) operators refer to states in the vicinity of  $+k_F$  ( $-k_F$ ), i.e., the  $\hat{c}^{\text{R}}$ -particles move to the right, the  $\hat{c}^{\text{L}}$ -particles move to the left. The  $k$ -summation is limited to an interval  $[-k_0, k_0]$  around  $k_F$  (typically,  $k_0 \approx \pi/2$ ). The Fermi velocity is given by

$$v_F = \left. \frac{\partial \epsilon(k)}{\partial k} \right|_{k_F}, \quad (2.17)$$

and the density of states is  $N(E_F) = 1/(\pi v_F)$ . In the *Tomonaga–Luttinger model*, one generalizes this kinetic energy by letting the cutoff  $k_0$  tend to infinity. Then, there are two branches of particles, namely, “right movers” and “left movers”. This modification makes the model exactly solvable even in the presence of nontrivial interactions. In addition, and most importantly, many of the features of this model carry over to strongly interacting fermions on a lattice.

To make progress, we introduce the Fourier components of the particle density operator for right and left movers by

$$\hat{\rho}_{+,s}(q) = \sum_k \hat{c}_{k+q,s}^{\text{R}\dagger} \hat{c}_{k,s}^{\text{R}}, \quad \hat{\rho}_{-,s}(q) = \sum_k \hat{c}_{k+q,s}^{\text{L}\dagger} \hat{c}_{k,s}^{\text{L}}. \quad (2.18)$$

They obey Bose-type commutation relations:

$$[\hat{\rho}_{+,s}(-q), \hat{\rho}_{+,s}(q')] = [\hat{\rho}_{-,s}(q), \hat{\rho}_{-,s}(-q')] = \delta_{qq'} \frac{qL}{2\pi}, \quad [\hat{\rho}_{+,s}(q), \hat{\rho}_{-,s}(q')] = 0. \quad (2.19)$$

The Bose operators are obtained as

$$\hat{b}_{\pm,q} = \sqrt{\frac{2\pi}{qL}} \hat{\rho}_{\pm,s}(q). \quad (2.20)$$

Then, the kinetic part of the Hamiltonian can be rewritten as [14]

$$\hat{T} = \frac{2\pi v_{\text{F}}}{L} \sum_{q>0,s} [\hat{\rho}_{+,s}(q) \hat{\rho}_{+,s}(-q) + \hat{\rho}_{-,s}(-q) \hat{\rho}_{-,s}(q)]. \quad (2.21)$$

The interaction term  $\hat{\mathcal{H}}_{\text{int}}$  takes the form

$$\hat{\mathcal{H}}_{\text{int}} = \hat{\mathcal{H}}_{\text{int},1} + \hat{\mathcal{H}}_{\text{int},2} + \hat{\mathcal{H}}_{\text{int},3} + \hat{\mathcal{H}}_{\text{int},4}, \quad (2.22)$$

where the four possible scattering terms are given by

$$\hat{\mathcal{H}}_{\text{int},1} = \frac{1}{L} \sum_{k,k',q} \sum_{s,s'} g_{1ss'} [\hat{c}_{k,s}^{\text{R}\dagger} \hat{c}_{k',s'}^{\text{L}\dagger} \hat{c}_{k'+2k_{\text{F}}+q,s}^{\text{R}} \hat{c}_{k-2k_{\text{F}}-q,s}^{\text{L}}], \quad (2.23)$$

$$\hat{\mathcal{H}}_{\text{int},2} = \frac{1}{L} \sum_q \sum_{s,s'} g_{2ss'} \hat{\rho}_{+,s}(q) \hat{\rho}_{-,s'}(-q), \quad (2.24)$$

$$\hat{\mathcal{H}}_{\text{int},3} = \frac{1}{2L} \sum_{k,k',q} \sum_{s,s'} g_{3ss'} [\hat{c}_{k,s}^{\text{R}\dagger} \hat{c}_{k',s'}^{\text{R}\dagger} \hat{c}_{k'-2k_{\text{F}}+q,s'}^{\text{L}} \hat{c}_{k+2k_{\text{F}}-q-G,s}^{\text{L}} + \text{h.c.}], \quad (2.25)$$

$$\hat{\mathcal{H}}_{\text{int},4} = \frac{1}{2L} \sum_q \sum_{s,s'} g_{4ss'} [\hat{\rho}_{+,s}(q) \hat{\rho}_{+,s'}(-q) + \hat{\rho}_{-,s}(-q) \hat{\rho}_{-,s'}(q)]. \quad (2.26)$$

Here,  $g_{iss'}$  ( $i = 1, \dots, 4$ ) are coupling constants, and  $G = 2\pi$  is a reciprocal lattice vector. The couplings  $g_{iss'}$  are functions of the parameters of the original lattice model. The possible scattering processes, as depicted graphically in Fig. 2.2, are:

**forward scattering:** small momentum transfers; parameters  $g_{2ss'}$ ,  $g_{4ss'}$

**backward scattering:** large momentum transfers; parameter  $g_{1ss'}$

**umklapp scattering:** only allowed at half filling as  $4k_{\text{F}} = G$  is required; parameter  $g_{3ss'}$

The general ‘ $g$ -ology’ model can be solved approximately only. When only the coupling constants  $g_2$  and  $g_4$  are finite, we arrive at the exactly solvable *Tomonaga–Luttinger model*.

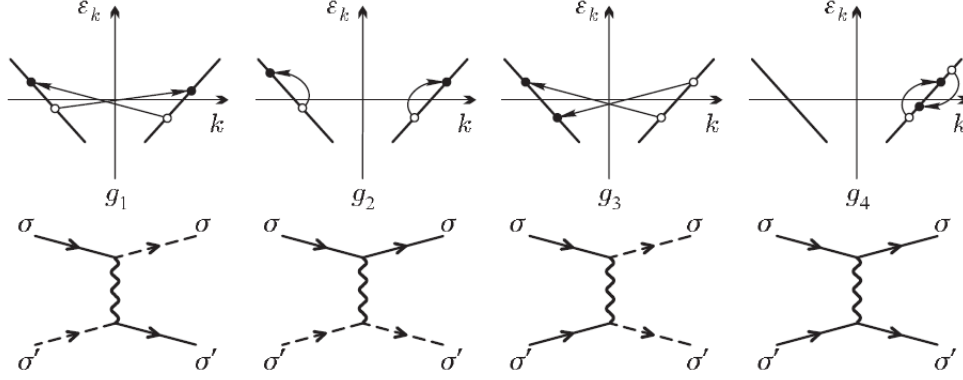


Fig. 2.2: Scattering processes in a one-dimensional electron gas. Solid lines stand for right-moving electrons, dashed lines for left-moving electrons.

In what follows we will assume that the model has spin-rotational symmetry, i.e.  $g_{i\uparrow\uparrow} = g_{i\downarrow\downarrow}$  and  $g_{i\uparrow\downarrow} = g_{i\downarrow\uparrow}$ , and thus we will use the notation

$$g_{i\parallel} = g_{iss} \ , \quad g_{i\perp} = g_{is,-s} \ . \quad (2.27)$$

When we consider the scattering process of two parallel spins, we do not know whether the scattering is forward or backward because we cannot distinguish them. In other words, we can combine the forward scattering  $g_{2\parallel} \hat{c}^\dagger \hat{c}^\dagger \hat{c} \hat{c}$  and the backward scattering  $g_{1\parallel} \hat{c}^\dagger \hat{c}^\dagger \hat{c} \hat{c}$  in the form  $(g_{1\parallel} - g_{2\parallel})$ , i.e., we can eliminate one parameter. By convention we take  $g_{2\parallel} = g_{2\perp} \equiv g_2$ . Moreover, because of the Pauli principle we do not have to take  $g_{3\parallel}$  and  $g_{4\parallel}$  into account. Therefore, we just write  $g_{3\perp} \equiv g_3$  and  $g_{4\perp} \equiv g_4$ . Lastly, in the case of SU(2) symmetry we have  $g_{1\parallel} = g_{1\perp} \equiv g_1$ .

To bosonize the full Hamiltonian  $\hat{\mathcal{H}} = \hat{T} + \hat{\mathcal{H}}_{\text{int}}$ , one introduces the fields  $\hat{\phi}$  and  $\hat{\Pi}$  for the two spin projections, and then transforms to charge and spin bosons via

$$\hat{\phi}_\nu = \frac{\hat{\phi}_\uparrow \pm \hat{\phi}_\downarrow}{\sqrt{2}} \ , \quad \hat{\Pi}_\nu = \frac{\hat{\Pi}_\uparrow \pm \hat{\Pi}_\downarrow}{\sqrt{2}} \quad \text{for } \nu = \rho, \sigma, \quad (2.28)$$

where

$$\hat{\phi}_s(x) = -\frac{i\pi}{L} \sum_{p \neq 0} \frac{1}{p} e^{-\eta|p|/2 - ipx} [\hat{\rho}_{+,s}(p) + \hat{\rho}_{-,s}(p)] - N \frac{\pi x}{L} \ , \quad (2.29)$$

$$\hat{\Pi}_s(x) = \frac{1}{L} \sum_{p \neq 0} e^{-\eta|p|/2 - ipx} [\hat{\rho}_{+,s}(p) - \hat{\rho}_{-,s}(p)] + \frac{J}{L} \ . \quad (2.30)$$

Here  $N$  and  $J$  are the number of particles added to the ground state and the difference between the number of right and left-moving particles, respectively, and  $\eta$  is a cutoff parameter which is set to zero at the end of the calculations. The operators  $\hat{\phi}_\nu$  and  $\hat{\Pi}_\nu$  obey Bose-like commutation relations:

$$[\hat{\phi}_\nu, \hat{\Pi}_\mu] = i\delta_{\nu\mu} \delta(x - y) \ , \quad (2.31)$$

and single fermion operators can be written as

$$\hat{\psi}_{\pm,s}(x) = \lim_{\eta \rightarrow 0} \frac{1}{2\pi\eta} \hat{F}_{\pm s} \exp \left[ \pm i k_F x - i \frac{1}{\sqrt{2}} \{ \pm (\hat{\phi}_\rho + s\hat{\phi}_\sigma) - (\hat{\theta}_\rho + s\hat{\theta}_\sigma) \} \right], \quad (2.32)$$

where

$$\hat{\theta}_\nu = \pi \int_{-\infty}^x \hat{\Pi}_\nu(x') dx'. \quad (2.33)$$

Here, the *Klein operators*  $\hat{F}_{+s}$  and  $\hat{F}_{-s}$  raise or lower the total fermion number by one. We introduce them so that the field operators  $\hat{\psi}_{\pm,s}(x)$  obey the fermionic anticommutation relations. For gapless systems, a change in the particle number is a  $(1/L)$ -effect. However, one must take these operators into account [15] for excitations over a gap.

Then, the full Hamiltonian in the absence of umklapp scattering ( $g_3 = 0$ ) takes the form

$$\hat{\mathcal{H}} = \hat{\mathcal{H}}_\rho + \hat{\mathcal{H}}_\sigma + \frac{g_{1\perp}}{(2\pi\eta)^2} \int dx \cos(\sqrt{8}\hat{\phi}_\sigma) \quad (2.34)$$

with

$$\hat{\mathcal{H}}_\nu = \int dx \left[ \frac{\pi v_\nu K_\nu}{2} \Pi_\nu^2 + \frac{v_\nu}{2\pi K_\nu} (\partial_x \phi_\nu)^2 \right] \quad (2.35)$$

and

$$v_\nu = \left[ \left( v_F + \frac{g_{4,\nu}}{\pi} \right)^2 - \frac{g_\nu^2}{(2\pi)^2} \right]^{1/2}, \quad (2.36)$$

$$K_\nu = \left[ \frac{2\pi v_F + 2g_{4,\nu} + g_\nu}{2\pi v_F + 2g_{4,\nu} - g_\nu} \right]^{1/2}. \quad (2.37)$$

Here,  $g_\nu$  and  $g_{i,\nu}$  are defined as

$$g_\nu = g_{1\parallel} - g_{2\parallel} \mp g_{2\perp}, \quad (2.38)$$

$$g_{i,\nu} = g_{i\parallel} \pm g_{i\perp}. \quad (2.39)$$

That is

$$g_\rho = g_1 - 2g_2, \quad g_\sigma = g_1, \quad g_{4,\rho} = g_4, \quad g_{4,\sigma} = -g_4. \quad (2.40)$$

$H_\rho$  and  $H_\sigma$  describe free bosonic modes (collective charge and spin excitations) which propagate with velocities  $v_\rho$  and  $v_\sigma$ , respectively. For a noninteracting system one thus has  $v_\nu = v_F$  (i.e., charge and spin velocities are equal) and  $K_\nu = 1$ . The fact that  $v_\rho \neq v_\sigma$  in general is called ‘spin-charge separation’ because the spin and charge degrees of freedom of the original electrons propagate at different velocities. Furthermore,  $K_\nu$  are the so-called ‘anomalous exponents’ or ‘TL parameters’ which determine the critical behavior in one-dimensional systems.

Let us consider physical quantities. The quantity  $\Pi_\rho(x)$  is proportional to the current density. Since the Hamiltonian commutes with the total current, we obtain

$$\sigma(\omega) = 2K_\rho v_\rho \delta(\omega) + \sigma_{\text{reg}}(\omega), \quad (2.41)$$

i.e., the Drude weight is directly related to the TL parameter  $K_\rho$ . Moreover, using Eq. (2.32) the single-particle Green function is described as

$$\begin{aligned} G^R(x, t) &= -i\theta(t)\langle[\hat{\psi}_{+,s}(x, t), \hat{\psi}_{+,s}^\dagger(x, t)]_+\rangle \\ &= -\frac{\theta(t)}{\pi} e^{ik_F x} \operatorname{Re} \left\{ \frac{1}{\sqrt{(v_\rho t - x)(v_\sigma t - x)}} \left[ \frac{\eta^2}{(\eta + iv_\rho t)^2 + x^2} \right]^{\alpha/2} \right\}. \end{aligned} \quad (2.42)$$

Fourier transforming (2.42) gives the momentum distribution function in the vicinity of  $k_F$ :

$$n(k) \propto \operatorname{sign}(k - k_F) |k - k_F|^\alpha, \quad (2.43)$$

and for the single-particle density of the states we find

$$D(\omega \rightarrow E_F) \sim |\omega|^\alpha. \quad (2.44)$$

In both cases the critical exponents  $\alpha$  is given by

$$\alpha = (K_\rho + K_\rho^{-1} - 2)/4 > 0. \quad (2.45)$$

We note that for any nonvanishing interaction ( $K_\rho \neq 1$ ) the momentum distribution function and the density of states displays a *power-law* behavior at the Fermi level, with a vanishing single particle density of states at  $E_F$ . This behavior is completely different from a Fermi liquid which would have a finite density of states and a discontinuity at the Fermi surface.

### 2.2.2 Correlation functions

As explained above, the one-dimensional electron systems belong to the same *universal class* called Tomonaga–Luttinger liquids. Furthermore, in the correlated one-dimensional systems there are two different phases, namely the gapless Tomonaga–Luttinger (TL) phase and the gapped Luther–Emery (LE) phase. The ground state is mainly characterized by the following correlations:

- spin singlet superconductivity (SS)
- spin triplet superconductivity (TS)
- charge-density-wave (CDW)
- spin-density-wave (SDW)

In general, correlation functions are defined as

$$C^{XY}(r) = \frac{1}{L} \sum_j \left( \langle \hat{X}_{j+r} \hat{Y}_j \rangle - \langle \hat{X}_{j+r} \rangle \langle \hat{Y}_j \rangle \right). \quad (2.46)$$

For example,  $X = \hat{N} = Y$  for density correlations and  $X = \hat{S}^z = Y$  for spin correlations. In the TL phase the correlation functions decay algebraically as a function of distance  $r$  for large  $r$ , modulated by  $\cos(2k_F r)$  for  $2k_F$ -CDW/SDW ( $\cos(4k_F r)$  for  $4k_F$ -CDW). Explicitly,

$$C^{\text{SS}}(r) \sim r^{-K_\sigma - 1/K_\rho}, \quad (2.47)$$

$$C^{\text{TS}}(r) \sim r^{-1/K_\sigma - 1/K_\rho}, \quad (2.48)$$

$$C^{2k_{\text{F}}\text{-CDW}}(r) \sim r^{-K_\sigma - K_\rho} \cos(2k_{\text{F}}r), \quad (2.49)$$

$$C^{4k_{\text{F}}\text{-CDW}}(r) \sim r^{-4K_\rho} \cos(4k_{\text{F}}r), \quad (2.50)$$

$$C^{2k_{\text{F}}\text{-SDW}}(r) \sim r^{-K_\sigma - K_\rho} \cos(2k_{\text{F}}r). \quad (2.51)$$

For a system with spin-rotational symmetry, we have  $K_\sigma = 1$ . Then,  $K_\rho = 1$  corresponds to non-interacting electrons, and  $K_\rho > 1$  ( $K_\rho < 1$ ) result for attractive (repulsive) interactions. Albeit there is no true long-range order in the TL ground state, the ‘phase’ is named after the correlation function with the weakest decay, i.e., the dominant fluctuations. Actually, in the case of  $K_\sigma = 1$  the dominant fluctuations are  $2k_{\text{F}}$ -CDW or  $2k_{\text{F}}$ -SDW for  $K_\rho < 1$ , and SS or TS for  $K_\rho > 1$ .

In the LE phase a spin gap opens. In this case the contributions from spin excitations vanish, and  $K_\sigma$  becomes zero. Thus, TS and  $2k_{\text{F}}$ -SDW correlations decay exponentially. In the  $2k_{\text{F}}$ -CDW and SS, the asymptotic decay of the correlations is given by

$$\text{SS: } \sim r^{-1/K_\rho}, \quad (2.52)$$

$$2k_{\text{F}}\text{-CDW: } \sim r^{-K_\rho}. \quad (2.53)$$

Therefore, the SS ( $2k_{\text{F}}$ -CDW) correlation is dominant for  $K_\rho > 1$  ( $K_\rho < 1$ ). We summarize the results in table 2.1.

	$\Delta_{\text{s}} \neq 0$	$\Delta_{\text{s}} = 0$
$\Delta_{\text{c}} \neq 0$	$2k_{\text{F}}$ -CDW	SDW
$\Delta_{\text{c}} = 0$	$2k_{\text{F}}$ -CDW, SS	SDW, TS

Table 2.1: Table of the dominant correlations depending on the existence of charge and spin gaps ( $\Delta_{\text{s}}$ : spin gap;  $\Delta_{\text{c}}$ : charge gap).

### 2.2.3 Commensurabilities

The umklapp process can also be expressed in terms of boson operators [14] as

$$\hat{\mathcal{H}}_{\text{int},3} = \frac{2g_3}{(2\pi\eta)^2} \int dx \cos(\sqrt{8}\phi_\rho). \quad (2.54)$$

This umklapp operator is effective at and near half-filling. Furthermore, umklapp scatterings exist not only at half-filling but for higher-order *commensurability* by transferring more particles across Fermi surface. Such processes are generated in higher order in perturbation theory [16–19]. To take the existence of this type of processes into account we add a term in the full Hamiltonian [19]

$$\hat{\mathcal{H}}_u = g_u \int dx \cos^m(\sqrt{2}\phi_\sigma(x)) \cos(\sqrt{2}m\phi_\rho(x)), \quad (2.55)$$

where  $g_u \approx g^{m+1}/t^m$  for band-filling  $1/m$  with an interaction matrix element  $g$ , i.e., we transfers  $m$  particles from  $-k_F$  to  $k_F$ , with matrix element  $g_u$ . There are now two physically different cases, according to the parity of  $m$ . If  $m$  is even, the  $\cos^m(\sqrt{2}\phi_\sigma(x))$  term can be expanded, and the lowest-order comes from the constant in this expansion, i.e., the effective  $\hat{\mathcal{H}}_u$  is

$$\hat{\mathcal{H}}_u \approx g_u \int dx \cos(\sqrt{2}m\phi_\rho(x)). \quad (2.56)$$

After a unitary transformation, we obtain the following results: at filling exactly equal to  $1/m$  we can have an insulator or a metallic phase, with the metallic state stable for  $K_\rho \geq 4/m^2$ , and  $K_\rho^* = 4/m^2$  at the metal-insulator transition. We approach the transition point as we increase the interaction strengths. Therefore, we call this kind of transition an *interaction-driven* metal-insulator transition. In addition, varying the particle density at constant  $K_\rho < 4/m^2$ , we arrive at another kind of a metal-insulator transition: as  $n \rightarrow 2/m$  one has  $K_\rho^{\text{CDW}} \rightarrow 2/m^2$ . We call this kind of transition as *density-driven* metal-insulator transition. The whole situation is shown in Fig. 2.3.

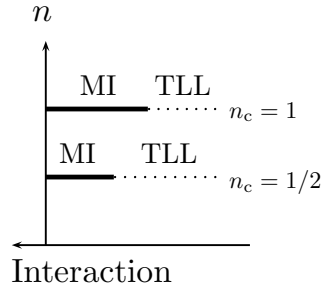


Fig. 2.3: Phase diagram of a generic interacting electron system. Mott insulating (MI) phases exist for commensurate densities only.

If  $m$  is odd, the situation is different. Now, the most relevant term in  $\hat{\mathcal{H}}_u$  is given by

$$\hat{\mathcal{H}}_u \approx g_u \int dx \cos(\sqrt{2}\phi_\sigma(x)) \cos(\sqrt{2}m\phi_\rho(x)), \quad (2.57)$$

i.e., spin and charge degrees of freedom are coupled. This operator produces a gap if  $K_\rho < 3/m^2$ . For a summary of the different types of critical TL parameters, see table 2.2.

	$n = 2/m$ $K_\rho \rightarrow K_\rho^*$	$n \rightarrow 2/m$ $K_\rho^{\text{CDW}} = \text{const.}$
$m$ even	$4/m^2$	$2/m^2$
$m$ odd	$3/m^2$	$1/(2m^2)$

Table 2.2: Critical behavior of the different metal-insulator transitions. The transition is approached from the metallic side. From table 1 in Ref. [17].

From table 2.2, we obtain  $K_\rho^* = 1/4$  and  $K_\rho^{\text{CDW}} = 1/8$  at quarter filling ( $m = 4$ ),  $K_\rho^* = 1/9$  and  $K_\rho^{\text{CDW}} = 1/18$  at one-sixth filling ( $m = 6$ ), respectively. These examples show that a slightly doped CDW insulator leads to a metallic phase with a small value for  $K_\rho$ , and, correspondingly, a large value for the exponent  $\alpha$ , see Eq. (2.45). In this thesis, we will investigate only the case  $m$  even. In this case we have  $K_\rho^* = n_c^2$  and  $K_\rho^{\text{CDW}} = n_c^2/2$  from table 2.2 when the transition is approached from the metallic side. Later, we will reproduce the field-theoretical predictions using numerical methods.

## 2.3 Experimental results

Quite a number of experiments have been carried out in order to detect the signatures of TL liquids. Here, we give a brief review of the recent experimental results for materials which are believed to be TL liquids.

### 2.3.1 Metallic single-wall carbon nanotubes

Carbon nanotubes (CN) have been discovered first by Iijima in 1991 [20]. They are multi-wall nanotubes consisting of concentric tubes of a two-dimensional graphite sheet arranged in a helical fashion about the axis. Later, single-wall carbon nanotubes (SWCN) have been produced [21,22]. Carbon nanotubes can be either a metal or a semiconductor, depending on their diameters and helical arrangement. The condition whether a CN is metallic or semiconducting can be obtained based on the band structure of a two-dimensional graphite sheet with periodic boundary conditions along the circumference direction. Since nanotubes are very stable one-dimensional conductors, SWCN attract a lot of attention from a theoretical point of view.

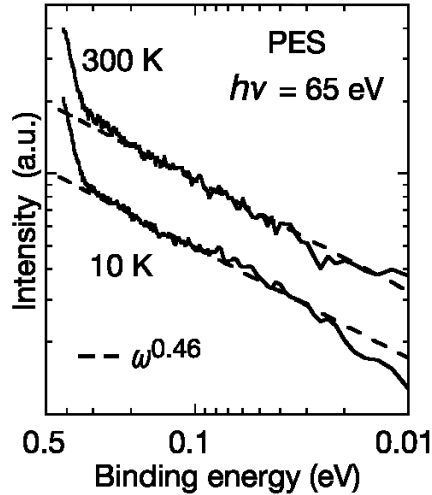


Fig. 2.4: High-resolution photo-emission spectra of SWCN near  $E_F$  measured at 10 K and 300 K with an energy resolution of 15 meV at  $h\nu = 65$  eV, plotted on a log-log scale, from Ref. [23].

Electrical transport measurements on single SWCN have been reported first by Tans *et al.* [24] who confirmed that SWCN indeed act as genuine quantum wires. Quite recently, Ishii *et al.* reported angle-integrated photoemission measurements of SWCN [23]. High-resolution photoemission spectra of SWCN with an energy resolution of 15 meV at  $h\nu = 65$  eV are shown in Fig. 2.4 as a function of the binding energy on a double-logarithmic scale. Fitting a power-law behavior  $D(\omega) \sim \omega^\beta$ , the exponent  $\beta$  is found to be  $0.46 \pm 0.10$ , see Fig. 2.4.

According to Egger *et al.* [25], we have to be cautious when estimating the TL parameter  $K_\rho$  in the case of SWCN. We should not use the “surface exponent”  $\beta$  but the following “bulk density of states”:

$$D_{\text{bulk}}(\omega) \sim \omega^\alpha \quad (2.58)$$

where the bulk scaling dimension is  $\alpha = 2\beta$ . Then, we obtain the fairly small value  $K_\rho \simeq 0.18$  from  $\beta \sim 0.46$ .

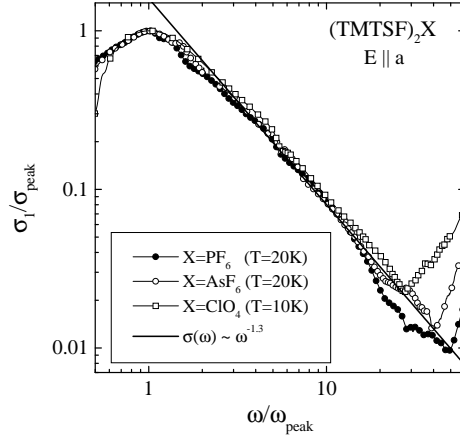


Fig. 2.5: Frequency dependence of the conductivities on a log-log scale in the  $(\text{TMTSF})_2X$  salts. The solid line is Eq. (2.59) with the exponent  $\nu = 1.3$ , from Ref. [26].

### 2.3.2 Bechgaard salts

Bechgaard salts are linear chain compounds based on the organic molecule tetramethyltetraselenofulvalene (TMTSF) or its analog tetramethyltetrathiafulvalene (TMTTF) where Selenium is substituted by Sulphur. Their composition is  $(\text{TMTSF})_2X$ , where  $X$  is a counterion such as  $\text{ClO}_4$ ,  $\text{PF}_6$ , or  $\text{AsF}_6$ . In the  $(\text{TMTSF})_2X$  family, charge transfer of one electron from every two TMTSF molecules leads to a quarter-filled band (or half-filled band due to the dimerization). The bandwidth is anisotropic and band structure calculations lead to transfer integrals  $t_a \sim 250\text{meV}$ ,  $t_b \sim 25\text{meV}$ , and  $t_c \sim 1\text{meV}$  in the three crystallographic directions [27]. Note that these values depend on the actual salts and can also vary by the methods of calculation. In any case, we can consider the  $(\text{TMTSF})_2X$  family as quasi one-dimensional electronic systems.

To compare the one-dimensional theory with experimental results, Vescoli *et al.* [26] measured the electrodynamic response of the  $(\text{TMTSF})_2X$  family. Calculations for TL liquids show that the frequency dependence of the conductivity at quarter filling is given by [16, 18, 28]

$$\sigma(\omega) \sim \omega^{-\nu} ; \nu = 16K_\rho - 5 . \quad (2.59)$$

A log-log plot of the experimental results is shown in Fig. 2.5. The observed exponent  $\nu \sim 1.3$  of the frequency dependence gives a small value for the TL exponents  $K_\rho \approx 0.23$ , which corresponds to a large value of a density of states exponent  $\alpha \approx 0.64$ , in agreement with photoemission experiments [29].

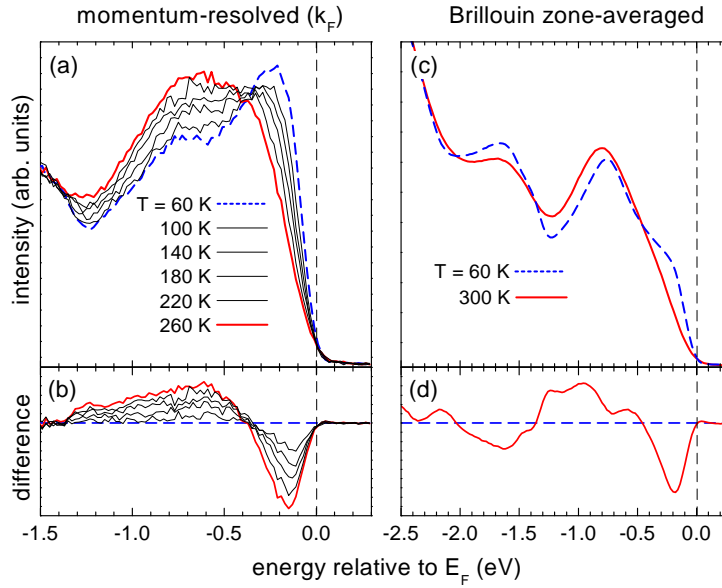


Fig. 2.6: Temperature dependence of the photoemission spectra of TTF-TCNQ ( $h\nu = 21.2$  eV). (a) Momentum-resolved spectrum at  $k = k_F$  measured between 60 K (dashed curve) and 260 K (solid curve). (b) Difference spectra relative to 60 K. (c) Momentum integrated spectrum at 60 K (dashed) and 300 K (solid). (d) Difference spectrum relative to 60 K, from Ref. [30].

### 2.3.3 TTF-TCNQ

The quasi one-dimensional conductor tetrathiafulvalene-tetracyanoquinodimethane (TTF-TCNQ) is an organic charge transfer salt. TTF-TCNQ contains planar TTF and TCNQ molecules, stacked to form segregated chains parallel to the crystallographic  $\mathbf{b}$  direction of the monoclinic structure. The conductivity along  $\mathbf{b}$  is up to three orders of magnitude

larger than perpendicular to it, making TTF-TCNQ a truly quasi one-dimensional metal. A charge transfer of about 0.59 electrons per molecule from TTF to TCNQ leads to a large metallic conductivity along the chains. A CDW with wave vector  $2k_F$  develops below  $T_P = 54$  K on the TCNQ chains and eventually brings the system into an insulating ordered state below 38 K [13].

Various properties of TTF-TCNQ have successfully been analyzed with the one-dimensional single-band Hubbard model [31]. It is generally accepted that  $U/4t \simeq 1$  for TTF-TCNQ, with the unperturbed bandwidth  $4t \sim 0.5$  eV from experiment and band theory [31]. For the Hubbard model, the TL exponent for the density of states near the Fermi energy is  $\alpha_H \leq 1/8$ .

By means of angle-resolved photoelectron spectroscopy (ARPES), the electronic structure of TTF-TCNQ has been recently studied [30,32]. The photoemission spectra at various temperatures are shown in Fig. 2.6. As seen in this figure, there is an almost *linear* energy dependence, which corresponds to  $\alpha \gtrsim 1$ . As in the previous examples, this corresponds to a rather small value for  $K_\rho$ . Using (2.45) we find  $K_\rho \lesssim 3 - 2\sqrt{2} \simeq 0.17$ .

The small experimental values for  $K_\rho$  cannot be reconciled with the Hubbard model. As discussed in more detail in Chap. 5, the bare Hubbard model gives  $K_\rho \geq 1/2$ , so that  $\alpha_H \leq 1/8$ . Indeed, the following arguments have been involved in [30] to explain the discrepancies between experiment and Hubbard-model predictions for the density of states near  $E_F$ :

- Impurities and/or defects on the surface of an organic conductor.
- Electron-phonon coupling, i.e., the Peierls transition at low temperatures.
- Long-range Coulomb interactions.

In the rest of part I of this thesis we shall investigate  $K_\rho$  as a function for the long-range Coulomb interactions. We shall show that  $K_\rho < 0.2$  can only be obtained in the vicinity of a CDW insulator. To this end, we must develop numerical methods which permit a reliable calculation of the TL parameter  $K_\rho$  for extended Hubbard models.



### 3 Numerical methods

Various numerical methods are used to investigate strongly correlated quantum systems. The most direct method is Exact Diagonalization (ED). The ED technique allows us to calculate almost all properties of a quantum system. Unfortunately, ED is restricted to systems with up to about 20 particles because of the exponential increase of the memory capacity with the number of particles. In many cases, such system sizes are too small to extrapolate the physical quantities of interest to the thermodynamic limit. Quantum Monte Carlo (QMC) simulations can be applied to much larger systems than ED techniques. However, they are restricted to simple quantum models because of the notorious “minus sign” problem. Using the Density-Matrix Renormalization Group (DMRG) method one can overcome these problems. DMRG can be used to investigate very large systems,  $L \sim \mathcal{O}(10^3)$ , and it is widely applicable. Over the last decade, DMRG has become the main tool to investigate quasi one-dimensional systems. In this chapter, we will introduce basic notions of the ED and the DMRG which we will use in the remaining chapters of part I.

#### 3.1 Exact Diagonalization (ED): Lanczos method

In general, we are interested in a quantum system with  $L$  sites, where  $L \rightarrow \infty$  or at least  $L \gg 1$ . To investigate such a many-particle system, we need to diagonalize the Hamiltonian. In the case of the Hubbard model, each site of the lattice represents a single-electron orbital, which can be empty, occupied by one electron of spin  $\sigma = \uparrow, \downarrow$ , or occupied by two electrons of opposite spin. Therefore, the dimension  $D$  of the matrix to diagonalize grows exponentially with the number of sites  $L$  ( $D = 4^L$  for the Hubbard model).

However, we are interested in the eigenvalues and eigenvectors of a few states only, say, the ground state and a few excited states. In this case, we need not store the whole Hamiltonian matrix, which requires a memory of  $D \times D$  words, but only a few vectors of length  $D$ . One of the well-known algorithms to find a (variational) representation of the ground state is the *Lanczos method* [33]. In this section, we give a short review of the exact diagonalization (ED) by the Lanczos method; for detailed reviews and implementations, see [34–36] and references therein.

The first step of the Lanczos method is to operate with the Hamiltonian  $\hat{\mathcal{H}}$  on an arbitrary vector  $|\phi_0\rangle$  (normalized to unity) in the Hilbert space of the model under consideration. Usually, we select an initial trial vector with *randomly* chosen coefficients in our basis. In this way we satisfy the requirement that the overlap between the actual ground state  $|\psi_0\rangle$  and the initial state  $|\phi_0\rangle$  is finite. If some exact quantum numbers of the ground state are known, it is convenient to initiate the iterations with a state with the same quantum numbers, with random coefficients within this subspace.

Applying  $\hat{\mathcal{H}}$  over  $|\phi_0\rangle$ , we define a state  $|\phi_1\rangle$  as follows:

$$|\phi_1\rangle = \hat{\mathcal{H}}|\phi_0\rangle - \frac{\langle\phi_0|\hat{\mathcal{H}}|\phi_0\rangle}{\langle\phi_0|\phi_0\rangle}|\phi_0\rangle, \quad (3.1)$$



### 3.2.1 Density matrix projection

We describe the entire system as the *superblock*, and divide it into the *system block*  $|i\rangle$  and *environment block*  $|j\rangle$  as shown in Fig. 3.1. Then, the state of the superblock is given by

$$|\psi\rangle = \sum_{i,j} \psi_{i,j} |i\rangle |j\rangle. \quad (3.6)$$

Here, we assume  $|\psi\rangle$  to be normalized,  $\langle\psi|\psi\rangle = 1$ . The reduced density matrix for the system block is described as

$$\rho_{ii'} = \sum_j \psi_{ij}^* \psi_{i'j}, \quad (3.7)$$

where  $\text{Tr}\hat{\rho} = 1$  by normalization. Then, for any system block operator  $\hat{A}$  we have

$$\langle\psi|\hat{A}|\psi\rangle = \text{Tr}\hat{\rho}\hat{A} = \sum_{\alpha} w_{\alpha} \langle u^{\alpha}|\hat{A}|u^{\alpha}\rangle \quad (3.8)$$

with the eigenstates  $|u^{\alpha}\rangle$  and eigenvalues  $w_{\alpha} \geq 0$  of  $\hat{\rho}$ . Since  $\text{Tr}\hat{\rho} = 1$ , we have  $\sum_{\alpha} w_{\alpha} = 1$ . Eq. (3.8) gives us a way to discard some states from the system block, namely, keeping the states with significant  $w_{\alpha}$  and discarding ones with  $w_{\alpha} \approx 0$ , we obtain a good approximation value of  $\langle\hat{A}\rangle$  as

$$\langle\psi|\hat{A}|\psi\rangle_{\text{approx}} = \sum_{\alpha=1}^m w_{\alpha} \langle u^{\alpha}|\hat{A}|u^{\alpha}\rangle \quad (3.9)$$

for a fixed number of  $m$  system block states kept.

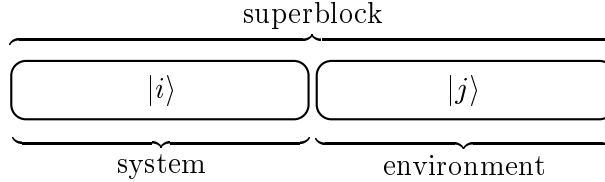


Fig. 3.1: A superblock divided into a system block and an environment block.

Let us make this argument more precise. For the moment, we assume that the superblock has been diagonalized and we have obtained one particular state  $|\psi\rangle$ , e.g., the ground state. We wish to construct an accurate approximation state  $|\psi'\rangle$  for  $|\psi\rangle$ , which is described by

$$|\psi\rangle \approx |\psi'\rangle = \sum_j \sum_{\alpha=1}^m a_{\alpha,j} |u^{\alpha}\rangle |j\rangle, \quad (3.10)$$

where the system block states  $|u^{\alpha}\rangle$  are defined for a fixed number  $m$  of states kept as

$$|u^{\alpha}\rangle = \sum_i u_i^{\alpha} |i\rangle, \quad \alpha = 1, \dots, m. \quad (3.11)$$

To this end, we minimize

$$\mathcal{D}_m = ||\psi\rangle - |\psi'\rangle|^2 \quad (3.12)$$

by varying over all  $a_{\alpha,j}$  and  $u^\alpha$ , with the condition  $\langle u^\alpha | u^{\alpha'} \rangle = \delta_{\alpha,\alpha'}$ . In general, one can write

$$|\psi'\rangle = \sum_{\alpha} a_{\alpha} |u^{\alpha}\rangle |v^{\alpha}\rangle, \quad (3.13)$$

where  $v_j^{\alpha} = \langle j | v^{\alpha} \rangle = N_{\alpha} a_{\alpha,j}$ , with  $N_{\alpha}$  chosen to set  $\sum_j |v_j^{\alpha}|^2 = 1$ . Then,  $\mathcal{D}_m$  is described by

$$\mathcal{D}_m = \sum_{ij} \left( \psi_{ij} - \sum_{\alpha=1}^m a_{\alpha} u_i^{\alpha} v_j^{\alpha} \right)^2, \quad (3.14)$$

and we need to minimize  $\mathcal{D}_m$  over all  $u^\alpha$ ,  $v^\alpha$  and  $a_\alpha$  with the given number of  $m$ . Here,  $\psi$  is a rectangular matrix. The solution is produced by the singular value decomposition [41] of  $\psi$ ,

$$\psi = U D V^T, \quad (3.15)$$

where  $U$  and  $D$  are  $\ell \times \ell$  matrices,  $V$  is an  $\ell \times J$  matrix (where  $j = 1, \dots, J$ , and we assume  $J \geq \ell$ ),  $U$  is orthogonal,  $V$  is column-orthogonal, and the diagonal matrix  $D$  contains the singular values of  $\psi$ . Here, the diagonal elements of  $D$  are the  $a_\alpha$  and the corresponding columns of  $U$  and  $V$  are the  $u^\alpha$  and  $v^\alpha$ . Using Eq. (3.7) we obtain

$$\rho = U D^2 U^T. \quad (3.16)$$

The eigenvalues of  $\rho$  are  $w_\alpha = a_\alpha^2$  and the eigenstates of  $\rho$  with the largest eigenvalues are  $u^\alpha$ . Each  $w_\alpha$  represents the probability of the block being in the state  $u^\alpha$ , with  $\sum_{\alpha} w_\alpha$ .

More specifically,  $D_m$  is the so-called ‘‘discarded weight’’ of the density matrix eigenvalues

$$D_m = \sum_{\alpha=m+1}^{m_{\max}} w_\alpha = 1 - \sum_{\alpha=1}^m w_\alpha, \quad (3.17)$$

where  $m_{\max}$  is the size of the density matrix. Since the discarded weight  $D_m$  is strongly correlated with the error in the ground-state energy,  $D_m$  is often used as a measure of the error. One can calculate the ground-state energy and the discarded weight for several values of  $m$  and make an extrapolation  $m \rightarrow \infty$ . This approach provides a reliable estimate of the error on the ground-state energy [37, 42].

In general, the accuracy of the energy for a given  $m$  is many orders of magnitude worse for periodic than for open boundary conditions. Therefore, it is usually better to treat systems with open boundary conditions on larger lattices than small systems with periodic boundary conditions.

### 3.2.2 DMRG algorithms

In the following, we will describe how to combine the superblock procedure with the density matrix projection in order to define efficient DMRG algorithms. For simplicity, we assume that the system size  $L$  is even.

#### The infinite-system algorithm

The starting point of the DMRG procedure is the infinite-system algorithm to enlarge the system size in real space while keeping the maximal dimension of the superblock Hamiltonian constant. The environment block is constructed using a *reflection* of the system block. The superblock configuration is shown in Fig. 3.2. Here,  $\tilde{\mathcal{H}}_l$  is the Hamiltonian for the system block with the reduced basis, each dot represents a single site, and the environment block  $\tilde{\mathcal{H}}_l^R$  is obtained by the reflection of  $\tilde{\mathcal{H}}_l$ .

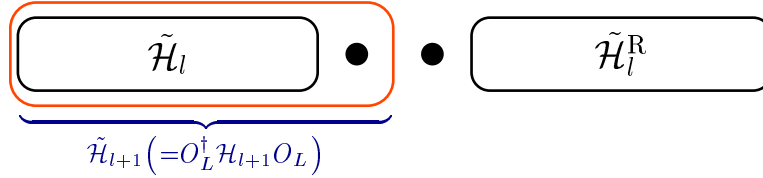


Fig. 3.2: Superblock configuration for the DMRG infinite-system algorithm.

The infinite-system algorithm proceeds as follows:

1. Form a superblock with  $L$  sites that is small enough to be exactly diagonalized.
2. Diagonalize the superblock Hamiltonian  $\mathcal{H}_L^{\text{SB}}$ , e.g., by using the Lanczos algorithm, or the more elaborate Lanczos–Davidson [43] algorithm, to find the ground-state eigenvalue  $E_0$  and eigenvector  $|\psi\rangle$ . Other states could also be kept, such as the first excited ones. They are called “target states”.
3. Form the reduced density matrix  $\rho_{ii'}$  for the new system block with  $l'$  sites from  $|\psi\rangle$  using Eq. (3.7), where  $l' = l = L/2 - 1$ .
4. Diagonalize  $\rho_{ii'}$ , and obtain the  $m$  eigenvectors  $u_1, \dots, u_m$  with the largest eigenvalues.
5. Construct  $\mathcal{H}_{l+1}$  and other operators  $A_{l+1}$  in the new system block, and transform them to the reduced density matrix eigenbasis as  $\tilde{\mathcal{H}}_{l+1} = O_L^\dagger \mathcal{H}_{l+1} O_L$  and  $\tilde{A}_{l+1} = O_L^\dagger A_{l+1} O_L$ , where  $O_L = (u_1, \dots, u_m)$ .
6. Form a new superblock  $\mathcal{H}_{L+2}^{\text{SB}}$  from  $\tilde{\mathcal{H}}_{l+1}$ , two single sites, and  $\tilde{\mathcal{H}}_{l+1}^R$ .
7. Repeat again from step 2 replacing  $L$  with  $L + 2$ .

The superblock size increases by two sites at each step as shown in Fig. 3.3. Iterations are continued until a good approximation of an infinite system is obtained.

Note that periodic boundary conditions can be attached to the ends by forming the superblock, and a different block layout should be considered to avoid connecting two big blocks (system and environment) which takes longer to converge. This is the key reason why DMRG prefers open boundary conditions.

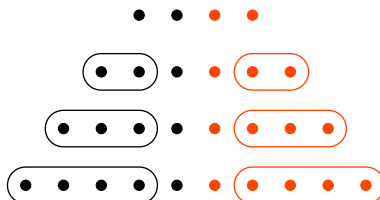


Fig. 3.3: Infinite-system algorithm

### Finite-system algorithm

The finite-system algorithm is the DMRG procedure to calculate the properties of a finite system most accurately. The environment is chosen so that the size of the superblock is kept fixed at every iteration.

The finite-system algorithm proceeds as follows:

0. Run the infinite-system algorithm until the superblock reaches size  $L$ . Store  $\tilde{\mathcal{H}}_l$  and the operators needed to connect the blocks at each iteration.
1. Carry out steps 3-5 of the infinite-system algorithm to obtain  $\tilde{\mathcal{H}}_{l+1}$ , and store it. (Note that now  $l \neq l'$ .)
2. Form a superblock of size  $L$  using  $\tilde{\mathcal{H}}_{l+1}$ , two single sites and  $\tilde{\mathcal{H}}_{l-1}$ .
3. Repeat steps 1 and 2 until the environment size reaches  $l' = 1$ . This is the *left to right* zipping phase of the algorithm.
4. Carry out steps 3-5 of the infinite-system algorithm but with the direction to build up the environment, and store  $\tilde{\mathcal{H}}_{l'+1}^R$  at each iteration.
5. Form a superblock of size  $L$  using  $\tilde{\mathcal{H}}_{l-1}$ , two single sites and  $\tilde{\mathcal{H}}_{l'+1}$ .
6. Repeat steps 4 and 5 until  $l = 1$ . This is the *left to right* zipping phase of the algorithm.
7. Repeat again from step 1.

Iterations are continued through every configuration of the superblock for a given number  $m$  of the density-matrix eigenstates kept until convergence. This procedure is illustrated in Fig. 3.4. This ensures a self-consistent optimization and thus considerably improves the quality of the results as compared to the infinite-system algorithm.

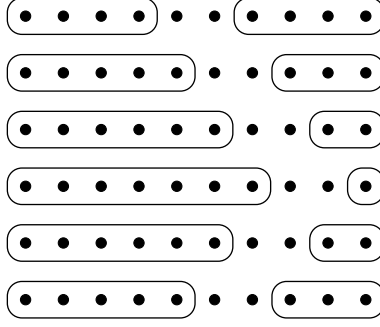


Fig. 3.4: Finite-system algorithm

### 3.2.3 Measurements

To measure physical quantities, we need to calculate expectation values  $\langle \psi | \hat{A} | \psi \rangle$ , where  $\psi$  is the superbloc wavefunction. If we wish to calculate the local observable  $\hat{A}_l$  for all sites  $l$  such as the on-site spin-density  $S_l^z$ , we must keep track of matrices  $[\hat{A}_l]_{ii'}$ , for all sites  $l$  in each of the blocks. Note that these operators must be updated at every step of each DMRG iteration. Then, because  $\hat{A}_l$  acts only on the site  $l$ , we can evaluate its expectation value as

$$\langle \psi | \hat{A}_l | \psi \rangle = \sum_{i,i',j} \psi_{ij}^* [\hat{A}_l]_{ii'} \psi_{i'j}. \quad (3.18)$$

However, if we wish to evaluate a product of two local operators  $\hat{A}_l \hat{B}_m$ , we have to take care whether  $l$  and  $m$  are on the same block or not. If they are on different blocks, we must keep only track of  $[\hat{A}_l]_{ii'}$  and  $[\hat{B}_m]_{jj'}$ , then we have

$$\langle \psi | \hat{A}_l \hat{B}_m | \psi \rangle = \sum_{i,i',j,j'} \psi_{ij}^* [\hat{A}_l]_{ii'} [\hat{B}_m]_{jj'} \psi_{i'j'}. \quad (3.19)$$

If  $l$  and  $m$  are on the same block, we need to keep track of matrices  $[\hat{A}_l \hat{B}_m]_{ii'}$  throughout the calculation. Then we obtain

$$\langle \psi | \hat{A}_l \hat{B}_m | \psi \rangle = \sum_{i,i',j} \psi_{ij}^* [\hat{A}_l \hat{B}_m]_{ii'} \psi_{i'j}. \quad (3.20)$$

It is normally more convenient to choose points  $l$  and  $m$  on different blocks, rather than keep track of complicated matrices  $[\hat{A}_l \hat{B}_m]_{ii'}$ . For a correlation function such as  $\langle \psi | S_l^z S_m^z | \psi \rangle$ , a convenient way is to always put  $l$  and  $m$  at the same distance (within a lattice spacing) from the center of the chain. As  $|l - m|$  is increased, both points move outwards symmetrically towards the ends of the chain.

## 3.3 Summary

In this chapter we have presented the basics of the ED and DMRG methods. The ED technique allows us to calculate properties of a strongly correlated quantum system in a

very direct way. Unfortunately, the ED method is restricted to systems with up to about 20 particles because of the exponential increase of memory requirements with the number of particles and lattice sites. The DMRG method solves this problem and gives us the opportunity to calculate various physical quantities of systems with up to about  $\mathcal{O}(1000)$  sites. Therefore, the DMRG has become the standard tool for the study of strongly correlated one-dimensional quantum systems.

We have left out many important recent DMRG developments such as *dynamical* density-matrix renormalization group, and *time-dependent* DMRG because they are not needed for our studies. For details on these DMRG developments, we refer to Refs. [37–39, 44–46] and references therein.

## 4 Critical exponents from combined ED and DMRG

In this chapter, we first discuss how to obtain the TL parameter  $K_\rho$  through TL relations from the compressibility  $\kappa$  using the DMRG method and the charge velocity  $v_c$  using the ED method. Since we calculate  $\kappa$  using the DMRG technique, the method is more accurate than the one using the ED method only. We also introduce an alternative method to estimate  $K_\rho$  from the Drude weight  $\sigma_0$ , and we compare both approaches. We discuss the limitation of the method in a short summary.

Next, we apply the method to the  $t$ - $U$ - $V_1$ - $V_2$  model at quarter filling to examine its ground-state properties. As already explained in Sec. 2.1.2, there exist  $2k_F$ -CDW and  $4k_F$ -CDW phases in the ground-state phase diagram. In between there appears a broad metallic phase, but little is known about the physical properties of this metallic state. The contents of this chapter has been published as Ref. [47].

### 4.1 Defining equations

#### 4.1.1 Charge velocity and compressibility

In the Tomonaga–Luttinger liquid, the TL parameter  $K_\rho$  is given by [48–50]

$$K_\rho = \frac{\pi}{2} n^2 v_c \kappa, \quad (4.1)$$

where  $v_c$  and  $\kappa$  are the charge velocity and charge compressibility, respectively. To estimate  $K_\rho$  numerically, we calculate the velocity of the charge excitations  $v_c$  from

$$E_{1\rho}(N_\uparrow, N_\downarrow, L) - E_0(N_\uparrow, N_\downarrow, L) = \frac{2\pi}{L} v_c(L), \quad (4.2)$$

where  $E_0(N_\uparrow, N_\downarrow, L)$  denotes the ground-state energy of a chain of length  $L$  with  $N_\uparrow$  spin-up electrons and  $N_\downarrow$  spin-down electrons, and  $E_{1\rho}(N_\uparrow, N_\downarrow, L)$  is the lowest excitation energy with momentum  $k = 2\pi/L$  and total spin  $S = 0$  for finite system size  $L$ . The compressibility  $\kappa$  is obtained by

$$\Delta_c^{(2)} = \frac{4}{n^2 L \kappa(L)}, \quad (4.3)$$

where the two-particle charge gap  $\Delta_c^{(2)}$  is given by

$$\Delta_c^{(2)} = E_0(N_\uparrow + 1, N_\downarrow + 1, L) + E_0(N_\uparrow - 1, N_\downarrow - 1, L) - 2E_0(N_\uparrow, N_\downarrow, L). \quad (4.4)$$

Note that the two-particle charge gap becomes twice the single-particle charge gap in the thermodynamic limit

$$\lim_{L \rightarrow \infty} \Delta_c^{(2)}(L) = 2 \lim_{L \rightarrow \infty} \Delta_c(L), \quad (4.5)$$

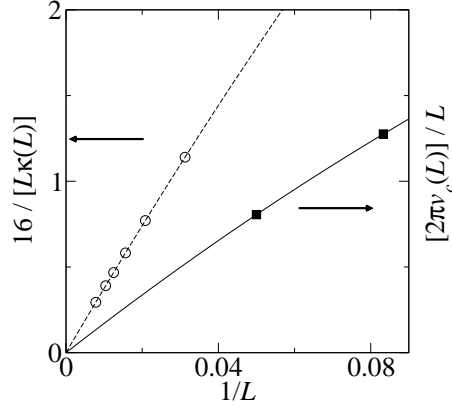


Fig. 4.1: Scaling of the inverse compressibility, Eq. (4.3), and of the charge velocity, Eq. (4.2), in the  $t$ - $U$ - $V_1$ - $V_2$  model as a function of  $1/L$  at  $U/t = 10$ ,  $V_1/t = 1$  and  $V_2/t = 1$ . The lines indicate the polynomial fits by Eq. (4.6) to the data.

when pairing is absent. We find that  $\Delta_c^{(2)}(L)$  decreases monotonically with increasing  $L$ , so that we can extrapolate it to the thermodynamic limit systematically by performing a polynomial fit in  $1/L$ . As shown in Fig. 4.1, both of the quantities  $\kappa$  and  $v_c$  are monotonous functions of  $1/L$  for all parameter sets and can be fitted to a polynomial function,

$$f(L) = a_1 L^{-1} + a_2 L^{-2} + \dots \quad (4.6)$$

Therefore, we obtain

$$\kappa = \lim_{L \rightarrow \infty} \kappa(L) = \frac{16}{a_1^{(\kappa)}}, \quad (4.7)$$

$$v_c = \lim_{L \rightarrow \infty} v_c(L) = \frac{a_1^{(v_c)}}{2\pi}, \quad (4.8)$$

so that the TL parameter can be estimated as

$$K_\rho = \frac{a_1^{(v_c)}}{a_1^{(\kappa)}} \quad (4.9)$$

in the thermodynamic limit.

For the compressibility we use DMRG for up to 128 sites. As seen from Fig. 4.1, the extrapolation is very well behaved, and a reliable extrapolation could have been obtained from the results for much smaller systems. This makes us confident that the extrapolation for the charge velocity is meaningful despite the fact that exact diagonalization is limited to  $L \leq 20$ . We could not use DMRG for the charge velocity because the charge excitation with energy  $E_{1\rho}$  lies rather high in the spectrum and cannot be targeted. A comparison with the exact  $K_\rho^{\text{exact}}$  for the one-dimensional Hubbard model [48] shows that relative errors  $|K_\rho^{\text{DMRG}} - K_\rho^{\text{exact}}|/K_\rho^{\text{exact}}$  are below 1%.

### 4.1.2 Drude weight

Alternatively, one can derive  $K_\rho$  from the Drude weight  $\sigma_0$  and charge velocity  $v_c$  [48]. They share the TL relations, see Eq. (2.41),

$$\sigma_0 = L\pi \frac{\partial^2 E_0(\phi)}{\partial \phi^2} = 2v_c K_\rho, \quad (4.10)$$

where  $\phi$  is the magnetic flux that penetrates our system which is closed to a ring. In Ref. [12], Schmitteckert *et al.* have obtained the ground-state curvature as a function of the flux for spinless fermions with longer-range Coulomb interactions up to 60 sites using the DMRG method. They calculated  $K_\rho$  from Eq. (4.10). They found that the deviation from  $K_\rho^{\text{exact}}$  is about 5%. For our spinful systems, one can calculate  $\sigma_0$  only up to 30 sites, and we expect even larger discrepancies. Therefore, we prefer to calculate  $K_\rho$  from  $\kappa$  and  $v_c$ , and we do not follow the approach by Schmitteckert *et al.*

### 4.1.3 Summary

In this section, we introduced a method to obtain the TL parameter  $K_\rho$  from the compressibility  $\kappa$  and the charge velocity  $v_c$ . Though the method is rather accurate, we still need to use the ED technique to calculate  $v_c$ , so that the system size is restricted to 20 sites. Of course, 20 sites are not enough, especially close to transition lines. From the point of view of hardware requirements a gigantic memory capacity ( $\sim 20$  GB) is needed to perform one calculation of  $v_c$ . In addition, it is almost impossible to study infinitesimal doping,  $n = 1 - 2/L$ , because this case is particularly size-sensitive.

In Chap. 5, we will introduce a much simpler and more accurate method to obtain  $K_\rho$  using *only* the DMRG method, so that we can estimate  $K_\rho$  in any quasi one-dimensional systems with hundreds of electrons. Moreover, this method gives us a possibility to investigate the density-driven metal-insulator transition by calculating  $K_\rho$  in the infinitesimally doped system. Nevertheless, the mixed ED/DMRG approach is still useful, as the following application demonstrates.

## 4.2 Application to the $t$ - $U$ - $V_1$ - $V_2$ model

In this section, we show that, despite its limitations, the ED/DMRG method can be applied successfully to the  $t$ - $U$ - $V_1$ - $V_2$  model. Below, we will provide the full ground-state phase diagram at quarter filling.

When we use the DMRG method in this section, we calculate chains with up to 256 sites with open boundary conditions whereby we keep up to  $m = 2000$  density-matrix eigenstates so that the maximum truncation error is about  $10^{-5}$ . For the calculation of charge excitations we use periodic boundary conditions with the Lanczos Exact Diagonalization technique.

### 4.2.1 Phase diagram at quarter filling

In order to determine the metallic region in the phase diagram, we calculate the charge gap  $\Delta_c/t$  at  $U/t = 10$  and  $V_1/t = 4$  as shown in Fig. 4.2. It is evident that  $\Delta_c/t$  is finite for both small  $V_2/t \leq 0.66$  and large  $V_2/t \geq 3.43$ , i.e., the system is insulating, and  $\Delta_c/t$

vanishes in a wide range of  $V_2/t$ , i.e.,  $0.66 \leq V_2/t \leq 3.43$ , within the accuracy of the extrapolation (error smaller than  $10^{-4}t$ ). The TL parameter  $K_\rho$  is also plotted in Fig. 4.2. We see that  $K_\rho > 0.25$  when the charge gap is zero and  $K_\rho = 0.25$  at the critical points. We have confirmed numerically that  $K_\rho$  is always one quarter at the CDW critical points for all finite values of  $U$ , in agreement with field theory.

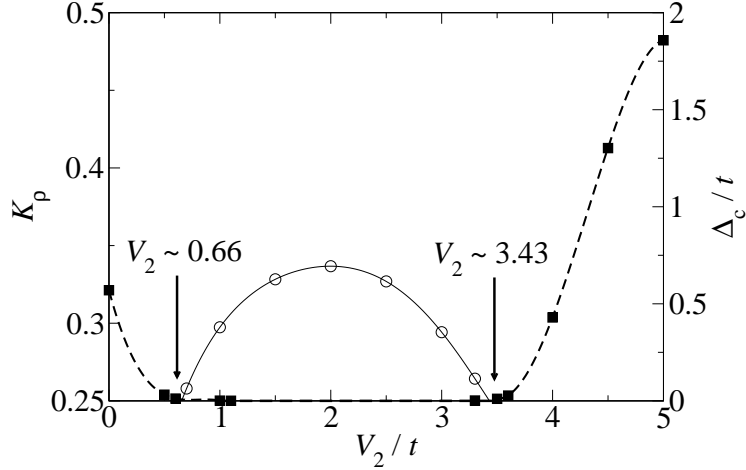


Fig. 4.2: Charge gap  $\Delta_c/t$  (squares) and TL parameter  $K_\rho$  (circles) for the one-dimensional  $t$ - $U$ - $V_1$ - $V_2$  model at quarter filling for  $U/t = 10$  and  $V_1/t = 4$ . Lines are guides to the eye.

For other values of  $V_1/t$  we find similar results as in Fig. 4.2, which demonstrates that a stable metallic phase indeed exists between two insulating phases. Thereby, we obtain the phase diagram of the  $t$ - $U$ - $V_1$ - $V_2$  model as shown in the Fig. 4.3. This result is consistent with other studies [12, 51–53] but much more accurate.

In Fig. 4.3,  $K_\rho$  reaches its maximum value around  $V_1 = 2V_2$ , i.e., the density-density correlations decay most rapidly when  $V_1$  and  $V_2$  maximally frustrate each other. In general, long-range Coulomb repulsions are expected to suppress the value of  $K_\rho$ . This is consistent with our results because  $K_\rho$  decreases when the values of  $V_1$  and  $V_2$  deviate from the relation  $V_1 \approx 2V_2$ , whereby the effective interaction strength increases. Apparently, the line  $V_1 = 2V_2$  goes along the ridges of the contour line of  $K_\rho$  in Fig. 4.3. This has been already suggested in the spinless fermion case and similar models [12, 51].

Lastly, we plot the TL parameter  $K_\rho$  as a function of  $V_1/t$  for fixed  $V_1 = 2V_2$  and several values of  $U$  in Fig. 4.4. For large  $U$ ,  $K_\rho$  decreases as a function of  $V_1/t$  and eventually crosses  $K_\rho = 0.25$  at some finite value of  $V_{1,c}$ . As shown above,  $K_\rho \geq 0.25$  for a metallic phase, so that the Tomonaga–Luttinger liquid turns into the  $4k_F$ -CDW at  $V_{1,c}$ . For small  $U$ , e.g.,  $U = 2t$  in Fig. 4.4,  $K_\rho$  decreases as a function of  $V_1$ , displays a minimum around  $V_1/t \approx \mathcal{O}(U/t)$  with  $K_{\rho,\min} > 0.25$ , and increases again. This results from the fact that  $V_1$  overcomes the Hubbard interaction  $U$  and electrons with opposite spin gain energy from on-site pairing. Eventually,  $K_\rho$  can become larger than unity and superconducting correlations are dominant. As seen from Fig. 4.4, the ground-state phase diagram in Fig. 4.3 is representative for all  $U \gtrsim 4t$  when a superconducting phase does not interfere.

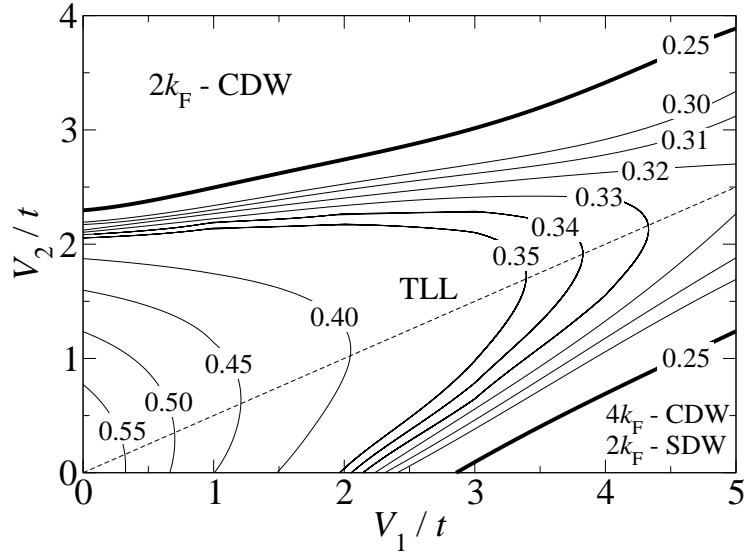


Fig. 4.3: Phase diagram of the one-dimensional  $t$ - $U$ - $V_1$ - $V_2$  model for  $U/t = 10$  at quarter filling.

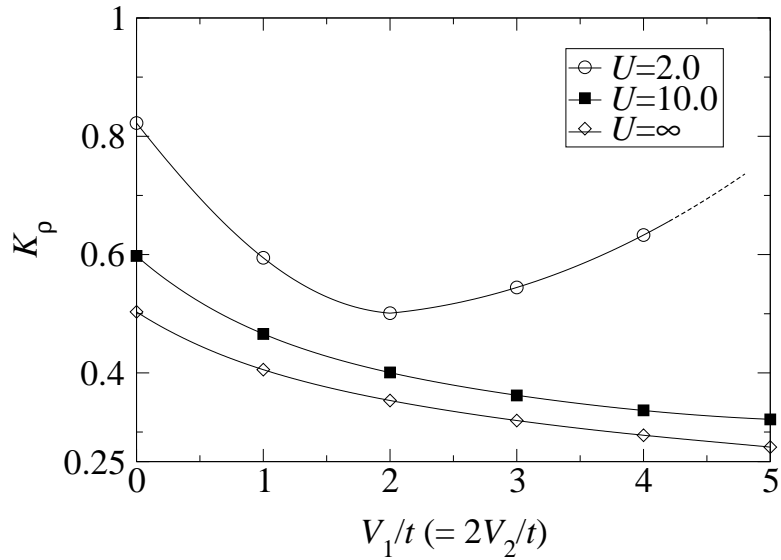


Fig. 4.4: TL parameter  $K_\rho$  for the  $t$ - $U$ - $V_1$ - $V_2$  model at quarter filling as a function of  $V_1/t$  along line  $V_1 = 2V_2$  for  $U = 2t$  (circles),  $U = 10t$  (squares), and  $U = \infty$  (diamonds). The lines are guides to the eye.

### 4.2.2 Absence of a tricritical point

In the limit of large values of  $V_1$  and  $V_2$  ( $V_1, V_2 < U$ ), the boundary between the ordered phases and the metallic phase shrinks. In Ref. [12], Schmitteckert *et al.* have obtained the TL parameter parameter  $K_\rho$  in the  $t$ - $U$ - $V_1$ - $V_2$  model for  $U = \infty$  (i.e., the spinless fermion model) from Eq. (4.10) using the DMRG method, and proposed that there exists a tricritical point where the TLL phase disappears for larger interaction strength.

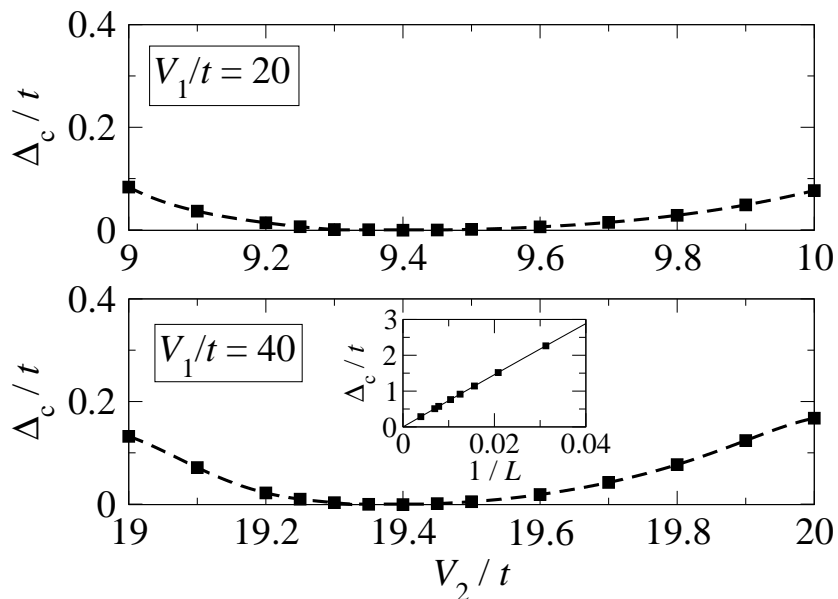


Fig. 4.5: Charge gap for spinless fermions at  $V_1/t = 20$  (upper part) and  $V_1/t = 40$  (lower part). The charge gap vanishes around  $V_2/t = V_1/(2t) - 0.6$  in both cases. The inset shows the charge gap for  $V_2/t = 19.4$  as a function of  $1/L$  for system sizes up to  $L = 256$ .

In Fig. 4.5, we show the charge gap as a function of  $V_2/t$  at  $V_1/t = 20$  and  $V_1/t = 40$  for spinless fermions. It demonstrates that a narrow but stable metallic regime exists between the two insulating phases. For large  $V_1$  and  $V_2$  it is very difficult to extrapolate  $\Delta_c$  reliably from exact diagonalization data ( $L \leq 20$ ), and DMRG [ $L \sim \mathcal{O}(200)$ ] must be used in the extrapolation. For example, Fig. 4.5 shows that  $V_1/t = 40$  at  $V_2/t = 20$  is a CDW insulator whereas it has been assigned a “non-Tomonaga–Luttinger metal” in Ref. [53].

Even with DMRG it is very difficult to decide whether or not the metallic region shrinks to zero at some tricritical point, as proposed in Ref. [12]. If it exists it is far beyond the values quoted previously [12]. As seen from Fig. 4.5 there is a metallic region for  $V_1/t = 40$  in the vicinity of  $V_2/t = 19.4$ . In the surrounding of this point, the gap nicely scales to zero as a function of the inverse system size, as seen from the inset to Fig. 4.5. Our results indicate that the metallic phase appears below the line  $V_2 = V_1/2$ , around  $V_2 = V_1/2 - 0.6t$ . We speculate that there is a metallic phase between the two CDW phases for all finite  $V_1$  and  $V_2$ , i.e., there are *no* tricritical points in the  $V_1$ - $V_2$  phase diagram.

### 4.2.3 Spin gap

In order to study the spin degrees of freedom, we calculate the spin gap for system size  $L$ , defined by

$$\Delta_s(L) = E_0(N_\uparrow + 1, N_\downarrow - 1, L) - E_0(N_\uparrow, N_\downarrow, L). \quad (4.11)$$

As in the case of the charge gap, the extrapolation to the thermodynamic limit is straightforward. In the  $2k_F$ -CDW phase, we find that  $\Delta_s$  is always finite because the system contains separated spin singlet pairs. For fixed  $V_1$ ,  $\Delta_s$  increases as a function of  $V_2$  and eventually saturates at  $\Delta_s = 4t^2/(U - V_1)$  in the limit  $V_2 \rightarrow \infty$ . This is readily understood because, for  $U, V_2 \gg V_1$ , the system can be mapped to an effective spin Hamiltonian

$$\hat{\mathcal{H}} = J_{2k_F} \sum_i \hat{\mathbf{S}}_{4i} \cdot \hat{\mathbf{S}}_{4i+1}, \quad J_{2k_F} = 4t^2/(U - V_1). \quad (4.12)$$

This model is trivially solvable and the spin gap is the energy difference between the singlet and triplet state at each bond,  $\Delta_s = 4t^2/(U - V_1)$ .

In the  $4k_F$ -CDW phase, we find that  $\Delta_s$  is always zero, because a charged site and a vacant site come alternately and the spin degrees of freedom can be described in terms of a one-dimensional uniform Heisenberg model. In fact, for  $U > V_1/2 \gg V_2$ , the effective spin Hamiltonian can be written as

$$\hat{\mathcal{H}} = J_{4k_F} \sum_i \hat{\mathbf{S}}_{2i} \cdot \hat{\mathbf{S}}_{2i+1}, \quad J_{4k_F} = 4 \left( \frac{t^2}{V_1 - 2V_2} \right)^2 \cdot \left( \frac{1}{U - V_2} + \frac{2}{U - 2V_2} \right). \quad (4.13)$$

This effective Heisenberg model displays gapless spin excitations, in agreement with our numerical results.

### 4.2.4 Summary

To summarize this chapter, we proposed a new calculation method to obtain the TL parameter  $K_\rho$  from the charge velocity  $v_c$  using the ED method and the compressibility  $\kappa$  using the DMRG method. Since we calculate  $\kappa$  using the DMRG method up to 256 sites, this method is more accurate than the one which is obtained by the ED method only.

Applying the method to the  $t$ - $U$ - $V_1$ - $V_2$  model at quarter filling, we obtained its accurate ground-state phase diagram. For intermediate to large Hubbard interaction  $U \gtrsim 4t$ , the system has CDW phases with  $q = 2k_F$  and  $4k_F$  between which there appears a broad region of a Tomonaga–Luttinger liquid. Because of the geometrical frustration of the long-range Coulomb interactions,  $K_\rho$  is maximum around  $V_2 = V_1/2$ . It is smallest at the phase boundaries,  $K_\rho^* = 1/4$ , in agreement with field theory. In the vicinity of the CDW insulator, especially for infinitesimal doping, a much more accurate method must be devised. We present such a method in the next chapter.



## 5 Critical exponents from DMRG

In this chapter we introduce a simple and accurate method to obtain  $K_\rho$  using *only* the DMRG method. This method makes it possible to investigate  $K_\rho$  even for the infinitesimally doped Mott–Hubbard insulator as we demonstrate for the Hubbard model at half filling. Then, we prove the accuracy of our methods for all band fillings by comparing with exact results for the Hubbard model and spinless fermions with nearest-neighbor interactions.

Finally, we apply this method to various extended Hubbard models with the aim to find parameter regions with small values of  $K_\rho$  which correspond to the experimental results of quasi one-dimensional materials. Some parts of this chapter have been published as Ref. [54].

### 5.1 Defining equations and tests

#### 5.1.1 Density-density correlation function

The density-density correlation function is defined by the ground-state expectation value

$$C^{\text{NN}}(r) = \frac{1}{L} \sum_{l=1}^L \{ \langle \hat{n}_{l+r} \hat{n}_l \rangle - \langle \hat{n}_{l+r} \rangle \langle \hat{n}_l \rangle \}, \quad (5.1)$$

where  $\hat{n}_l = \sum_{\sigma} \hat{n}_{l,\sigma}$  counts the electrons on site  $l$ . We have  $C^{\text{NN}}(r) = C^{\text{NN}}(-r)$  due to inversion symmetry, and periodic boundary conditions apply.

Using conformal field theory it can be shown [48, 50] that the asymptotic behavior for  $1 \ll r \ll L$  is given by

$$C^{\text{NN}}(r) \sim -\frac{K_\rho}{(\pi r^2)} + \frac{A \cos(2k_{\text{F}}r)}{r^{1+K_\rho}} \ln^{-3/2}(r) + \dots, \quad (5.2)$$

where  $k_{\text{F}} = n\pi/2$  is the Fermi wave number, and  $A$  is a constant. For spinless fermions, the first term should be multiplied by  $1/2$ . In order to extract  $K_\rho$ , we introduce the Fourier transform

$$\tilde{C}^{\text{NN}}(q) = \sum_{r=1}^L e^{-iqr} C^{\text{NN}}(r) \quad (5.3)$$

with  $0 \leq q < 2\pi$ . By construction,  $\tilde{C}^{\text{NN}}(q=0) = 0$ . For the derivative at  $q=0$  one finds in the thermodynamic limit [55]

$$K_\rho = \pi \lim_{q \rightarrow 0^+} \frac{\tilde{C}^{\text{NN}}(q)}{q}. \quad (5.4)$$

In numerical simulations we treat finite systems. There, Eq. (5.4) translates into

$$K_\rho = \lim_{L \rightarrow \infty} \frac{L}{2} \tilde{C}^{\text{NN}} \left( \frac{2\pi}{L} \right). \quad (5.5)$$

Several groups have calculated the density-density correlation function in position space for Hubbard-type models. After Fourier transformation they obtained  $K_\rho$  from Eq. (5.5), see, e.g., Refs. [55–57] and Ref. [38], p. 197. The main problem of this approach lies in the accurate calculation of  $C^{\text{NN}}(r)$  from Eq. (5.1) for large distances. The accuracy of the correlation function becomes worse as the distance  $r$  increases, which severely limits the precision of the Fourier transform  $\tilde{C}^{\text{NN}}(q)$ , especially for small  $q$ .

In order to obtain  $K_\rho$  more precisely, we calculate  $\tilde{C}^{\text{NN}}(2\pi/L)$  directly in momentum space using the *real-space* DMRG method. We define

$$N(q) = \frac{1}{L} \langle \Psi_0 | \hat{n}(q) \hat{n}(-q) | \Psi_0 \rangle \quad (5.6)$$

for  $q = 2\pi m/L$  ( $m \geq 1$ ), where  $\hat{n}(q)$  is given by

$$\hat{n}(q) = \hat{n}^+(-q) = \sum_{l,\sigma} e^{-iq(l-r_c)} \hat{c}_{l,\sigma}^\dagger \hat{c}_{l,\sigma}. \quad (5.7)$$

Here,  $r_c = (L+1)/2$  denotes the central position of the chain. Note that  $N(q)$  and  $\tilde{C}^{\text{NN}}(q)$  are different. It is only in the thermodynamic limit, when boundary effects are absent, that they become identical. Therefore,

$$K_\rho(L) = \frac{L}{2} N \left( \frac{2\pi}{L} \right), \quad K_\rho = \lim_{L \rightarrow \infty} K_\rho(L). \quad (5.8)$$

The important idea is to target not only the ground state in the DMRG procedure but also the state  $|\Psi_q\rangle = \hat{n}(-q)|\Psi_0\rangle$ . In this way, a precise DMRG calculation of  $N(q)$  and of  $K_\rho$  from Eq. (5.8) becomes possible. In addition, we note that this method is valid not only for periodic boundary conditions but also for open boundary conditions, which are preferable for the DMRG technique.

### 5.1.2 Infinitesimal doping

Using this method we can investigate  $K_\rho$  even for the infinitesimally doped Mott–Hubbard insulator because we calculate  $N(2\pi/L)$  so that the momentum  $q = 2\pi/L$  transferred from the ground state  $|\Psi_0\rangle$  to  $|\Psi_q\rangle$  is of the same order of magnitude as the phase shifts induced by the introduction of two holes.

As an example, we present the results for the TL parameter for the infinitesimally doped Mott–Hubbard insulator in the half-filled Hubbard model. In Fig. 5.1, we show  $K_\rho(L)$  as a function of the inverse system size keeping  $n = 1 - 2/L$  at several values of  $U/t$ . For  $U \gtrsim 2t$  our systems are larger than the correlation length of the system, and we confirm the bosonization results  $K_\rho^{\text{CDW}}(U > 0, n \rightarrow 1) = n_c^2/2 = 1/2$  numerically.

Note that the extrapolation becomes cumbersome for small  $U/t$ . This can be understood from the exact Bethe-ansatz result [49]. To first order in the doping  $\delta = 1 - n \ll 1$  we have

$$K_\rho(U, 1 - \delta) = \frac{1}{2} + \frac{\delta}{f(U)}, \quad f(U) = \frac{4}{\ln 2} \int_1^\infty \frac{dx}{\sqrt{x^2 - 1}} \frac{1}{\sinh(2\pi tx/U)}. \quad (5.9)$$

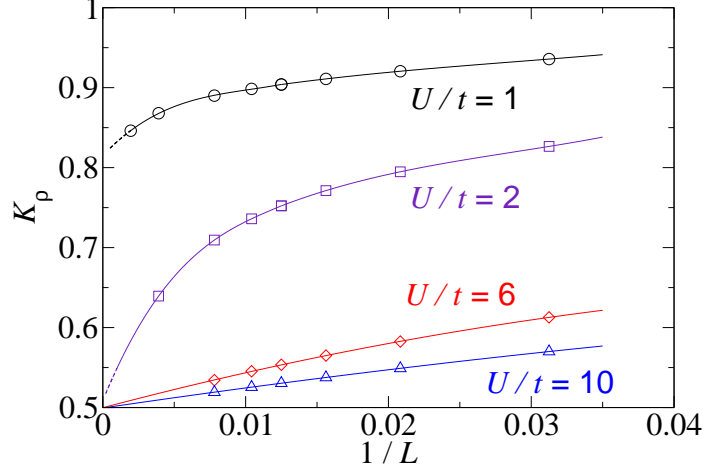


Fig. 5.1:  $K_\rho$  for the infinitesimally doped Mott–Hubbard insulator,  $n = 1 - 2/L$ , as a function of the inverse system size for various interaction strengths. It extrapolates to the exact value  $K_\rho = 1/2$  for all  $U/t$ .

As expected for a transition of Kosterlitz–Thouless (KT) type, the prefactor  $1/f(U)$  diverges exponentially for  $U \rightarrow U_c = 0^+$ ,

$$\frac{1}{f(U \rightarrow 0)} \sim \exp\left[\frac{2\pi t}{U}\right]. \quad (5.10)$$

For infinitesimal doping,  $\delta = 2/L$ , the proper  $1/L$  scaling of  $K_\rho(L)$  sets in for  $L > \mathcal{O}(\exp(2\pi t/U))$ . For this reason, we cannot confirm Eq. (5.9) reliably for small  $U$ . This observation applies to all KT-type CDW transitions which we discuss further in the Sec. 5.2.

### 5.1.3 Comparison with exact results for the Hubbard model for all fillings

Next, we test the accuracy of our method by comparing with the exact solution of the Hubbard model for all band fillings. As a first example we investigate the Hubbard model (2.1), for which  $K_\rho(U; n)$  is known from the Bethe-ansatz solution [48]. We study systems with  $L \leq 128$  sites and open boundary conditions. The number of density matrix states kept is  $m = 1500$ , so that the maximum truncation error is  $3 \times 10^{-6}$ .

In Fig. 5.2a, we show  $K_\rho(L)$  as a function of the inverse system size for several values of  $U/t$ . The band filling is fixed at  $n = 0.1$ , which, apart from the limit  $n \rightarrow 1$ , is the most difficult parameter region in this model because  $K_\rho$  changes significantly as a function of the interaction strength. For all values  $U > 0$ ,  $K_\rho(L)$  is found to decrease monotonically as a function of inverse system size, so that we can extrapolate  $K_\rho$  to the thermodynamic limit systematically by performing a least-squares fit of  $K_\rho$  to a polynomial in  $1/L$ .

In Fig. 5.2b, we compare our results for  $K_\rho^{\text{DMRG}}$  with those from Bethe ansatz for various fillings and interaction strengths. The relative error  $|K_\rho^{\text{DMRG}} - K_\rho^{\text{exact}}|/K_\rho^{\text{exact}}$  is below 0.3% for all DMRG data shown. We reproduce the exact results with a much better accuracy than exact diagonalization [48], the DMRG [38] method based on the Fourier

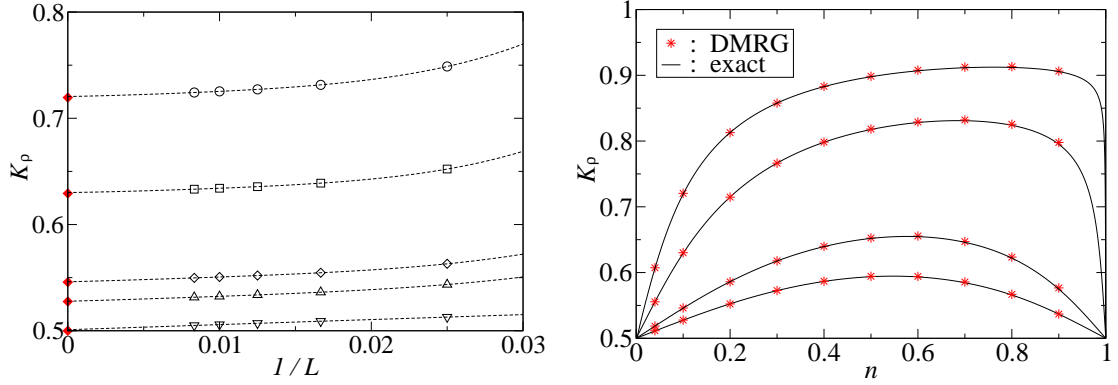


Fig. 5.2: Left:  $K_\rho(L)$  for the one-dimensional Hubbard model at  $n = 0.1$  as a function of the inverse system size for  $U/t=1$  (circles),  $U/t = 2$  (squares),  $U/t = 6$  (diamonds),  $U/t = 10$  (upward triangles), and  $U/t = \infty$  (downward triangles). Filled symbols are the exact values from the Bethe ansatz in the thermodynamic limit. Lines are 4th-order polynomial fits.

Right: TL parameter  $K_\rho$  for the one-dimensional Hubbard model as a function of the density for  $U/t = 1, 2, 6, 10$  (from top to bottom). The full lines are exact values from the Bethe ansatz, stars mark the results from DMRG.

transformation formula (5.4), and the calculation of  $K_\rho$  from the compressibility and the charge velocity [47], see last chapter.

#### 5.1.4 Comparison with exact results for spinless fermions

As our last test we study the extended Hubbard model at quarter filling,  $n = 1/2$  for  $U = \infty$ , which can be mapped onto the exactly solvable Heisenberg XXZ chain. The parameter  $K_\rho$  for the Hubbard model at  $U = \infty$  from the Bethe ansatz is ( $V \leq V_c = 2t$ )

$$K_\rho = \frac{\pi}{4 \arccos[-V/(2t)]}. \quad (5.11)$$

In Fig. 5.3, we show  $K_\rho$  as function of  $V$  for  $U = \infty$  together with the exact result. For this system we use periodic boundary conditions because  $m = 2000$  density-matrix eigenstates are enough to calculate  $K_\rho(L)$  with high precision, and finite-size effects are much smaller for periodic than for open boundary conditions, see the inset in Fig. 5.3. Relative errors  $|K_\rho^{\text{DMRG}} - K_\rho^{\text{exact}}|/K_\rho^{\text{exact}}$  are below 0.5%, even for  $V = 1.95t$  where the system is close to the CDW insulator.

#### 5.1.5 Summary

In this section, we introduced a method to obtain the TL parameter  $K_\rho$  by calculating the Fourier transform of the density-density correlation function directly in momentum space. To this end, we use the real-space DMRG method whereby we target not only the ground state but also the state  $|\Psi_q\rangle = \hat{n}(-q)|\Psi_0\rangle$ . Thus, we can finally investigate the properties of  $K_\rho$  very accurately in any quasi one-dimensional systems with the number of

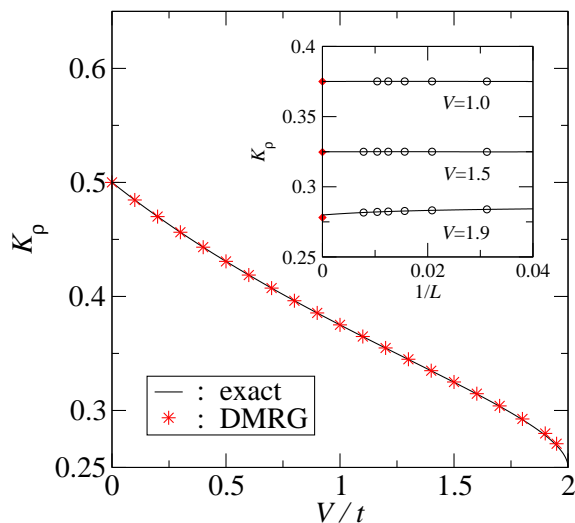


Fig. 5.3: TL parameter  $K_\rho$  for the  $t$ - $U$ - $V$  model at  $U/t = \infty$ ,  $V \leq 2t$  from DMRG (stars) and exact Bethe ansatz (full line). Inset:  $K_\rho(L)$  as a function of inverse system size for periodic boundary conditions.

lattice sites of the order of  $10^3$ . We checked its accuracy in the Hubbard model and the spinless fermion model with nearest-neighbor interaction  $V$  by comparing with the exact results from the Bethe-ansatz solutions. The agreement between both results is excellent. In addition, this method makes it possible to examine the infinitesimally doped system. We demonstrated this for the Hubbard model near half band-filling.

In the following sections, we apply this method to the Hubbard-type models and look for the parameter region where we obtain small values for  $K_\rho$  which correspond to the experimental results for some quasi one-dimensional systems.

## 5.2 Application to the $t$ - $U$ - $V$ model

As a first application, we study the one-dimensional  $t$ - $U$ - $V$  model at (or near) quarter filling. Unfortunately, we have much less exact statements on its physical properties than for the original Hubbard model. The model is exactly solvable only in the limits  $U = \infty$  and/or  $V = \infty$ . In the case of  $U = \infty$  (i.e. spinless fermions), we have the exact solutions from Bethe-ansatz calculations. Using this Bethe-ansatz solutions we can carry out a similar approach as in Sec. 5.1.2. We first compare those exact results with those from the DMRG method.

Except for  $U = \infty$  we have no exact solution of the  $t$ - $U$ - $V$  model. However, the general low-energy properties of the  $t$ - $U$ - $V$  model can be studied using  $g$ -ology (see Sec. 2.2) and functional renormalization group (fRG), which is a recently developed numerical method. We find that our results compare favorable with those from  $g$ -ology and fRG in the weak-coupling limit. Finally, we show the phase diagram of the model with our results for the TL parameter  $K_\rho$  and discuss how to obtain small values for  $K_\rho$  in this model.

Using the DMRG method we study chains with up to 120 sites with open boundary conditions and keep up to  $m = 1500$  density-matrix eigenstates so that the maximum truncation error is about  $10^{-5}t$ .

### 5.2.1 Spinless fermions with nearest-neighbor repulsion

Using a Jordan-Wigner transformation, the one-dimensional spinless fermion model with nearest-neighbor Coulomb interaction  $V$  maps to the XXZ Heisenberg model which has an exact solution from Bethe ansatz.

As shown in Fig. 5.3, there exists a metallic phase for  $0 \leq V \leq V_c = 2t$  in this model. For  $V > 2t$  we have a  $4k_F$ -CDW phase. In this CDW phase we can apply a similar approach as in Sec. 5.1.2, namely, to first order in the doping  $\delta = 1/2 - n \ll 1$  we have

$$K_\rho(U = \infty, V, n_c - \delta) = \frac{1}{8} + \frac{\delta}{2g(V)}, \quad g(V) = \frac{1 + 2 \sum_{n=1}^{\infty} [(-1)^n / \cosh(n\gamma)]}{1 + 2 \sum_{n=1}^{\infty} [1 - \tanh(n\gamma)]}, \quad (5.12)$$

where  $\cosh(\gamma) = V/V_c$ . As expected for a transition of Kosterlitz–Thouless (KT) type, the prefactor  $1/g(V)$  diverges exponentially for  $V \rightarrow V_c^+$ ,

$$g(V \rightarrow V_c) = \frac{2\pi}{\ln 2} \exp \left[ -\frac{\pi^2}{2\sqrt{2}(V/V_c - 1)} \right]. \quad (5.13)$$

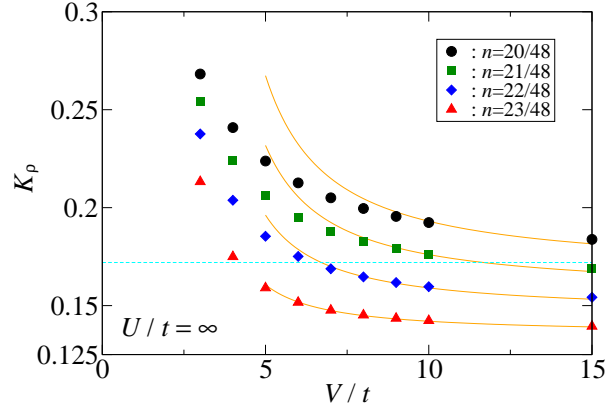


Fig. 5.4: TL parameter  $K_\rho$  in the slightly doped Mott insulator ( $n \simeq 1/2$ ) for spinless fermions as a function of  $V/t$  for various fillings. Lines are the calculated results from Eq. (5.12). The dashed horizontal line marks  $K_\rho = 3 - 2\sqrt{2} \approx 0.17$ .

In Fig. 5.4, we show  $K_\rho$  in the slightly doped system ( $n \approx 1/2$ ) as a function of  $V/t$  for the band filling  $n = 20/48, 21/48, 22/48,$  and  $23/48$  from top to bottom as obtained by Eq. (5.12) and the DMRG method. The agreement for all band fillings is quite good for  $V \gtrsim 8$ , and, naturally, the minimal values of  $K_\rho$  for each band filling come close to

$K_\rho^{\text{CDW}}(n_c = 1/2) = 1/8$  as  $n \rightarrow n_c = 1/2$ . As expected, when the doping  $\delta$  is small we see good agreement between both results. Most importantly, we find small values for  $K_\rho$ . The horizontal line marks  $K_\rho = 3 - 2\sqrt{2} \approx 0.17$  below which the critical exponent for the density of states is larger than unity,  $\alpha \geq 1$ . Therefore, we expect that we can obtain small values for  $K_\rho$  in the  $t$ - $U$ - $V$  model close to quarter filling, see Sec. 5.2.4.

### 5.2.2 Comparison with field theory

In the weak-coupling limit, we can compare with the results from  $g$ -ology and fRG which become exact for  $U, V \rightarrow 0$ . Recently, the fRG [58–60] has been developed as a new computational tool to study interacting Fermi systems. It is particularly efficient in low dimensions. Though technically quite complicated, the fRG provides access to low-dimensional quantum systems in a larger parameter region than  $g$ -ology.

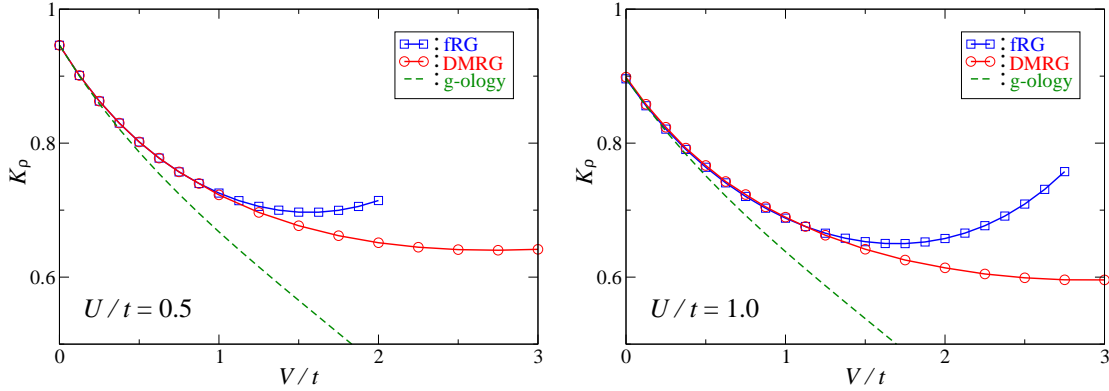


Fig. 5.5: TL parameter  $K_\rho$  for the  $t$ - $U$ - $V$  model at quarter filling as a function of  $V/t$  for  $U/t = 0.5$  and  $U/t = 1.0$ . Results from the DMRG calculations are compared with the results from the one-loop  $g$ -ology calculation and to those from the two-loop fRG method [61].

Quite recently, Andergassen *et al.* [61] have applied the fRG to the one-dimensional  $t$ - $U$ - $V$  model. They calculated the TL parameter  $K_\rho$  with the two-loop fRG. As we can see in Fig. 5.5, the  $g$ -ology results agree with the DMRG data for  $U/t \leq 1$  and  $V/t \leq 0.5$ . The fRG results are applicable up to  $U/t \leq 1.5$  and  $V/t \leq 1.5$ . In fact,  $g$ -ology is exact to first-order in the Coulomb interaction, and the two-loop fRG gives the exact second-order result in  $U, V$  for  $K_\rho$ .

The favorable comparison with the weak coupling renormalization group approaches confirms the results from  $g$ -ology and the fRG and shows again that our method works very well for the  $t$ - $U$ - $V$  model at quarter filling.

### 5.2.3 Phase diagram at quarter filling

We proceed to investigate the TL parameter  $K_\rho$  in the  $t$ - $U$ - $V$  model at quarter filling in the whole  $U$ - $V$  parameter space. In Fig. 5.6, we show the phase diagram together with the contour lines for  $K_\rho$ . Three different phases are found, namely, a “superconducting phase” ( $K_\rho > 1$ ) where the system has dominant superconducting fluctuations, a metallic phase

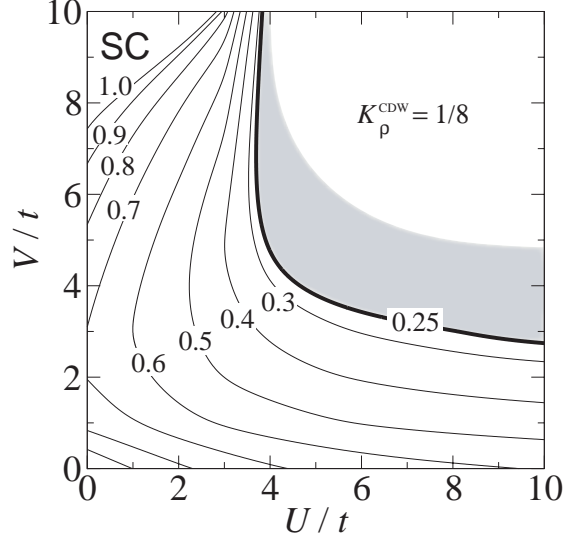


Fig. 5.6: Contour map for the TL parameter  $K_\rho$  in the  $U$ - $V$  plane of the  $t$ - $U$ - $V$  model at quarter filling. The bold line represents the boundary of the metal-insulator transition. The infinitesimally doped CDW insulator has  $K_\rho^{\text{CDW}} = 1/8$ . The shaded area indicates the region with an exponentially small gap.

( $1/4 \leq K_\rho \leq 1$ ), and a  $4k_F$ -CDW insulator [see Fig. 2.1 (a)] beyond the critical line. The results are in good agreement with previous work [10, 11].

On the CDW transition line we find  $K_\rho^* = n_c^2 = 1/4$ . For large  $U$ , this transition line approaches  $V_c/t = 2$ , the exact value for  $U/t = \infty$ . Moreover,  $K_\rho^{\text{CDW}} = n_c^2/2 = 1/8$  for the infinitesimally doped CDW insulator, in agreement with field theory. The parameter region where finite-size effects are prominent due to an exponentially small gap is shaded in Fig. 5.6. Outside this region, we can determine the TL parameter reliably.

#### 5.2.4 Doped Mott insulator

As discussed above, we confirm the field-theoretical predictions for the  $t$ - $U$ - $V$  model. Now, we can go one step further and look for the regions where we can find small values for  $K_\rho$ . In the infinitesimally doped CDW phase we find  $K_\rho^{\text{CDW}} = 1/8$ . Our extrapolated results for the slightly doped system ( $\delta = 1/24 \approx 4\%$ ) are shown in Fig. 5.7 as a function of  $V/t$  for  $U/t = 6, 10, \infty$ . Deep in the CDW phase ( $U/t \gtrsim 5, V/t \gtrsim 6$ ) neither  $U$  nor  $V$  have a large influence on  $K_\rho$ .

As expected, the slightly doped CDW insulators displays much smaller values for  $K_\rho$  than the metallic quarter-filled phase where  $K_\rho \geq 1/4$ . Nevertheless, the minimal value for  $K_\rho$  is  $K_\rho(U = \infty, V = \infty, n_c - \delta) = 1/8 + \delta/2$  so that its minimal value is 0.145 even at 4% doping. As seen from Fig. 5.7, at doping of 4%,  $U/t = 10, V/t = 8$  are barely large enough to reduce  $K_\rho$  below  $K_\rho = 3 - 2\sqrt{2}$  which corresponds to  $\alpha \geq 1$ . We see that very small  $K_\rho < 0.17$  requires very large interaction strengths and/or very small doping.

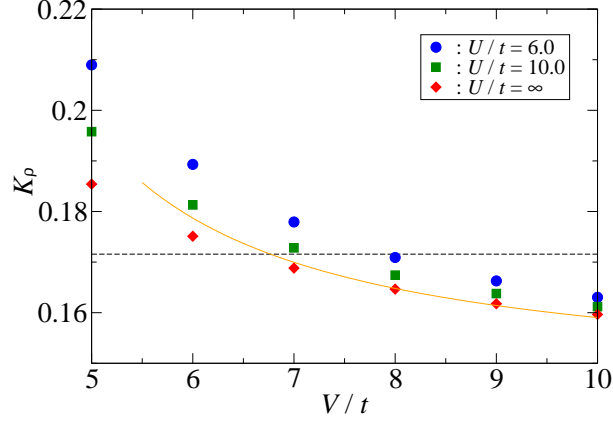


Fig. 5.7: TL parameter  $K_\rho$  for the  $t$ - $U$ - $V$  model as a function of  $V/t$  at filling  $n = 11/24$ . The full line is the result (5.12), the dashed horizontal line marks  $K_\rho = 3 - 2\sqrt{2} \approx 0.17$ .

### 5.2.5 Summary

In this section, we investigated the  $t$ - $U$ - $V$  model at quarter filling. For  $U = \infty$  we have exact solutions. We carried out a Taylor expansion for small doping in the CDW phase for  $U = \infty$  and obtained small values for  $K_\rho$  in the slightly doped system ( $n \approx 1/2$ ). Our DMRG results agree very well with the exact results. Next, we compared our results for the  $t$ - $U$ - $V$  model at quarter filling and weak coupling with those from the  $g$ -ology and the fRG. As expected, we found a good agreement.

We obtained the phase diagram in the  $t$ - $U$ - $V$  model at quarter filling. There are three different phases, namely, superconducting phase, metallic phase, and  $4k_F$ -CDW insulating phase. We also verified the field-theoretical predictions of the TL parameter  $K_\rho$  at quarter filling,  $K_\rho^* = n_c^2 = 1/4$  and  $K_\rho^{\text{CDW}} = n_c^2/2 = 1/8$ . As in the case of spinless fermions, we examined the TL parameter  $K_\rho$  in the slightly doped system ( $n \approx 1/2$ ). We finally obtained very small  $K_\rho < 0.17$  which corresponds to  $\alpha > 1$ , but only with very large interaction strengths  $U \gtrsim 8$  and very small doping  $\delta \lesssim 4\%$ .

## 5.3 Application to the $t$ - $U$ - $V_1$ - $V_2$ model

In this section, we investigate the  $t$ - $U$ - $V_1$ - $V_2$  model at  $n = 1/3$ . As explained in Sec. 2.1.2, we will find a  $4k_F$ -CDW insulator for enough large interactions  $U$ ,  $V_1$  and  $V_2$ . To examine this metal-insulator transition, we need to calculate  $\Delta_c$  which is defined in Eqs. (4.4) and (4.5). We limit our investigation to the case  $U/t = 20$ .

Using the DMRG method we study chains with up to 120 sites with open boundary conditions and keep up to  $m = 2000$  density-matrix eigenstates so that the maximum truncation error is about  $10^{-5}t$ . The next nearest-neighbor Coulomb interaction  $V_2$  makes DMRG calculations more difficult than in the  $t$ - $U$ - $V$  model in the last section so that we need larger density-matrix eigenstates in this system.

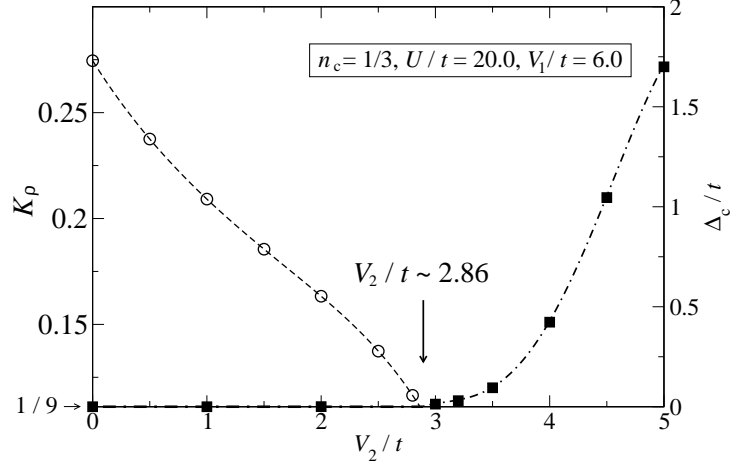


Fig. 5.8: Charge gap  $\Delta_c$  (squares) and TL parameter  $K_\rho$  (circles) for the  $t$ - $U$ - $V_1$ - $V_2$  model at  $n_c = 1/3$  for  $U/t = 20$  and  $V_1/t = 6$ . Lines are guides to the eye.

### 5.3.1 Commensurate filling

Firstly, we look for the critical interaction strength  $V_{2,c}$  where the charge gap  $\Delta_c$  closes. Our results for  $\Delta_c$  for  $U/t = 20$  and  $V_1/t = 6$  are shown in Fig. 5.8. As we can see in this figure, the charge gap  $\Delta_c$  increases almost linearly when  $V_2/t$  is large, and vanishes rapidly close to  $V_{2,c}$ . We extrapolate  $\Delta_c(V_2 \searrow V_{2,c}) \rightarrow 0$ , and obtain  $V_{2,c}/t \simeq 2.86$ . The TL parameter  $K_\rho$  is also shown in Fig. 5.8. Similar to spinless fermions (see Fig. 5.3),  $K_\rho$  decreases rapidly close to the metal-insulator transition. We extrapolate  $K_\rho(V_2 \nearrow V_{2,c}) \rightarrow 1/9$  and obtain the critical interaction strength  $V_{2,c}/t \simeq 2.86$ , in agreement with the extrapolation of the charge gap  $\Delta_c$ . Thus, it is evident that  $\Delta_c/t$  is finite for  $V_2/t \geq 2.86$ , so that the system is insulating, and  $\Delta_c/t$  vanishes for  $V_2/t \leq 2.86$ , within the accuracy of the extrapolation (error smaller than  $10^{-4}$ ).

Furthermore, in the metallic region we see that  $K_\rho > 1/9$  when the charge gap is zero and  $K_\rho^* = n_c^2 = 1/9$  at the critical point, in agreement with field theory.

### 5.3.2 Infinitesimal doping

It is interesting to calculate  $K_\rho$  for the  $4k_F$ -CDW insulator at infinitesimal doping. In Fig. 5.9, we show  $K_\rho(L)$  as function of the inverse system size keeping  $n = 1/3 - 2/L$  for  $U/t = 20$  at several values of  $V_1/t$  and  $V_2/t$ . As we can see in this figure, all data extrapolate to the value  $0.056 \simeq 1/18$ . Thus, we confirm again the field theory results  $K_\rho^{\text{CDW}} = n_c^2/2 = 1/18$  at infinitesimal doping of the  $4k_F$ -CDW insulator.

It is seen that very small  $K_\rho$ -values can be obtained for the slightly doped CDW insulator. Note, however, that the parameters of this model study are not representative for a real material. Nevertheless, it shows that electron-electron interactions can indeed give rise to very small values of  $K_\rho$ .

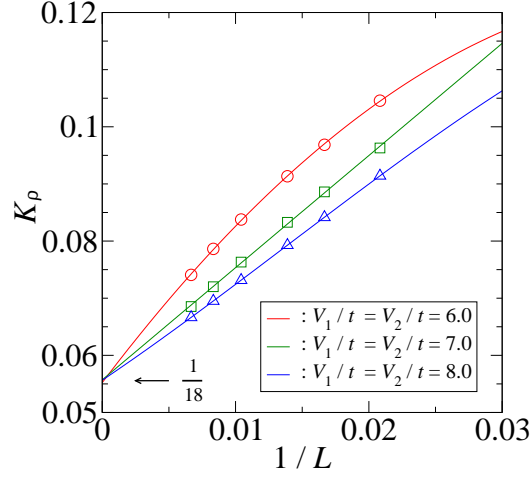


Fig. 5.9:  $K_\rho(L)$  for the infinitesimally doped Mott–Hubbard insulator,  $n = 1/3 - 2/L$ , as a function of the inverse system size for various interaction strengths. For  $1/L \rightarrow 0$  all lines extrapolate to the value  $K_\rho^{\text{CDW}} = n_c^2/2 = 1/18$ .

### 5.3.3 Summary

In this section, we investigated the  $t$ - $U$ - $V_1$ - $V_2$  model at  $n = 1/3$ . As expected, we found the  $4k_{\text{F}}$ -CDW phase at large enough interaction strengths. We determined the critical interaction strength  $V_{2,c}/t \sim 2.86$  for  $U/t = 20$  and  $V_1/t = 6$ . At the transition point we obtained  $K_\rho^* = n_c^2 = 1/9$ , and in the CDW phase  $K_\rho^{\text{CDW}} = n_c^2/2 = 1/18$  for infinitesimal doping, in agreement with field theory.

This case study shows that the electron–electron interaction can cause very small values of  $K_\rho$  in the vicinity of a CDW transition.

## 5.4 Application to the Peierls–Hubbard model

In this section, in order to examine the effect of dimerization, we study the Peierls–Hubbard model, i.e.,  $V = 0$  in Eq. (2.13). We may assume that the weak-coupling theory works well for small  $U/t_1$ . Therefore, the weak-coupling limit will be helpful to estimate  $K_\rho$  and to check the performance of our method. Next, we provide the TL parameter  $K_\rho$  as a function of the interaction strength for all  $U/t_1$  and compare it to the single-band Hubbard model (SHM). Most importantly, at quarter filling the system becomes Mott insulating for all dimerization and interaction strengths, since each electron localizes on a dimer, i.e., the quarter-filled PHM can be exactly mapped to the half-filled Hubbard model for small energies. This situation is clearly reflected in the behavior of  $K_\rho$ .

In this model, the chain length should be multiples of four because the system describes two bands due to the dimerization. Using the DMRG method, we study chains with up to 256 sites and open boundary conditions. We keep up to  $m = 2000$  density-matrix eigenstates, so that the maximum truncation error is about  $10^{-6}t_1$ .

Due to the dimerization we need to redefine Eqs. (5.6)-(5.8) as follows:

$$N_{\text{PHM}}(q) = \frac{2}{L} \langle \Psi_0 | \hat{n}(q) \hat{n}(-q) | \Psi_0 \rangle \quad (5.14)$$

for  $q = 4\pi m/L$  ( $m \geq 1$ ), where  $\hat{n}(q)$  is given by

$$\hat{n}_{\text{PHM}}(q) = \hat{n}_{\text{PHM}}^+(-q) = \sum_{l=1}^{L/2} \sum_{\sigma} e^{-iq(l-r_c)} (\hat{c}_{2l-1,\sigma}^\dagger \hat{c}_{2l-1,\sigma} + \hat{c}_{2l,\sigma}^\dagger \hat{c}_{2l,\sigma}). \quad (5.15)$$

Here,  $r_c = (L/2 + 1)/2$ . Then, we can extrapolate as

$$K_\rho(L) = \frac{L}{4} N \left( \frac{4\pi}{L} \right), \quad K_\rho = \lim_{L \rightarrow \infty} K_\rho(L). \quad (5.16)$$

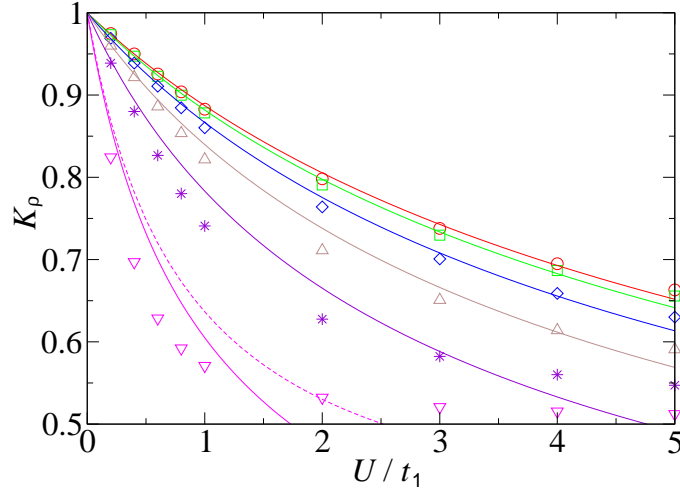


Fig. 5.10: TL parameter  $K_\rho$  for the Peierls–Hubbard model from the DMRG (symbols) in comparison with  $g$ -ology (solid lines), as a function of  $U/t_1$  for  $t_2/t_1 = 1, 0.9, 0.5, 0.3,$  and  $0.1$  (from top to bottom) at  $n_c = 0.4$ . Dotted line shows the  $g$ -ology result for the reduced single-band model at strong dimerization,  $t_2/t_1 = 0.1$ .

#### 5.4.1 Comparison with field theory

In the  $g$ -ology method, the  $g$  couplings of the model are obtained as  $g_1 = g_2 = g_4 = U/2$ , since the interaction is the  $SU(2)$  symmetric. Therefore, one can estimate the TL parameter  $K_\rho$  as [62]

$$K_\rho = \sqrt{\frac{2\pi v_F}{2\pi v_F + U}}, \quad (5.17)$$

where the Fermi velocity  $v_F$  is given by

$$v_F = \frac{t_1 t_2 \sin k_F}{\sqrt{t_1^2 + t_2^2 + 2t_1 t_2 \cos(k_F)}}. \quad (5.18)$$

In Fig. 5.10, we compare the TL parameter  $K_\rho$  from the DMRG method with those obtained by the  $g$ -ology method as a function of  $U/t_1$  for various dimerization strength  $t_2/t_1$  at band-filling  $n = 0.4$ . The system is always metallic for all interaction strengths  $U/t_1$ . For any dimerization strength  $t_2/t_1$ ,  $K_\rho$  decreases with increasing  $U/t_1$  and approaches to 0.5 for  $U = \infty$ , as expected from well-known results in the Hubbard model without dimerization. When  $t_2/t_1$  is close to unity, i.e., the dimerization is small, we can see a good agreement between the  $g$ -ology results and those from the DMRG. For fixed  $U/t_1$ ,  $K_\rho$  decreases slowly as  $t_2/t_1$  decreases and we may explain this by slowly reducing the effective bandwidth  $W$ . On the contrary, when the dimerization is large ( $t_2/t_1 \lesssim 0.5$ ),  $g$ -ology substantially deviates from the DMRG, and  $K_\rho$  decreases rapidly with decreasing  $t_2/t_1$ . This implies that the umklapp scattering strength increases, even for fixed  $U/t_1$ , as  $t_2/t_1$  decreases. For large dimerization, low-energy states of the dimerized Hubbard model at filling  $n$  could be reduced to those of the single-band Hubbard model at filling  $2n$  with the effective onsite repulsion [63]

$$U_{\text{eff}} = 2t_1 - \frac{\sqrt{U^2 + 16t_1^2} - U}{2}, \quad (5.19)$$

and the effective hopping integral  $t_{\text{eff}} = t_2/2$ . In the following, we denote this effective model as RSHM, the reduced single-band Hubbard model. Note that,  $U_{\text{eff}}/t_{\text{eff}}$  produces the umklapp scattering processes and it can be large even when  $U/t_1$  is small. The  $g$ -ology results for  $K_\rho$  in the RSHM for  $t_2/t_1 = 0.1$  are also shown in Fig. 5.10 as a dotted line. They agree well with the DMRG results of the PHM for  $t_2/t_1 = 0.1$  which confirms the applicability of the mapping.

#### 5.4.2 Effect of dimerization on $K_\rho$

We now investigate the TL parameter  $K_\rho$  as a function of the band filling  $n$  and the interaction strength  $U/t_1$ . In Fig. 5.11, we show  $K_\rho$  as a function of the filling  $n$  for various interaction strengths  $U/t_1$  and dimerizations, (a)  $t_2/t_1 = 0.9$ , (b)  $t_2/t_1 = 0.5$ , and (c)  $t_2/t_1 = 0.1$ . We also plot in this figure exact Bethe-ansatz solutions of  $K_\rho$  in the one-dimensional Hubbard model to investigate the effect of dimerization. For a proper comparison, the hopping integral of the SHM is set to  $t = (t_1 + t_2)/2$  so that the effective band width  $W$  should be same as that of the PHM.

For weak dimerization, in Fig. 5.11 (a), we can see the good agreement of the results between the SHM and the PHM except for a quite narrow range around quarter band-filling,  $n_c = 0.5$ . This means that the TLL properties are not affected by small dimerizations except for the narrow region around  $n_c = 0.5$ . There, the system is Mott insulating for all dimerization and interaction strength because the PHM can be mapped to the half-filled single-band Hubbard model. Hence, we may expect a marked increase of the umklapp scattering processes due to the commensurate filling effect around  $n_c = 0.5$ . In addition, we find that  $K_\rho(n_c \rightarrow 0.5) \rightarrow 1/2$  for all dimerization strengths. This corresponds to  $K_\rho = 0.5$  of the SHM around half filling.

When the dimerization strength is intermediate [Fig. 5.11 (b)], the values of  $K_\rho$  in the PHM are much smaller than the ones in the SHM. The umklapp scattering due to the dimerization starts to increase, and, thus, we can also see a rapid decrease of  $K_\rho$  around  $n_c = 0.5$ . We note that  $K_\rho$  of the PHM is somewhat larger than that of the SHM in

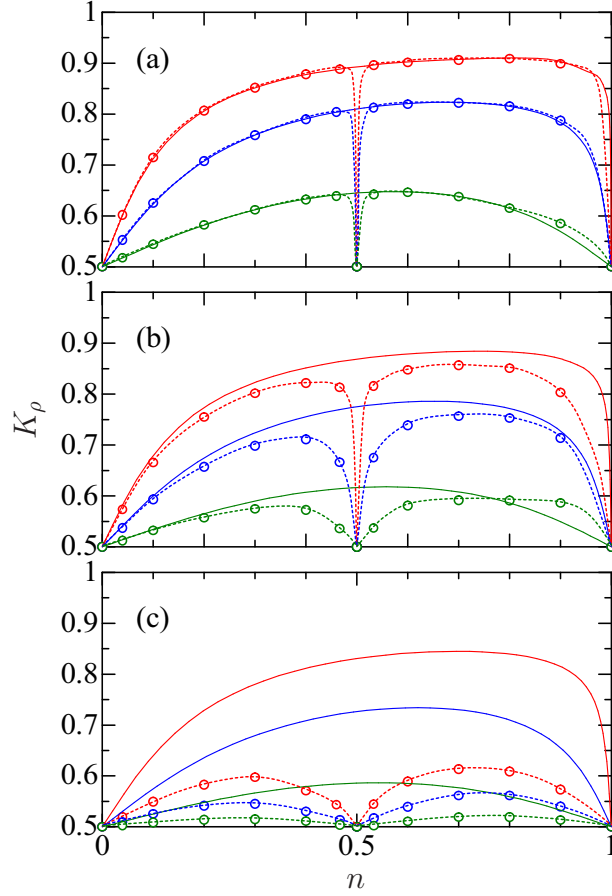


Fig. 5.11: TL parameter  $K_\rho$  for the PHM as a function of band filling  $n$  and interaction strength  $U/t_1$  for dimerization strength  $t_2/t_1 = 0.9$  (a),  $0.5$  (b), and  $0.1$  (c).  $U/t_1 = 1, 2,$  and  $6$  from top to bottom in each figure. Open circles denote the DMRG results and dotted lines are a guide to the eye. Solid lines denote  $K_\rho$  of the SHM with hopping integral  $t = (t_1 + t_2)/2$  and interaction strength  $U$ .

strong coupling ( $U/t_1 \gtrsim 4$ ) and high concentration ( $n_c \sim 1$ ). The scattering processes of the PHM compete with those of the SHM. Similar behavior can be seen in the results for  $t_2/t_1 = 0.9$ .

When the dimerization strength is large [Fig. 5.11 (c)], the values of  $K_\rho$  in the PHM are much smaller than the ones of the SHM with the effective bandwidth. Because of the strong effective ‘onsite’ coupling  $U_{\text{eff}}/t_{\text{eff}}$  the umklapp scattering strength becomes very large. Therefore, the mapping of the PHM into the SHM with the reduced band-filling and the strong effective Coulomb repulsion can be performed almost exactly. For instance, the effective couplings at  $t_2/t_1 = 0.1$  are estimated from Eq. (5.19) as  $U_{\text{eff}}/t_{\text{eff}} = 8.8, 15.3,$  and  $27.9$  for  $U/t_1 = 1, 2,$  and  $6$ , respectively. In Fig. 5.12, we compare the TL parameter  $K_\rho$  in the PHM at  $t_2/t_1 = 0.1$  as a function of band-filling  $n$  with the one in the RSHM with the estimated effective interaction strengths  $U_{\text{eff}}/t_{\text{eff}}$ . The band-filling  $n$  of the PHM

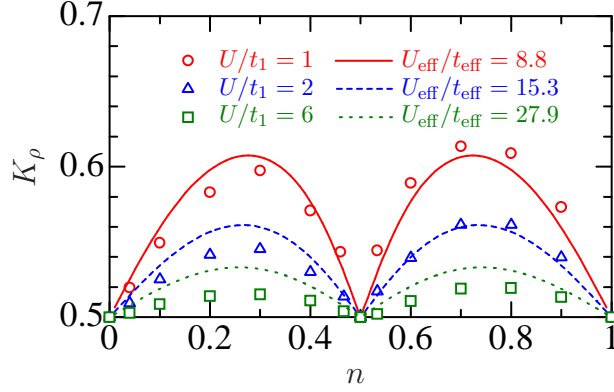


Fig. 5.12: Comparison of the TL parameter  $K_\rho$  in the PHM with  $K_\rho$  in the RSHM with the effective interaction strengths  $U_{\text{eff}}/t_{\text{eff}}$  from Eq. (5.19) as a function of band-filling  $n$  at  $t_2/t_1 = 0.1$ . The band-filling of the PHM corresponds to  $2n$  of the SHM.

corresponds to the one  $2n$  of the SHM. As expected, in this figure we can see a reasonable agreement between both results and we confirm the efficiency of the mapping of the PHM into the RSHM for strong dimerization.

### 5.4.3 Summary

In this section, we investigated the Peierls–Hubbard model using the DMRG method to examine the effect of dimerization to the TL parameter  $K_\rho$ . We first checked the performance of our method for the model on the weak-coupling limit. As expected, for small dimerization the agreement between  $g$ -ology and the DMRG is quite good, and becomes worse as the dimerization strength increases.

Next, we obtained  $K_\rho$  as a function of band-filling  $n$ . Since the system becomes Mott insulating at quarter filling for all dimerization and interaction strengths, the values of  $K_\rho$  come close to 0.5 as  $n \rightarrow 1/2$ . This corresponds to  $K_\rho \rightarrow K_\rho^{\text{CDW}} = 1/2$  in the SHM near half band-filling. For weak dimerization, the TLL properties are not strongly affected except for the narrow region around quarter filling and the values of  $K_\rho$  for this parameter region can be reproduced by the ones in the SHM with the effective bandwidth. On the other hand, for large dimerization the values for  $K_\rho$  are much smaller than the ones in the SHM with the same effective bandwidth. In this case the PHM can be mapped into the RSHM with a much larger effective strong onsite Coulomb interaction. We verified this mapping for strong dimerization.

In general, dimerization decreases the values of  $K_\rho$  by decreasing the effective bandwidth or increasing the effective Coulomb repulsion. However, the minimal value of  $K_\rho$  is not affected by dimerization in the Peierls–Hubbard model as compared to the SHM.



## 6 Conclusions

In the first part of this thesis, we used exact numerical methods to calculate the Tomonaga–Luttinger parameter  $K_\rho$ . This parameter determines all critical exponents, e.g., the exponent  $\alpha$  for the density of states near the Fermi energy, which has been derived from experiment. The estimated  $\alpha$  is larger than unity which would imply  $K_\rho \lesssim 0.17$ , a value which cannot be understood within the bare Hubbard model where  $K_\rho \geq 0.5$ , i.e.,  $\alpha_H \leq 1/8$ . In order to reconcile this discrepancy between theoretical and experimental results, extended Hubbard models need to be investigated which, however, are not analytically solvable. Therefore, we developed new methods to calculate  $K_\rho$  very accurately using the ED and DMRG methods. The best method to obtain the Tomonaga–Luttinger parameter  $K_\rho$  is based on the DMRG. Our central result is the observation that small values of  $K_\rho$  are obtained for large interaction strengths and small doping of charge-density-wave insulators. If this situation does not apply for a quasi one-dimensional material other mechanism, e.g., impurities, must be responsible for the observed reduced density of states near the Fermi energy.

As new technical developments we proposed two methods to obtain  $K_\rho$  for generic one-dimensional model Hamiltonians. First, in Chap. 4, we obtained  $K_\rho$  from the charge velocity  $v_c$  using the ED method and the compressibility  $\kappa$  using the DMRG method. We applied the method to the  $t$ - $U$ - $V_1$ - $V_2$  model at quarter filling. In its accurate phase diagram in which we include the values for  $K_\rho$ , there exist two CDW phases with  $q = 2k_F$  and  $4k_F$ , in between there appears a wide region of a Tomonaga–Luttinger liquid.  $K_\rho$  is maximum around  $V_2 = V_1/2$  and smallest at the phase boundaries,  $K_\rho^* = 1/4$ , in agreement with field theory. However, the first method is not accurate enough to investigate  $K_\rho$  in the vicinity of the CDW insulator or for infinitesimal doping. Therefore, in Chap. 5, we developed a second method to calculate  $K_\rho$  from the density-density correlation function. Since it is based on the DMRG method, we can investigate chains with up to the system size  $L = \mathcal{O}(10^3)$  with a relative error below 0.3% for the Hubbard model.

As a first example, we applied the method to the  $t$ - $U$ - $V$  model at quarter filling. We obtained its phase diagram in which we found a superconducting phase, a metallic phase, and a  $4k_F$ -CDW insulator phase. We confirmed the field-theoretical predictions,  $K_\rho^* = n_c^2 = 1/4$  and  $K_\rho^{\text{CDW}} = n_c^2/2 = 1/8$  in this model. Then, we estimated  $K_\rho$  in the slightly doped Mott insulator. As expected, the slightly doped CDW insulator displays smaller values for  $K_\rho$  than we find at the boundaries of the interaction-driven Mott transition,  $K_\rho^* = 1/4$ . However, very small  $K_\rho \leq 0.17$ , and, thus,  $\alpha \geq 1$ , requires large interaction strengths and small doping,  $\delta \leq 2\%$ . As a second example, we investigated the  $t$ - $U$ - $V_1$ - $V_2$  model at  $n_c = 1/3$ . We again verified the field-theoretical predictions  $K_\rho^* = 1/9$  and  $K_\rho^{\text{CDW}} = 1/18$ .

As our third and last example, we investigated the Peierls–Hubbard model in order to examine the effects of dimerization. At quarter filling the system becomes Mott insulating for all dimerization and interaction strengths. This situation is clearly reflected in the behavior of  $K_\rho$ . In general, for weak dimerization the TLL properties are not strongly

affected by the dimerization except for the narrow region around quarter filling. The values of  $K_\rho$  for weak dimerization can be reproduced by those of the single-band Hubbard model with an effective bandwidth. On the other hand, for large dimerization the system can be mapped onto a reduced single-band Hubbard model with strong onsite Coulomb interactions and twice the band-filling. Thus, dimerization decreases the values of  $K_\rho$  by decreasing the effective bandwidth or by increasing the effective Coulomb repulsion. However, the minimal value of  $K_\rho$  is not affected by dimerization in the Peierls–Hubbard model compared to the single-band Hubbard model. Therefore, dimerization is not the primary reason for small values of  $K_\rho$ .

## **Part II**

### **Charges in a spin-disordered background**



## 7 Motivation: disordered spin background

In this chapter we review the Mott–Hubbard insulator in infinite dimensions and the Harris–Lange model. They are examples for the motion of charges in a spin-disordered background. For such systems, perturbation theory can be performed to high orders and even exact solutions become possible. These results serve as test cases for numerical investigations.

### 7.1 Mott–Hubbard insulator in infinite dimensions

In this section, we review the Mott–Hubbard insulator in the single-band Hubbard model in infinite dimensions as our first example of the system in the spin-disordered regime. In order to examine this model, we first introduce the Dynamical Mean-Field Theory (DMFT) which should be solved numerically. Then, we give a short account of the results from the strong-coupling expansion and a comparison with numerical data. Lastly, we discuss the Mott–Hubbard transition in this model where the best available treatments using the Dynamical Density-Matrix Renormalization Group (DDMRG) method lead to conflicting results.

#### 7.1.1 Dynamical Mean-Field Theory (DMFT)

We start from the Hubbard model on a Bethe lattice with connectivity  $Z \rightarrow \infty$ ,

$$\hat{\mathcal{H}} = \sum_{\mathbf{i}, \mathbf{j}; \sigma} t_{\mathbf{i}, \mathbf{j}} \hat{c}_{\mathbf{i}, \sigma}^\dagger \hat{c}_{\mathbf{j}, \sigma} + \sum_{\mathbf{i}} \left( \hat{n}_{\mathbf{i}, \uparrow} - \frac{1}{2} \right) \left( \hat{n}_{\mathbf{i}, \downarrow} - \frac{1}{2} \right), \quad (7.1)$$

where  $\hat{c}_{\mathbf{i}, \sigma}^\dagger$ ,  $\hat{c}_{\mathbf{i}, \sigma}$  are creation and annihilation operators for electrons with spin  $\sigma = \uparrow, \downarrow$  on site  $\mathbf{i}$  (here bold characters mean vectors). The matrix elements  $t_{\mathbf{i}, \mathbf{j}}$  are the electron transfer amplitudes between sites  $\mathbf{i}$  and  $\mathbf{j}$ , and  $t_{\mathbf{i}, \mathbf{i}} = 0$ .  $\hat{n}_{\mathbf{i}, \sigma} = \hat{c}_{\mathbf{i}, \sigma}^\dagger \hat{c}_{\mathbf{i}, \sigma}$  is the local density operator at site  $\mathbf{i}$  for spin  $\sigma$ . Since we are interested in the Mott insulating phase, we consider exclusively a half-filled band where the number of electrons  $N$  equals the number of lattice sites  $L$ . The electron transfer is restricted to nearest neighbors, i.e.,  $t_{\mathbf{i}, \mathbf{j}} = -t/\sqrt{Z}$  when  $\mathbf{i}$  and  $\mathbf{j}$  are nearest neighbors and zero otherwise. The limit  $Z \rightarrow \infty$  is implicitly understood henceforth. In the following, we take  $t \equiv 1$  as our unit of energy. We note that the strong-coupling expansion is directly applied to the Hamiltonian (7.1).

In the limit of infinite dimensions and under the condition of convergence of perturbation theory in weak and strong coupling, the Hubbard model can be mapped to the single-impurity Anderson model (SIAM) in ‘star geometry’, see Fig. 7.1, which needs to be solved *self-consistently*. The model describes the hybridization of an impurity site with Hubbard interaction to  $n_s - 1$  bath sites without interaction at energies  $\epsilon_l$ . The hybridization matrix elements  $V_l$  are real, positive numbers. Let  $\hat{d}_\sigma^\dagger$ ,  $\hat{d}_\sigma$ ,  $\hat{\psi}_{\sigma, l}^\dagger$  and  $\hat{\psi}_{\sigma, l}$  denote creation and annihilation operators for electrons with spin  $\sigma = \uparrow, \downarrow$  on the impurity and the bath

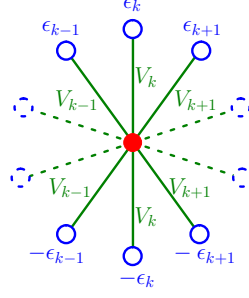


Fig. 7.1: Star geometry

site  $l$ , respectively. Then, the Hamiltonian reads

$$\begin{aligned} \hat{\mathcal{H}}_{\text{SIAM}} &= \sum_{\sigma} \sum_{l=1}^{n_s-1} \epsilon_l \hat{\psi}_{\sigma,l}^{\dagger} \hat{\psi}_{\sigma,l} + U \left( \hat{d}_{\uparrow}^{\dagger} \hat{d}_{\uparrow} - \frac{1}{2} \right) \left( \hat{d}_{\downarrow}^{\dagger} \hat{d}_{\downarrow} - \frac{1}{2} \right) \\ &+ \sum_{\sigma} \sum_{l=1}^{n_s-1} V_l (\hat{\psi}_{\sigma,l}^{\dagger} \hat{d}_{\sigma} + \hat{d}_{\sigma}^{\dagger} \hat{\psi}_{\sigma,l}). \end{aligned} \quad (7.2)$$

The parameters  $\epsilon_l$  and  $V_l$  appear in a simple combination in the *hybridization function*

$$\Delta(\omega) = \pi \sum_l |V_l|^2 \delta(\omega - \epsilon_l), \quad (7.3)$$

which here plays the role of a mean field. Because of its frequency dependence it is a *dynamical* mean field. Since the bath describes the same electrons as those on the local site,  $\Delta(\omega)$  has to be determined from the self-consistency condition

$$G[\Delta(\omega)] = \int d\epsilon D_0(\epsilon) \{ \omega - \Sigma[\Delta(\omega)] - \epsilon \}^{-1}, \quad (7.4)$$

where the self-energy term  $\Sigma[\Delta(\omega)] \equiv \Delta(\omega) - 1/G[\Delta(\omega)] + \omega$  is a frequency-dependent potential, and  $D_0(\epsilon)$  is the bare density of states of width  $W$  for the Bethe lattice ( $Z \rightarrow \infty$ ) [64],

$$D_0(\epsilon) = \frac{4}{\pi W} \sqrt{1 - \left( \frac{2\epsilon}{W} \right)^2} \quad \text{for } |\epsilon| \leq \frac{W}{2}. \quad (7.5)$$

The time-dependent local single-particle Green function at zero temperature is given by

$$G(t) = -i \frac{1}{L} \sum_{i,\sigma} \hat{\mathcal{T}} [\hat{c}_{i,\sigma}(t) \hat{c}_{i,\sigma}^{\dagger}], \quad (7.6)$$

where  $\hat{\mathcal{T}}$  is the time-ordering operator,  $\langle \dots \rangle$  implies the average over the degenerate ground states with energy  $E_0$ , and (taking  $\hbar \equiv 1$ )

$$\hat{c}_{i,\sigma}(t) = \exp(i\hat{\mathcal{H}}t) \hat{c}_{i,\sigma} \exp(-i\hat{\mathcal{H}}t) \quad (7.7)$$

is the annihilation operator in the Heisenberg picture.

In the insulating phase, we can identify the contributions from the lower (LHB) and upper (UHB) Hubbard bands to the Fourier transform of the local Green function ( $\eta = 0^+$ ),

$$\begin{aligned} G(\omega) &= \int_{-\infty}^{\infty} dt e^{i\omega t} G(t) = G_{\text{LHB}}(\omega) + G_{\text{UHB}}(\omega), \\ G_{\text{LHB}}(\omega) &= \frac{1}{L} \sum_{i,\sigma} \langle \hat{c}_{i,\sigma}^\dagger [\omega + \hat{\mathcal{H}} - E_0 - i\eta]^{-1} \hat{c}_{i,\sigma} \rangle, \\ G_{\text{UHB}}(\omega) &= -G_{\text{LHB}}(-\omega). \end{aligned} \quad (7.8)$$

The last equality follows from the particle-hole symmetry. Furthermore, the density of states for the lower Hubbard band can be obtained from the imaginary part of the Green function (7.8) for real arguments

$$D_{\text{LHB}}(\omega) = \frac{1}{\pi} \text{Im} G_{\text{LHB}}(\omega) = \frac{1}{L} \sum_{i,\sigma} \langle \hat{c}_{i,\sigma}^\dagger \delta(\omega + \hat{\mathcal{H}} - E_0) \hat{c}_{i,\sigma} \rangle, \quad (7.9)$$

with  $\omega \leq -\Delta(U)/2 < 0$ , where  $\Delta(U)$  is the single-particle gap. Particle-hole symmetry yields a symmetric density of states around  $\omega = 0$  at half band-filling

$$D(\omega) = D_{\text{LHB}}(\omega) + D_{\text{UHB}}(\omega), \quad (7.10)$$

with  $D_{\text{UHB}}(\omega) = D_{\text{LHB}}(-\omega)$ .

At last, we can obtain the Green function via the density of states. We have to choose bath energies and hybridizations in such a way that the single-particle Green function and the hybridization function the self-consistency condition (7.4).

The DDMRG provides the local density of states for the model (7.2)

$$D_\sigma^\eta(\omega_i) = -\frac{1}{\pi} \text{sgn}(\omega_i) \text{Im} G_\sigma(\omega_i) \quad (7.11)$$

at selected frequencies  $\omega_i$  very accurately. Here,  $\eta$  is a finite broadening which must be scaled inversely proportional to the system size [45]. To carry out the iterative procedure, we deconvolve the DDMRG data by inserting the Lorentz transformation

$$D^\eta(\omega_i) = \sum_j \frac{\delta\omega}{\pi} \frac{\eta}{\eta^2 + (\omega_i - \omega_j)^2} D(\omega_j), \quad (7.12)$$

where  $D^\eta(\omega) = D_\uparrow^\eta(\omega) + D_\downarrow^\eta(\omega)$ . Through Eq. (7.11) this deconvolved density of states  $D(\omega)$  determines the imaginary part of the Green function  $G(\omega)$  which is used in the accurate and stable ‘fixed-energy DMFT’ (FE-DMFT) scheme [65], where the  $\epsilon_l$  are kept fixed and the  $V_l$  are determined self-consistently within the cycle.

### 7.1.2 Ground-state properties

Using Kato–Takahashi strong-coupling perturbation theory [67], Kalinowski and co-workers calculated the ground-state energy  $e_0(U)$  ( $= E_0(U)/L$ ) to 11th order in the inverse coupling strength [65, 68, 69]:

$$e_0(U) = -\frac{U}{4} - \frac{1}{2U} - \frac{1}{2U^3} - \frac{19}{8U^5} - \frac{593}{32U^7} - \frac{23877}{128U^9} - \frac{4496245}{2048U^{11}} - \mathcal{O}(U^{-13}). \quad (7.13)$$

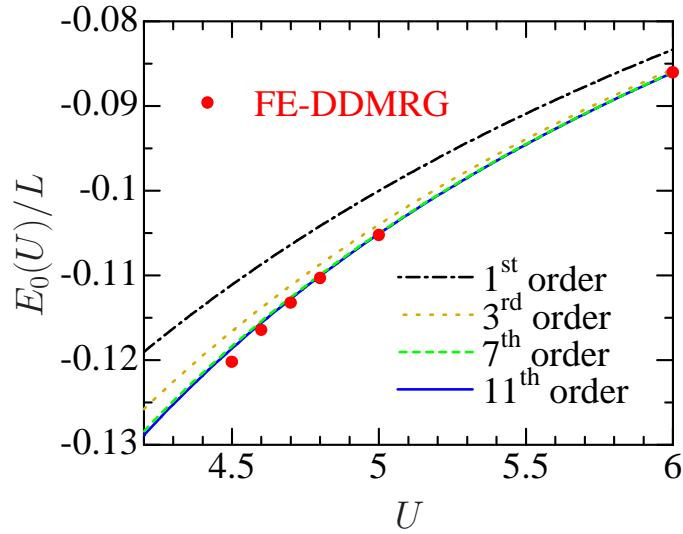


Fig. 7.2: Ground-state energy  $E_0/L$  of the Mott–Hubbard insulator as a function of the interaction strength [66]. FE-DMFT (DDMRG) results for  $U=4.5, 4.6, 4.7, 4.8, 5, 6$  (circles) and perturbation theory (lines) for various orders in  $1/U$ .

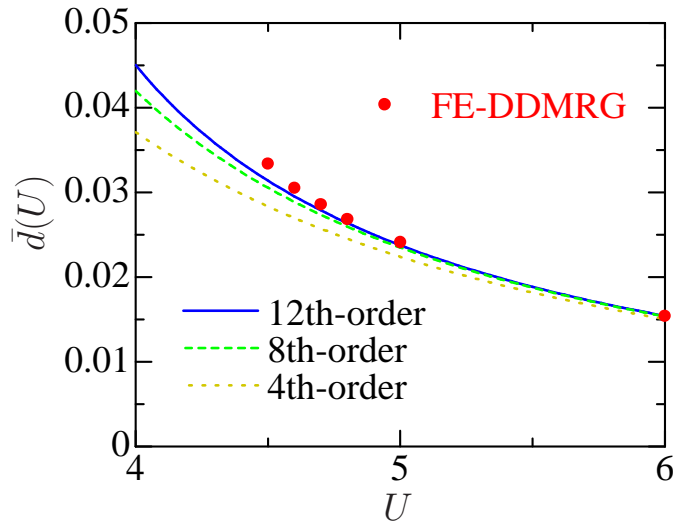


Fig. 7.3: Average double occupancy of the Mott–Hubbard insulator in infinite dimensions as a function of the interaction strength  $U$  [66]. FE-DMFT (DDMRG) results for  $U = 4.5, 4.6, 4.7, 4.8, 5, 6$  (circle) and perturbation theory for various orders in  $1/U$  (lines).

We verified the terms up to order  $U^{-9}$  independently. The average double occupancy is related to a partial derivative of the ground-state energy by

$$d(U) = \frac{1}{4} + \frac{1}{L} \langle \hat{D} \rangle = \frac{1}{4} + \frac{1}{L} \frac{\partial E_0(U)}{\partial U}. \quad (7.14)$$

Therefore, we obtain from Eq. (7.13)

$$d(U) = \frac{1}{2U^2} + \frac{3}{2U^4} + \frac{95}{8U^6} + \frac{4151}{32U^8} + \frac{214893}{128U^{10}} + \frac{49458695}{2048U^{12}} + \mathcal{O}(U^{-14}). \quad (7.15)$$

The ground-state energy per site of the Hubbard model can also be calculated numerically from the self-consistent single-impurity Anderson model. In Fig. 7.2 we show the ground-state energy  $E_0(L)/L$  in the Mott–Hubbard insulator phase for  $4.5 \leq U \leq 6$  in comparison with the strong-coupling perturbation theory (7.13). As we can see, there is a very good agreement between the numerical data and the analytical results. DDMRG data points lie slightly below the best perturbative energy (11th order in  $1/U$ ). As expected, deviations from the perturbative results become larger when  $U$  becomes smaller. N. Bluemer *et al.* show a comparison between the DMFT (QMC) approach [68] and the analytical data, and the agreement is also very good. The differences are small, of the order of  $2 \times 10^{-4}$  or less, for  $U \geq 4.8$ . No comparison with DDMRG data is possible below the coupling strength  $U < 4.8$ , since the Mott insulator solution disappears in the DMFT (QMC) approach.

In Fig. 7.3 we compare FE-DMFT (DDMRG) results for the average double occupancy with perturbation theory (7.15) up to 12th order in  $1/U$ . Again, the agreement is very good but deviations become clearly noticeable for  $U < 5$ . FE-DMFT (DDMRG) and DMFT (QMC) [68] data provide results for the average double occupancy which deviate from each other by less than  $3 \times 10^{-5}$  down to  $U = 4.8$ .

### 7.1.3 Mott–Hubbard transitions

Let us consider the single-particle gap in the Mott–Hubbard insulator. As shown in Ref. [65], from strong-coupling perturbation theory the density of states of the lower Hubbard band is given to second order in  $1/U$  by

$$D_{\text{LHB}}(\omega) = \int_{-2}^2 d\epsilon \rho_0(\epsilon) s(\epsilon, U) \delta\left(\omega + \frac{U}{2} + g(\epsilon, U)\right) + \mathcal{O}(U^{-3}),$$

$$s(\epsilon, U) = 1 - \frac{\epsilon}{U} + \frac{9(\epsilon^2 - 1)}{4U^2}, \quad g(\epsilon, U) = \epsilon - \frac{\epsilon^2 - 3}{2U} + \frac{3\epsilon(2\epsilon^2 - 7)}{8U^2}. \quad (7.16)$$

The zeros of  $D_{\text{LHB}}(\omega)$  provide the single-particle gap

$$\Delta^{\text{PT}2}(U) = U - 4 - \frac{1}{U} - \frac{3}{2U^2}, \quad (7.17)$$

up to second order in  $1/U$ . Using this  $\Delta^{\text{PT}2}(U)$  we can obtain the critical interaction strength  $U_{c,1}^{\text{PT}2} = 4.31$  from  $\Delta^{\text{PT}2}(U_{c,1}^{\text{PT}2}) = 0$ . The calculated single-particle gaps from FE-DDMRG and FE-ED methods are compared with  $\Delta^{\text{PT}2}(U)$  in Fig. 7.4. Here, the estimated value of  $U_c$  from FE-DDMRG is  $U_{c,1}^{\text{DDMRG}} \approx 4.45$  with an error smaller than 0.05.

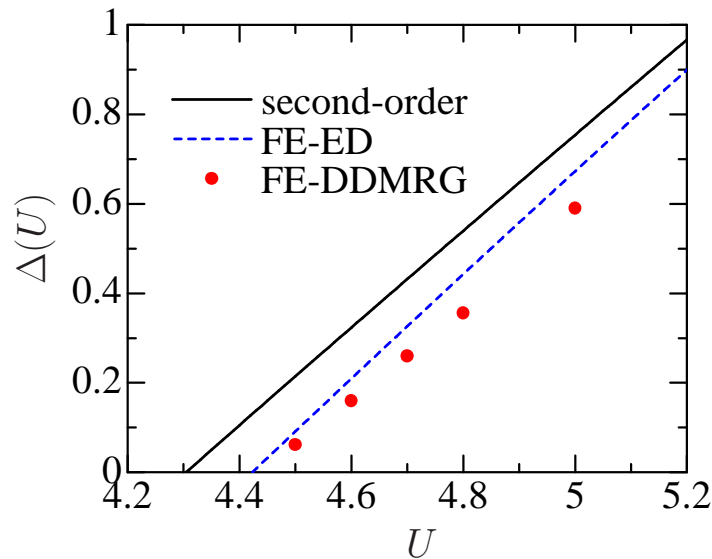


Fig. 7.4: Single-particle gap of the Mott–Hubbard insulator in the limit of infinite dimensions as a function of the interaction strength [66]. FE-DMFT (DDMRG) results (circles), second-order perturbation theory (solid line) and the interpolated result from FE-DMRG (ED) (dashed line).

In contrast to that, several groups found the critical value  $U_{c,1} \approx 4.78$  using the numerical renormalization group (NRG) method within DMFT [70], an analysis of the strong-coupling expansion [68], and the DMRG combined with the Lanczos technique within DMFT (Lanczos-DMRG) [71]. In table 7.1 we summarize the critical interaction strength  $U_c$  obtained by various analytical and numerical methods.

	RDA	FE-DMFT(DDMRG)	QMC	NRG	Lanczos-DMRG
$U_{c,1}$	$4.0 \pm 0.4$	$4.45 \pm 0.05$	4.782	4.78	4.78
$U_{c,2}$	equal to $U_{c,1}$	$6.2 \pm 0.1$	5.84	5.88	$6.0 \pm 0.4$

Table 7.1: Comparison of the calculated critical interaction strength, using the random dispersion approximation (RDA) [72], FE-DMFT (DDMRG) [66], QMC [68], NRG [70] and Lanczos-DMRG [71].

In summary, we have a good agreement in the ground-state energy and average double occupancy between the analytical and numerical results. However, the value for  $U_{c,1}$  from FE-DMFT (DDMRG) results are in conflict with other numerical methods. Therefore, it is important to have an exactly solvable model system which provides more insight into the physics of charges moving via random spin background. Moreover, such a model permits us to judge applicability of series expansions for the ground-state energy  $e_0(U)$  and the gap  $\Delta(U)$ .

## 7.2 Exact results for the Harris–Lange model

The Harris–Lange model is an exactly solvable one-dimensional model which describes the motion of charges in a random spin background. It naturally arises in the perturbative treatment of the Hubbard model around the atomic limit. This expansion was performed for the first time by Harris and Lange [73]. For this reason the resulting effective Hamiltonian to lowest order in  $W/U$  is called the “Harris–Lange model”. In this section we review the Harris–Lange model as our second example of a spin-disordered system.

### 7.2.1 Hamiltonian

We split the Fermi annihilation operator into a part which destroys an electron on a singly occupied site and another part which destroys an electron on a doubly occupied site:

$$\hat{c}_{l,\sigma} = \hat{n}_{l,-\sigma} \hat{c}_{l,\sigma} + (1 - \hat{n}_{l,-\sigma}) \hat{c}_{l,\sigma}. \quad (7.18)$$

The corresponding creation operator can be treated accordingly. We may split the kinetic energy operator into

$$\hat{T} = \hat{T}_{\text{LHB}} + \hat{T}_{\text{UHB}} + \hat{T}^+ + \hat{T}^-, \quad (7.19)$$

where

$$\hat{T}_{\text{LHB}} = -t \sum_{l,\sigma} (1 - \hat{n}_{l,-\sigma}) (\hat{c}_{l,\sigma}^\dagger \hat{c}_{l+1,\sigma} + \hat{c}_{l+1,\sigma}^\dagger \hat{c}_{l,\sigma}) (1 - \hat{n}_{l+1,-\sigma}), \quad (7.20)$$

$$\hat{T}_{\text{UHB}} = -t \sum_{l,\sigma} \hat{n}_{l,-\sigma} (\hat{c}_{l,\sigma}^\dagger \hat{c}_{l+1,\sigma} + \hat{c}_{l+1,\sigma}^\dagger \hat{c}_{l,\sigma}) \hat{n}_{l+1,-\sigma}, \quad (7.21)$$

$$\begin{aligned} \hat{T}^+ &= -t \sum_{l,\sigma} \left[ \hat{n}_{l,-\sigma} \hat{c}_{l,\sigma}^\dagger \hat{c}_{l+1,\sigma} (1 - \hat{n}_{l+1,-\sigma}) + \hat{n}_{l+1,-\sigma} \hat{c}_{l+1,\sigma}^\dagger \hat{c}_{l,\sigma} (1 - \hat{n}_{l,-\sigma}) \right] \\ &= \left( \hat{T}^- \right)^+. \end{aligned} \quad (7.22)$$

The operator  $\hat{T}_{\text{LHB}}$  for the lower Hubbard band describes the hopping of holes. Doubly occupied sites can move in the upper Hubbard band via  $\hat{T}_{\text{UHB}}$ . Their number is *conserved* by both hopping processes. The operator  $\hat{T}^+$  ( $\hat{T}^-$ ) increases (decreases) the number of double occupancies by one.

The basic idea of the approach of Harris and Lange is to apply a canonical transformation which eliminates the operators  $\hat{T}^\pm$  to a given order in  $t/U$ ,

$$\hat{c}_{l,\sigma} = e^{i\hat{S}(\bar{c})} \bar{c}_{l,\sigma} e^{-i\hat{S}(\bar{c})} \quad (7.23)$$

with  $(\hat{S}(\bar{c}))^+ = \hat{S}(\bar{c})$ . Since  $[\hat{D}, \hat{T}^\pm]_- = \pm \hat{T}^\pm$ , the operator to lowest order in  $t/U$  reads

$$\hat{S}(\bar{c}) = \frac{it}{U} \left( \hat{T}^+ - \hat{T}^- \right). \quad (7.24)$$

Neglecting all correction terms to order  $t/U$  and higher, we arrive at the Harris–Lange model

$$\hat{\mathcal{H}}_{\text{HL}} = \hat{T}_{\text{LHB}} + \hat{T}_{\text{UHB}} + U\hat{D}. \quad (7.25)$$

Therefore, the energies obtained from the Harris–Lange model agree with those of the Hubbard model to order  $t(t/U)^{-1}$  and  $t(t/U)^0$ . For all other physical operators which do not contain a factor of  $U/t$  we may replace

$$\hat{c}_{l,\sigma} = \bar{c}_{l,\sigma} \quad (7.26)$$

since the error is only of order  $(t/U)$ , and we do not have to distinguish between the operators  $\hat{c}_{l,\sigma}$  and  $\bar{c}_{l,\sigma}$  to lowest order in  $t/U$ .

The corresponding band structure for the charge excitations is shown in Fig. 7.5.

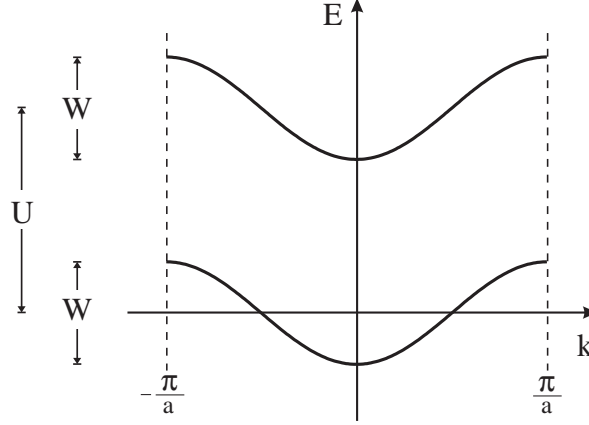


Fig. 7.5: Dispersion relation for charges in the upper and lower Hubbard band of the Harris–Lange model for  $U = 2W$ , from Ref. [74].

### 7.2.2 Optical absorption and optical conductivity in an array of chains

Our presentation follows Ref. [74]. The dielectric function  $\tilde{\epsilon}(\omega)$  and the coefficient for the linear optical absorption  $\tilde{\alpha}(\omega)$  are given by

$$\tilde{\epsilon}(\omega) = 1 + \frac{4\pi i \sigma(\omega)}{\omega}, \quad (7.27)$$

$$\tilde{\alpha}(\omega) = \frac{4\pi \text{Re}[\sigma(\omega)]}{n_b c}, \quad (7.28)$$

where  $n_b$  is the background refractive index, and  $c$  is the speed of light. The real part of the optical conductivity is described in terms of the current-current correlation function  $\chi(\omega)$  by

$$\text{Re}[\sigma(\omega)] = \frac{\text{Im}[\chi(\omega)]}{\omega}, \quad (7.29)$$

$$\chi(\omega) = \frac{\mathcal{N}_\perp}{La} i \int_0^\infty dt e^{i\omega t} \langle [\hat{j}(t), \hat{j}]_- \rangle, \quad (7.30)$$

where  $\mathcal{N}_\perp$  is the number of chains per unit area perpendicular to the chain direction, and  $a$  is the lattice spacing.

We can spectrally decompose the current-current correlation function in terms of exact eigenstates of the system as

$$\chi(\omega) = \frac{\mathcal{N}_\perp}{La} \sum_n |\langle 0|\hat{j}|n\rangle|^2 \left[ \frac{1}{\omega + (E_n - E_0) + i\eta} - \frac{1}{\omega - (E_n - E_0) + i\eta} \right], \quad (7.31)$$

where  $|0\rangle$  is the exact ground state with the energy  $E_0$ ,  $|n\rangle$  are exact excited states with the energies  $E_n$ , and  $|\langle 0|\hat{j}|n\rangle|^2$  are the oscillator strengths for optical transitions between them.  $\eta$  is a phenomenological broadening of the resonances at  $\omega = \pm(E_n - E_0)$ . The spectral decomposition of the real part of the optical conductivity reads

$$\text{Re}[\sigma(\omega)] = \frac{\mathcal{N}_\perp \pi}{La\omega} \sum_n |\langle 0|\hat{j}|n\rangle|^2 [\delta(\omega - (E_n - E_0)) - \delta(\omega + (E_n - E_0))], \quad (7.32)$$

which is positive for all  $\omega$ .

In the following we will concentrate on the dimensionless reduced optical conductivity

$$\sigma_{\text{red}}(\omega > 0) = \frac{\omega \text{Re}[\sigma(\omega > 0)]}{\mathcal{N}_\perp a e^2 W}. \quad (7.33)$$

According to the spectral decomposition of the current-current correlation function (7.31), it is necessary to determine the excitation energies  $E_n - E_0$  and their oscillator strengths  $|\langle 0|\hat{j}|n\rangle|^2$ . The corresponding total momenta of these states are  $P_0$  and  $P_n$ .

### 7.2.3 Optical absorption in the Harris–Lange model

In the Harris–Lange model at half-filling all states with no double occupancy are possible ground states, i.e., the spin background is disordered. Instead of calculating the optical absorption for a specific state  $|0\rangle$ , we investigate the average absorption

$$\overline{\text{Im}[\chi(\omega)]} = \frac{1}{2L} \sum_{|0\rangle} \text{Im}[\chi(\omega)]. \quad (7.34)$$

For the Hubbard model this corresponds to temperatures  $k_B T \gg J = \mathcal{O}(W^2/U)$ , i.e., the ‘hot-spin case’. The spin average in the Harris–Lange model gives rise to the ‘spin-structure factor’

$$g(q) = \frac{3}{5 + 4 \cos(qa)}, \quad (7.35)$$

which enters the real part of the average optical conductivity in the form

$$\text{Re}[\overline{\sigma(\omega > 0)}] = \frac{\mathcal{N}_\perp \pi}{2L^2 a \omega} \sum_{|q|, |k| \leq \pi/a} \{ea\epsilon(k)\}^2 g(q) \delta(\omega - E(k, q)) \quad (7.36)$$

with

$$E(k, q) = U + \epsilon(k + q/2) - \epsilon(k - q/2) = U + 4t \sin(ka) \sin(qa/2). \quad (7.37)$$

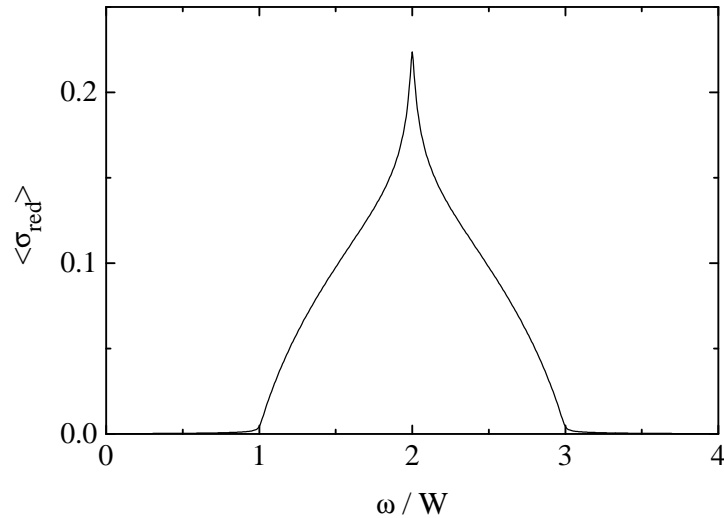


Fig. 7.6: Reduced average optical conductivity  $\overline{\sigma_{\text{red}}(\omega > 0)}$  for the Harris–Lange model for  $U = 2W$  [74]. A broadening of  $\eta = 0.01W$  has been included.

The reduced optical conductivity becomes

$$\overline{\sigma_{\text{red}}(\omega > 0)} = \frac{1}{4\pi} \int_{u'}^1 \frac{dx}{x^2} \sqrt{\frac{x^2 - u'^2}{1 - x^2}} \frac{3}{9 - 8x^2} \quad (7.38)$$

with  $u' = |\omega - U|/W \leq 1$ . The integrand displays a  $1/x$  singularity for  $u' \rightarrow 0$ . The parallel Hubbard bands seen in Fig. 7.5 give rise to a logarithmic divergence,  $\sigma(\omega \rightarrow U) \sim |\ln(\omega - U)|$ , because their large joint density of states for  $\omega = U$  survives even in the presence of a spinon bath which provides any momentum to the charge sector. The overall behavior of the optical absorption is shown in Fig. 7.6.

The same absorption curve was obtained by Lyo *et al.* [75] for a half-filled Hubbard model with a random spin background. In fact, the Harris–Lange model treats the strong-coupling limit of the Hubbard model,  $U - W \gg k_{\text{B}}T \gg J$ , where all terms of  $\mathcal{O}(U^{-1})$  are omitted. Naturally, it is interesting to go one step further and treat the one-dimensional Hubbard model for finite  $J$ . This requires the solution of the Thermodynamic Bethe Ansatz equations for the one-dimensional Hubbard model for the temperature region  $U - W \gg k_{\text{B}}T \gg J$ , to which we turn now.

## 8 Thermodynamic Bethe ansatz equations

In 1967 Yang used the Bethe ansatz to solve the one-dimensional electron-gas problem with a  $\delta$ -function interaction. One year later Lieb and Wu generalized Yang's solution to the one-dimensional Hubbard model [76]. They obtained the celebrated Lieb–Wu equations, which yield the exact ground-state energy of the model. Takahashi thereafter obtained the finite-temperature Bethe-ansatz equations and the *Thermodynamic Bethe Ansatz* (TBA) equations for the model based on Lieb and Wu's solution [77]. Furthermore, Ha solved the TBA equations in a strong-coupling expansion series form [78]. Based on Ha's result we investigate the properties of charges in a random spin background in the one-dimensional Hubbard model.

In first three sections, we review the basic concept of the Lieb–Wu, Takahashi and TBA equations. In Sec. 8.4, we work out Ha's result to the required lowest order. The presentation in this chapter closely follows Refs. [5, 79, 80].

### 8.1 Lieb–Wu equations for the one-dimensional Hubbard model

From now on we work with the following form of the Hubbard Hamiltonian

$$\begin{aligned} \hat{\mathcal{H}} = & -t \sum_{j=1}^L \sum_{\sigma=\uparrow,\downarrow} (\hat{c}_{j,\sigma}^\dagger \hat{c}_{j+1,\sigma} + \hat{c}_{j+1,\sigma}^\dagger \hat{c}_{j,\sigma}) + U \sum_{j=1}^L \hat{n}_{j\uparrow} \hat{n}_{j\downarrow} \\ & - \mu \sum_{j=1}^L (\hat{n}_{j\uparrow} + \hat{n}_{j\downarrow}) - B \sum_{j=1}^L (\hat{n}_{j\uparrow} - \hat{n}_{j\downarrow}). \end{aligned} \quad (8.1)$$

In what follows we define  $u = U/4t$  and set  $t = 1$ .

Lieb and Wu obtained the following Bethe ansatz equations for  $N$  electrons,  $M$  down spins on a  $L$  site system:

$$\exp(ik_j L) = \prod_{\beta=1}^M \frac{\Lambda_\beta - \sin k_j - iu}{\Lambda_\beta - \sin k_j + iu}, \quad j = 1, \dots, N, \quad (8.2)$$

$$\prod_{j=1}^N \frac{\Lambda_\alpha - \sin k_j - iu}{\Lambda_\alpha - \sin k_j + iu} = \prod_{\substack{\beta=1 \\ \beta \neq \alpha}}^M \frac{\Lambda_\alpha - \Lambda_\beta - 2iu}{\Lambda_\alpha - \Lambda_\beta + 2iu}, \quad \alpha = 1, \dots, M. \quad (8.3)$$

Here,  $\Lambda_\alpha$  is the spin rapidity introduced for each down spin. The eigenenergy and momentum of the state are

$$E = - \sum_{j=1}^N 2 \cos k_j - \mu N - B(N - 2M), \quad P = \sum_{j=1}^N k_j. \quad (8.4)$$

The ground state is described by real  $k$ 's and  $\Lambda$ 's. On the other hand, an excited state is given by the complex rapidities with the so-called *string hypothesis* which is discussed in the next section.

Let us take the logarithm of Eq. (8.2) and (8.3) using Eq. (A.17) we obtain

$$Lk_j = 2\pi I_j + 2 \sum_{\beta=1}^M \arctan \left[ \frac{\Lambda_\beta - \sin k_j}{u} \right], \quad (8.5)$$

$$\sum_{j=1}^N 2 \arctan \left[ \frac{\Lambda_\alpha - \sin k_j}{u} \right] = 2\pi J_\alpha + \sum_{\beta=1}^M 2 \arctan \left[ \frac{\Lambda_\alpha - \Lambda_\beta}{2u} \right]. \quad (8.6)$$

Here the  $I_j$ s are integers (half-odd integers) for even (odd)  $M$  and the  $J_\alpha$ s are integers (half-odd integers) for odd (even)  $N - M$ . From these equations and (8.4) we obtain the total momentum:

$$P = \frac{2\pi}{L} \left( \sum_{j=1}^N I_j + \sum_{\beta=1}^M J_\beta \right). \quad (8.7)$$

For the ground state  $I_j$  and  $J_\alpha$  are successive integers or half-integers centered around the origin. For the lowest energy state at even  $N$  and odd  $M$  they are

$$I_j = \frac{N-1}{2}, \frac{N-3}{2}, \dots, -\frac{N-1}{2}, \quad J_\alpha = \frac{M-1}{2}, \frac{M-3}{2}, \dots, -\frac{M-1}{2}. \quad (8.8)$$

Now we take the limit  $L \rightarrow \infty$  and consider  $N/L$  and  $M/N$  as constants. We define the distribution functions of  $ks$  and  $\Lambda$ s as  $\rho(k)$  and  $\sigma(\Lambda)$ . From Eq. (8.5) and (8.6) we obtain

$$k = 2\pi f(k) - \int_{-A}^A 2 \arctan \left[ \frac{\sin k - \Lambda}{u} \right] \sigma(\Lambda) d\Lambda, \quad (8.9)$$

$$\int_{-Q}^Q 2 \arctan \left[ \frac{\Lambda - \sin k}{u} \right] \rho(k) dk = 2\pi g(\Lambda) + \int_{-A}^A 2 \arctan \left[ \frac{\Lambda - \Lambda'}{2u} \right] \sigma(\Lambda') d\Lambda', \quad (8.10)$$

where  $f_j(k) = I_j/L$  and  $g_\alpha(\Lambda) = J_\alpha/L$ . We know that  $k_j$  takes values in the interval  $[-\pi, \pi]$  since  $k$  and  $k + 2\pi n$  give the same wave function. If we consider  $I_j$  as a function of  $k$ ,  $f_j(k + dk) - f_j(k)$  counts the number of  $k$  values from  $k$  to  $k + dk$ . Therefore we have  $f'(k) = \rho(k)$  and  $g'(\Lambda) = \sigma(\Lambda)$ .  $+Q$  ( $-Q$ ) is the upper (lower) bound of the distribution of  $ks$ , and  $\pm A$  are the bounds on the  $\Lambda$ s. Differentiating with respect to  $k$  and  $\Lambda$  we obtain

$$\rho(k) = \frac{1}{2\pi} + \cos k \int_{-A}^A a_1(\sin k - \Lambda) \sigma(\Lambda) d\Lambda, \quad (8.11)$$

$$\sigma(\Lambda) = \int_{-Q}^Q a_1(\Lambda - \sin k) \rho(k) dk - \int_{-A}^A a_2(\Lambda - \Lambda') \sigma(\Lambda') d\Lambda' \quad (8.12)$$

where

$$a_n(x) \equiv \frac{1}{2\pi} \frac{2nu}{(nu)^2 + x^2}. \quad (8.13)$$

$Q$  and  $A$  are determined by the conditions

$$\int_{-Q}^Q \rho(k) dk = N/L = n = n_{\uparrow} + n_{\downarrow}, \quad (8.14)$$

$$\int_{-A}^A \sigma(\Lambda) d\Lambda = M/L = n_{\downarrow}. \quad (8.15)$$

From Eq. (8.4) we obtain the energy per site

$$e = \int_{-Q}^Q (-2 \cos k - \mu - B) \rho(k) dk + 2B \int_{-A}^A \sigma(\Lambda) d\Lambda. \quad (8.16)$$

Substituting (8.11) into (8.14) and using Eq. (A.1) of the appendix we can easily see that  $Q = \pi$  implies that the band is half filled:

$$\frac{N}{L} = \int_{-\pi}^{\pi} dk \rho(k) = 1. \quad (8.17)$$

It is also useful to consider the case  $A = \infty$ . From (8.11), (8.12), (8.14) and (8.15) we obtain

$$n_{\downarrow} = \int_{-\infty}^{\infty} d\Lambda \sigma(\Lambda) = \frac{1}{2} \int_{-Q}^Q dk \rho(k) = \frac{N}{2L} = \frac{n}{2}, \quad (8.18)$$

i.e., the magnetization of the ground state is zero. In addition we obtain from Eq. (8.12)

$$\begin{aligned} \tilde{\sigma}(\omega) &= \int_{-\infty}^{\infty} e^{i\omega\Lambda} \sigma(\Lambda) \\ &= \int_{-Q}^Q dk \rho(k) \exp[-u|\omega| + i\omega \sin k] - \int_{-\infty}^{\infty} d\Lambda' e^{i\omega\Lambda'} \sigma(\Lambda') e^{-2u|\omega|}. \end{aligned} \quad (8.19)$$

Collecting terms and Fourier transforming back we arrive at

$$\sigma(\Lambda) = \int_{-Q}^Q dk \rho(k) \int_{-\infty}^{\infty} \frac{d\omega}{2\pi} \frac{\exp[-i\omega(\Lambda - \sin k)]}{2 \cosh(u\omega)} = \int_{-Q}^Q dk s(\Lambda - \sin k) \rho(k). \quad (8.20)$$

### 8.1.1 Ground-state energy at half band-filling

At  $Q = \pi$ ,  $A = \infty$  we can solve the coupled integral equations (8.11) and (8.12) analytically. From Eq. (8.20) and (A.1) we have

$$\sigma_0(\Lambda) = \int_{-\pi}^{\pi} \frac{dk}{2\pi} s(\Lambda - \sin k) = \int_{-\infty}^{\infty} \frac{d\omega}{2\pi} \frac{J_0(\omega) e^{-i\omega\Lambda}}{2 \cosh(u\omega)}. \quad (8.21)$$

Substituting this into Eq. (8.11),  $\rho(k)$  can be recast as follows:

$$\begin{aligned} \rho_0(k) &= \frac{1}{2\pi} + \cos k \int_{-\pi}^{\pi} \frac{dk'}{2\pi} R(\sin k - \sin k') \\ &= \frac{1}{2\pi} + \cos k \int_{-\infty}^{\infty} \frac{d\omega}{2\pi} \frac{J_0(\omega) \cos(\omega \sin k)}{1 + \exp(2u|\omega|)}. \end{aligned} \quad (8.22)$$

Substituting these into (8.16) we finally obtain the ground-state energy per site for the half-filled Hubbard chain

$$e_0 = -\mu - 4 \int_0^{\infty} \frac{J_0(\omega) J_1(\omega)}{1 + \exp(2u\omega)}. \quad (8.23)$$

### 8.1.2 Mott transition at zero temperature

Next we investigate whether or not there is a gap for charge excitations, in order to gain some insight into the conducting properties in the half-filled Hubbard model. In general, we have two kind of chemical potentials, namely one ( $\mu_+$ ) necessary to add one extra electron into the half-filled ground state and the other ( $\mu_-$ ) necessary to remove one electron:

$$\mu_{\pm} = \pm[E(L \pm 1, u) - E(L, u)], \quad (8.24)$$

where  $E(N, u)$  is the ground-state energy for the Hubbard model with  $N$  electrons. Due to electron-hole symmetry we have

$$E(N, u) = -(L - N)U + E(2L - N, u). \quad (8.25)$$

Then, the charge gap  $\Delta$  is given by

$$\Delta = \mu_+ - \mu_- = U - 2\mu_-. \quad (8.26)$$

Therefore, we need only the chemical potential  $\mu_-$  to calculate the charge gap.

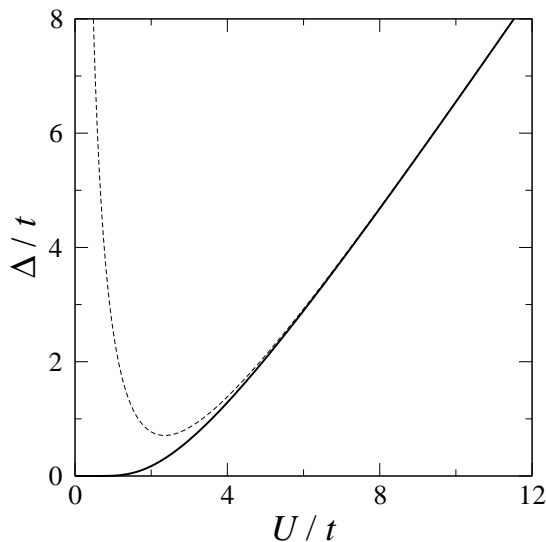


Fig. 8.1: Mott-Hubbard gap  $\Delta$  for the one-dimensional Hubbard model at half filling as a function of the interaction strength  $U/t$ . The dashed line is the result of the large- $U$  expansion.

Now we remove one electron from the half-filled chain ( $N = L - 1$ ). Hence, we have to put one hole into the successive distribution of the quantum number for the charge excitations  $I_j$ . We define this hole to be at  $I_h$ . It gives rise to the shift of  $\delta$ -function form in  $\rho(k)$  which distributes successively in the region  $[-\pi, \pi]$ . Therefore, in the r.h.s of Eq. (8.11) the shift  $1/2\pi \rightarrow 1/2\pi - (1/L)\delta(k - k_h)$  shows this type of charge excitations. As we can see here, the shift due to the creation of one hole is proportional to  $1/L$ .  $\sigma_1(\Lambda)$  is the corresponding change in  $\sigma(\Lambda)$  and satisfies

$$\sigma_1(\Lambda) = -s(\Lambda - \sin k_h). \quad (8.27)$$

Substituting this into (8.11) we obtain the change in  $\rho(k)$ :

$$\rho_1(k) = -\delta(k - k_h) - \cos k R(\sin k - \sin k_h). \quad (8.28)$$

This equality is obtained via Eq. (A.10). Integrating this equation we can check that the number of particles is  $N = L - 1$ . Substituting  $\rho_1(k)$  into (8.16) we obtain the excitation energy for charge excitations as

$$e_1(k_h) = 2 \cos k_h + \mu + 2 \int_{-\pi}^{\pi} \cos^2 k R(\sin k - \sin k_h) dk. \quad (8.29)$$

The minimum value of this excitation is given by  $k_h = \pm\pi$ . Because the spin excitation has no gap, the chemical potential  $\mu_-$  is derived from the condition  $e_1(\pm\pi) = 0$ . Finally, we obtain the charge gap  $\Delta$  substituting this  $\mu_-$  into (8.26)

$$\begin{aligned} \Delta &= U - 4 \left[ 1 - \int_{-\pi}^{\pi} \cos^2 k R(\sin k) dk \right] \\ &= U - 4 \left[ 1 - \int_0^{\infty} \frac{d\omega}{\omega} \frac{J_1(\omega) e^{-U\omega/4}}{\cosh(u\omega)} \right]. \end{aligned} \quad (8.30)$$

In the limiting cases of weak and strong interactions the gap  $\Delta$  becomes [81, 82]

$$\Delta(U) = \begin{cases} (8/\pi)\sqrt{U} \exp(-2\pi/U) & \text{for } U \lesssim W/2 = 2 \\ U - 4 + 8 \ln(2)/U & \text{for } U \gtrsim W = 4 \end{cases}. \quad (8.31)$$

The gap  $\Delta$  is shown in Fig. 8.1 as a function of  $U/t$ . As we can see from the figure and (8.31),  $\Delta$  is always positive at  $U > 0$ , i.e., the half-filled Hubbard chain is always an insulator with critical interaction strength  $U_c = 0^+$ .

Eq. (8.31) and Fig. 8.1 also show that the gap is exponentially small for  $U \lesssim W/2$ , which is similar to the gap for the superconductivity in BCS theory. Actually, in the weak coupling region the insulating phase is formed by creating electron-hole pairs within a wide region around the Fermi surface. On the other hand, when the interaction becomes larger, the gap increases proportional to  $U$ . Since  $\Delta \sim U$  corresponds to the energy with two electrons on one site, the electrons are localized on individual lattice sites.

The Mott insulating phase in the Hubbard model appears to cross over from a ‘BCS-type instability’ to ‘electron localization’. Indeed, the perfect nesting instability for small interactions is a consequence of the umklapp scattering which is a relevant perturbations at half band-filling, see Chap. 2. If this scattering processes were suppressed, we would see  $U_c = \mathcal{O}(W)$  as indicated by the large- $U$  behavior. We shall confirm this conjecture in Sec. 9.2.1.

## 8.2 Takahashi equations

As seen in the last section, eigenstates of the Hubbard Hamiltonian are described by the solutions of the Lieb–Wu equations (8.2) and (8.3). In 1972, Takahashi introduced the so-called *string hypothesis* to derive the integral equations for the one-dimensional Hubbard model at finite temperature starting from the Lieb–Wu equations [77]. In this section we discuss the string hypothesis and give a short sketch of the *Takahashi equations*.

### 8.2.1 String hypothesis

At first we consider a special case, namely a state with one spin-up and one spin-down electron ( $N = 2$ ,  $M = 1$ ). We allow the spectral parameters  $k$  to be complex, namely  $k_{\pm} = q \pm i\xi$ , where  $q$ ,  $\xi$  are real and  $\xi > 0$ . The Lieb–Wu equations are

$$\exp(ik_-L) = \frac{\Lambda' - \sin(k_-) - iu}{\Lambda' - \sin(k_-) + iu}, \quad (8.32)$$

$$\exp(ik_+L) = \frac{\Lambda' - \sin(k_+) - iu}{\Lambda' - \sin(k_+) + iu}, \quad (8.33)$$

$$1 = \frac{\Lambda' - \sin(k_-) - iu}{\Lambda' - \sin(k_-) + iu} \frac{\Lambda' - \sin(k_+) - iu}{\Lambda' - \sin(k_+) + iu}. \quad (8.34)$$

Since  $\xi > 0$ , the l.h.s. of Eq. (8.32) is exponentially large for large  $L$ . To fulfill Eq. (8.32) the r.h.s. must be exponentially close to a pole,

$$\Lambda' = \sin(k_-) - iu + \mathcal{O}(\exp(-\xi L)). \quad (8.35)$$

This indicates that the second factor on the r.h.s of (8.34) is exponentially small,

$$\sin(k_+) = \Lambda' - iu + \mathcal{O}(\exp(-\xi L)). \quad (8.36)$$

Neglecting the exponential term, we find a  $k$ - $\Lambda$  string solution (see Appendix A.6):

$$\begin{aligned} k_- &= \pi - \arcsin(\Lambda' + iu), \\ k_+ &= \pi - \arcsin(\Lambda' - iu), \end{aligned} \quad (8.37)$$

within the accuracy of  $\mathcal{O}(\exp(-\delta L))$ , where  $\delta$  is some positive number. Here  $\Lambda'$  is real and the branch of  $\arcsin(x)$  is fixed as  $-\pi/2 \leq \text{Re}[\arcsin(x)] \leq \pi/2$ . The corresponding energy of this two-electron state is given by

$$E_{2\text{el}} = -2(\cos k_- + \cos k_+) = 4\text{Re}\sqrt{1 - (\Lambda' - iu)^2}. \quad (8.38)$$

This two-electron case can be generalized straightforwardly. We find that  $2m$   $k$ s can combine with  $m$   $\Lambda$ s to form a  $k$ - $\Lambda$  string of length  $2m$ :

$$\begin{aligned} k_{\alpha}^1 &= \pi - \arcsin(\Lambda_{\alpha}^{\prime m} + miu), \\ k_{\alpha}^2 &= \arcsin(\Lambda_{\alpha}^{\prime m} + (m-2)iu), \\ k_{\alpha}^3 &= \pi - k_{\alpha}^2, \\ &\vdots \\ k_{\alpha}^{2m-2} &= \arcsin(\Lambda_{\alpha}^{\prime m} - (m-2)iu), \\ k_{\alpha}^{2m-1} &= \pi - k_{\alpha}^{2m-2}, \\ k_{\alpha}^{2m} &= \pi - \arcsin(\Lambda_{\alpha}^{\prime} - miu), \end{aligned} \quad (8.39)$$

and

$$\Lambda_{\alpha}^{\prime m, j} = \Lambda_{\alpha}^{\prime m} + (m - 2j + 1)iu + \mathcal{O}(\exp(-\delta L)), \quad j = 1, \dots, m, \quad (8.40)$$

Here,  $\alpha$  distinguishes the strings of the same length  $m$ ,  $j$  counts the  $\lambda$ s involved in a given string, and  $\Lambda_\alpha^m$  is the real center of the  $\alpha$ th  $k$ - $\Lambda$  string. The corresponding energy of this excitation is

$$E_{k-\Lambda} = -2 \sum_{j=1}^{2m} \cos k_\alpha^j = 4 \operatorname{Re} \sqrt{1 - (\Lambda_\alpha^m - imu)^2}. \quad (8.41)$$

In addition, we also have ‘ $\Lambda$  strings’ involving only  $\Lambda$ s which are denoted by

$$\Lambda_\alpha^{m,j} = \Lambda_\alpha^m + (m - 2j + 1)iu + \mathcal{O}(\exp(-\delta L)), \quad j = 1, \dots, m. \quad (8.42)$$

Here,  $\alpha$  distinguishes the strings of the same length  $m$ ,  $j$  counts the  $\lambda$ s involved in the  $\alpha$ th  $\Lambda$  string.  $\Lambda_\alpha^m$  is the real center of the  $\Lambda$  string.

Almost all strings for  $L \gg 1$  and  $N \gg 1$  are close to ideal, i.e., the imaginary part of the  $k$ s and  $\lambda$ s are almost equally spaced. The string hypothesis assumes that almost all solutions of the Lieb–Wu equations are approximately given by Eqs. (8.39), (8.40) and (8.42) within the accuracy of  $\mathcal{O}(\exp(-\delta L))$ , where  $\delta$  is some real and positive number and depends only on the string under consideration.

### 8.2.2 Setup of the Takahashi equations

Let us solve the Lieb–Wu equations (8.2) and (8.3). All regular solutions  $k_j$ ,  $\lambda_l$  of the Lieb–Wu equations are described by the *string hypothesis* [77]:

1. A single real momentum  $k_j$
2.  $m$   $\Lambda$ s correspond to a  $\Lambda$  string (8.42). This includes the case of a real single  $\Lambda_\alpha$ .
3.  $2m$   $k$ s and  $m$   $\Lambda$ s correspond to a  $k$ - $\Lambda$  string (8.39) and (8.40).

These states form a complete set of  $4^L$  eigenstates [83]. Within the framework of the string hypothesis, a solution contains  $\mathcal{M}_e$  single  $k_j$ s,  $M_n$  ‘ $\Lambda$  strings’ and  $M'_n$  ‘ $k$ - $\Lambda$  strings’ of length  $n$  ( $n = 1, 2, \dots$ ).  $\mathcal{M}_e$ ,  $M_n$  and  $M'_n$  are called *occupation numbers* of the string configuration under consideration and satisfy the sum rules

$$M = \sum_{n=1}^{\infty} n(M_n + M'_n), \quad (8.43)$$

$$N = \mathcal{M}_e + \sum_{n=1}^{\infty} 2nM'_n. \quad (8.44)$$

We apply this prescription to the Lieb–Wu equations (8.2) and (8.3) and take the logarithm of the resulting equations. In this way we obtain the so-called *Takahashi equations*, which involve only the real centers of the strings. For even  $L$  we have

$$k_j L = 2\pi I_j - \sum_{n=1}^{\infty} \sum_{\alpha=1}^{M_n} \theta \left( \frac{\sin k_j - \Lambda_\alpha^n}{nu} \right) - \sum_{n=1}^{\infty} \sum_{\alpha=1}^{M'_n} \theta \left( \frac{\sin k_j - \Lambda_\alpha'^n}{nu} \right), \quad (8.45)$$

$$\sum_{j=1}^{N-2M'} \theta \left( \frac{\Lambda_\alpha^n - \sin k_j}{nu} \right) = 2\pi J_\alpha^n + \sum_{m=1}^{\infty} \sum_{\beta=1}^{M_m} \Theta_{nm} \left( \frac{\Lambda_\alpha^n - \Lambda_\beta^m}{u} \right), \quad (8.46)$$

$$2L \operatorname{Re}[\arcsin(\Lambda_\alpha'^n + inu)] = 2\pi J_\alpha'^n + \sum_{j=1}^{N-2M'} \theta \left( \frac{\Lambda_\alpha'^n - \sin k_j}{nu} \right) + \sum_{m=1}^{\infty} \sum_{\beta=1}^{M'_m} \Theta_{nm} \left( \frac{\Lambda_\alpha'^n - \Lambda_\beta'^m}{u} \right), \quad (8.47)$$

$$(8.48)$$

where  $\theta(x) = 2 \arctan(x)$ , and

$$\Theta_{nm}(x) = \begin{cases} \theta \left( \frac{x}{|n-m|} \right) + 2\theta \left( \frac{x}{|n-m|+2} \right) + \cdots + 2\theta \left( \frac{x}{n+m-2} \right) + \theta \left( \frac{x}{n+m} \right), & \text{if } n \neq m \\ 2\theta \left( \frac{x}{2} \right) + 2\theta \left( \frac{x}{4} \right) + \cdots + 2\theta \left( \frac{x}{2n-2} \right) + \theta \left( \frac{x}{2n} \right), & \text{if } n = m. \end{cases} \quad (8.49)$$

Taking the logarithm, we obtain integer or half-odd integer numbers  $I_j$ ,  $J_\alpha^n$  and  $J_\alpha'^n$  again:

$$I_j \quad \text{is} \quad \begin{cases} \text{integer} & \text{if } \sum (M_m + M'_m) \text{ is even} \\ \text{half-odd integer} & \text{if } \sum (M_m + M'_m) \text{ is odd,} \end{cases} \quad (8.50)$$

$$J_\alpha^n \quad \text{is} \quad \begin{cases} \text{integer} & \text{if } N - M_n \text{ is odd} \\ \text{half-odd integer} & \text{if } N - M_n \text{ is even,} \end{cases} \quad (8.51)$$

$$J_\alpha'^n \quad \text{is} \quad \begin{cases} \text{integer} & \text{if } L - N + M'_n \text{ is odd} \\ \text{half-odd integer} & \text{if } L - N + M'_n \text{ is even,} \end{cases} \quad (8.52)$$

$M'$  is the total number of  $\Lambda$ s involved in the  $k$ - $\Lambda$  strings

$$M' = \sum_{n=1}^{\infty} n M'_n. \quad (8.53)$$

The quantum numbers  $I_j$ ,  $J_\alpha^n$  and  $J_\alpha'^n$  are restricted in the following ranges:

$$-\frac{L}{2} < I_j \leq \frac{L}{2}, \quad (8.54)$$

$$|J_\alpha^n| \leq \frac{1}{2} \left( N - 2M' - \sum_{m=1}^{\infty} \gamma_{nm} M_m - 1 \right), \quad (8.55)$$

$$|J_\alpha'^n| \leq \frac{1}{2} \left( L - N + 2M' - \sum_{m=1}^{\infty} \gamma_{nm} M'_m - 1 \right), \quad (8.56)$$

where  $\gamma_{mn} = 2\min(m, n) - \delta_{mn}$ . The eigenenergy and total momentum of the state are given by

$$E = -2 \sum_{j=1}^{N-2M'} \cos k_j + \sum_{n=1}^{\infty} \sum_{\alpha=1}^{M'_n} 4\operatorname{Re} \sqrt{1 - (\Lambda_\alpha'^n - inu)^2}, \quad (8.57)$$

$$\begin{aligned}
P &= \frac{2\pi}{L} \left( \sum_{j=1}^{N-2M'} I_j - \sum_{n=1}^{\infty} \sum_{\alpha=1}^{M'_n} J'_\alpha{}^n - \sum_{n=1}^{\infty} \sum_{\alpha=1}^{M_n} J_\alpha{}^n \right) + \pi \sum_{n=1}^{\infty} \sum_{\alpha=1}^{M'_n} (n+1) \\
&= \sum_{j=1}^{N-2M'} k_j - \sum_{n=1}^{\infty} \sum_{\alpha=1}^{M'_n} (2\text{Re}[\arcsin(\Lambda_\alpha'^n - inu)] - (n+1)\pi). \tag{8.58}
\end{aligned}$$

### 8.3 Thermodynamic Bethe Ansatz (TBA) equations

In this section we derive the TBA equations from the Takahashi equations in the last section. There are three steps to the derivation.

**Step 1:** In order to turn the Takahashi equations (8.45)-(8.47) into a system of coupled integral equations for root densities of particles and holes, we describe a general eigenstate of the Hamiltonian in the thermodynamic limit:

$$L \rightarrow \infty, \quad N_\sigma \rightarrow \infty, \quad n_\sigma = N_\sigma/L = \text{fixed}, \quad \sigma = \uparrow, \downarrow. \tag{8.59}$$

**Step 2:** We describe the entropy and the Gibbs free energy in terms of the root distribution functions.

**Step 3:** We minimize the Gibbs free energy with respect to the root densities and get a set of coupled, nonlinear integral equations.

**Step 1** In the framework of the string hypothesis there is a one-to-one correspondence between sets of the quantum numbers and sets of spectral parameters, i.e.,

$$\{I_j, J_\alpha^n, J_\beta'^m\} \longleftrightarrow \{k_j, \Lambda_\alpha^n, \Lambda_\beta'^m\}. \tag{8.60}$$

Each set  $\{I_j, J_\alpha^n, J_\beta'^m\}$  uniquely identifies a solution  $\{k_j, \Lambda_\alpha^n, \Lambda_\beta'^m\}$  of the Takahashi equations and thus an eigenfunction of the Hamiltonian. The other important property of the Takahashi equations is that as we approach the thermodynamic limit  $L \rightarrow \infty$  and fix  $N/L$  and  $M/L$ , the roots of (8.45)-(8.47) become dense

$$k_{j+1} - k_j = \mathcal{O}(L^{-1}), \quad \Lambda_{\alpha+1}^n - \Lambda_\alpha^n = \mathcal{O}(L^{-1}), \quad \Lambda_{\alpha+1}'^n - \Lambda_\alpha'^n = \mathcal{O}(L^{-1}). \tag{8.61}$$

Now we define the so-called *counting functions* as follows

$$y(k_j) = \frac{2\pi I_j}{L}, \quad z'_n(\Lambda_\alpha^n) = \frac{2\pi J_\alpha'^n}{L}, \quad z_n(\Lambda_\alpha^n) = \frac{2\pi J_\alpha^n}{L}. \tag{8.62}$$

Then we have

$$Ly(k) = kL + \sum_{n=1}^{\infty} \sum_{\alpha=1}^{M_n} \theta\left(\frac{\sin k - \Lambda_\alpha^n}{nu}\right) + \sum_{n=1}^{\infty} \sum_{\alpha=1}^{M'_n} \theta\left(\frac{\sin k - \Lambda_\alpha'^n}{nu}\right), \tag{8.63}$$

$$Lz_n(\Lambda) = \sum_{j=1}^{N-2M'} \theta\left(\frac{\Lambda - \sin k_j}{nu}\right) - \sum_{m=1}^{\infty} \sum_{\beta=1}^{M_m} \Theta_{nm}\left(\frac{\Lambda - \Lambda_\beta^m}{u}\right), \tag{8.64}$$

and

$$Lz'_n(\Lambda') = L[\arcsin(\Lambda' + inu) - \arcsin(\Lambda' - inu)] - \sum_{j=1}^{N-2M'} \theta\left(\frac{\Lambda' - \sin k_j}{nu}\right) - \sum_{m=1}^{\infty} \sum_{\beta=1}^{M'_m} \Theta_{nm}\left(\frac{\Lambda' - \Lambda'_\beta}{u}\right). \quad (8.65)$$

We note that the counting functions are monotonically increasing functions of their arguments.

Next we define the *root densities*. By definition, the counting functions enumerate the roots, e.g.,

$$L[y(k_j) - y(k_n)] = 2\pi(I_j - I_n). \quad (8.66)$$

For a given solution of the Takahashi equations some of the numbers between  $I_j$  and  $I_n$  will be occupied with a corresponding root  $k$ . We define this  $k$ -values in terms of a root density  $\rho^p(k)$  for *particles* and  $\rho^h(k)$  for *holes*. Then for  $L \gg 1$  we have by definition

$$\begin{aligned} L\rho^p(k)dk &= \text{number of particles in } dk, \\ L\rho^h(k)dk &= \text{number of holes in } dk. \end{aligned} \quad (8.67)$$

Combining Eqs. (8.66) and (8.67) in the thermodynamic limit we obtain

$$2\pi[\rho^p(k) + \rho^h(k)] = \frac{dy(k)}{dk}. \quad (8.68)$$

We obtain similar equations for the other types of roots in (8.45)-(8.47)

$$2\pi[\sigma_n^p(\Lambda) + \sigma_n^h(\Lambda)] = \frac{dz_n(\Lambda)}{d\Lambda}, \quad 2\pi[\sigma_n'^p(\Lambda) + \sigma_n'^h(\Lambda)] = \frac{dz_n'(\Lambda)}{d\Lambda}. \quad (8.69)$$

Now we can turn the Takahashi equations into coupled integral equations with counting functions and root densities

$$y(k) = k + \sum_{n=1}^{\infty} \int_{-\infty}^{\infty} d\Lambda \theta\left(\frac{\sin k - \Lambda}{nu}\right) [\sigma_n'^p(\Lambda) + \sigma_n^p(\Lambda)], \quad (8.70)$$

$$z_n(\Lambda) = \int_{-\pi}^{\pi} dk \theta\left(\frac{\Lambda - \sin k}{nu}\right) \rho^p(k) - \sum_{m=1}^{\infty} \int_{-\infty}^{\infty} d\Lambda' \Theta_{nm}\left(\frac{\Lambda - \Lambda'}{u}\right) \sigma_m^p(\Lambda'), \quad (8.71)$$

$$\begin{aligned} z_n'(\Lambda) &= \arcsin(\Lambda + inu) + \arcsin(\Lambda - inu) \\ &\quad - \int_{-\pi}^{\pi} dk \theta\left(\frac{\Lambda - \sin k}{nu}\right) \rho^p(k) - \sum_{m=1}^{\infty} \int_{-\infty}^{\infty} d\Lambda' \Theta_{nm}\left(\frac{\Lambda - \Lambda'}{u}\right) \sigma_m'^p(\Lambda'). \end{aligned} \quad (8.72)$$

Differentiating (8.70)-(8.72) we obtain coupled integral equations involving only the root densities for particles and holes

$$\rho^p(k) + \rho^h(k) = \frac{1}{2\pi} + \cos k \sum_{n=1}^{\infty} d\Lambda a_n(\Lambda - \sin k) [\sigma_n'^p(\Lambda) + \sigma_n^p(\Lambda)], \quad (8.73)$$

$$\sigma_n^h(\Lambda) = - \sum_{m=1}^{\infty} A_{nm} * \sigma_m^p \Big|_{\Lambda} + \int_{-\pi}^{\pi} dk a_n(\sin k - \Lambda) \rho^p(k), \quad (8.74)$$

$$\begin{aligned} \sigma_n'^h(\Lambda) &= \frac{1}{\pi} \operatorname{Re} \frac{1}{\sqrt{1 - (\Lambda - inu)^2}} - \sum_{m=1}^{\infty} A_{nm} * \sigma_m'^p \Big|_{\Lambda} \\ &\quad - \int_{-\pi}^{\pi} dk a_n(\sin k - \Lambda) \rho^p(k). \end{aligned} \quad (8.75)$$

Here,  $a_n(x)$  is defined in Eq. (8.13) and  $A_{nm}$  is an integral operator acting on a function  $f$  as

$$A_{nm} * f|_x = \delta_{nm} f(x) + \int_{-\infty}^{\infty} \frac{dy}{2\pi} \frac{d}{dx} \Theta_{nm} \left( \frac{x-y}{u} \right) f(y). \quad (8.76)$$

Using Eqs. (8.73)-(8.75) we describe the densities of holes in terms of the densities of particles.

We can recast (8.74) and (8.75) in a more useful form. As a preparation we indicate that the inverse of the integral operator  $A_{nm}$  is

$$A_{nm}^{-1} * f|_x = \delta_{k,n} f(x) - (\delta_{k-1,n} + \delta_{k+1,n}) \int_{-\infty}^{\infty} dy s(x-y) f(y), \quad (8.77)$$

where  $s(x)$  is given by Eq. (A.4). Acting  $A^{-1}$  on (8.74) and (8.75) we have

$$\sigma_n^p(\Lambda) = -\sigma_n^h(\Lambda) + s * \left( \sigma_{n+1}^h + \sigma_{n-1}^h \right) \Big|_{\Lambda} + \delta_{n,1} \int_{-\pi}^{\pi} dk s(\Lambda - \sin k) \rho^p(k), \quad (8.78)$$

$$\sigma_n'^p(\Lambda) = -\sigma_n'^h(\Lambda) + s * \left( \sigma_{n+1}'^h + \sigma_{n-1}'^h \right) \Big|_{\Lambda} - \delta_{n,1} \int_{-\pi}^{\pi} dk s(\Lambda - \sin k) \left( \rho^p(k) - \frac{1}{2\pi} \right). \quad (8.79)$$

**Step 2** To obtain the Gibbs free energy we need an expression for the entropy. We can describe the entropy as a function of the root densities. For instance, the number of vacancies for  $k$  in the region  $[k, k + \Delta k]$  is  $L(\rho^p(k) + \rho^h(k))\Delta k$ , where  $L\rho^p(k)\Delta k$  are occupied. Therefore, the total number of states with  $k$  lying in the region  $[k, k + \Delta k]$  is

$$\frac{(L[\rho^p(k) + \rho^h(k)]\Delta k)!}{(L\rho^p(k)\Delta k)! (L\rho^h(k)\Delta k)!}. \quad (8.80)$$

Since the corresponding entropy  $dS$  is the logarithm of (8.80), which becomes large for  $L \rightarrow \infty$ , we can use Stirling's formula to obtain  $dS$ . In this way the total entropy per site is given by

$$\begin{aligned} s &= \int_{-\pi}^{\pi} dk \{ \mathcal{L}[\rho^p(k) + \rho^h(k)] - \mathcal{L}[\rho^p(k)] - \mathcal{L}[\rho^h(k)] \} \\ &\quad + \sum_{n=1}^{\infty} \int_{-\infty}^{\infty} d\Lambda \{ \mathcal{L}[\sigma_n'^p(\Lambda) + \sigma_n'^h(\Lambda)] - \mathcal{L}[\sigma_n'^p(\Lambda)] - \mathcal{L}[\sigma_n'^h(\Lambda)] \} \\ &\quad + \sum_{n=1}^{\infty} \int_{-\infty}^{\infty} d\Lambda \{ \mathcal{L}[\sigma_n^p(\Lambda) + \sigma_n^h(\Lambda)] - \mathcal{L}[\sigma_n^p(\Lambda)] - \mathcal{L}[\sigma_n^h(\Lambda)] \}, \end{aligned} \quad (8.81)$$

where  $\mathcal{L}[f(x)] \equiv f(x) \ln[f(x)]$ . For  $B \geq 0$  and  $\mu \leq 0$  we obtain the following expression of the Gibbs free-energy functional per site

$$f(\mu, BT) = e - \mu n_c - 2Bm - Ts, \quad (8.82)$$

$$e = -2 \int_{-\pi}^{\pi} \cos k \rho(k) dk + \sum_{n=1}^{\infty} \int_{-\infty}^{\infty} 4 \operatorname{Re} \sqrt{1 - (\Lambda - inu)^2} \sigma_n^{\prime p}(\Lambda) d\Lambda, \quad (8.83)$$

$$n_c = N/L = \int_{-\pi}^{\pi} \rho(k) dk + \sum_{n=1}^{\infty} 2n \int_{-\infty}^{\infty} \sigma_n^{\prime p}(\Lambda) d\Lambda, \quad (8.84)$$

$$m = \frac{n_{\uparrow} - n_{\downarrow}}{2} = \frac{n_c}{2} - n_{\downarrow} = \frac{1}{2} \int_{-\pi}^{\pi} \rho(k) dk - \sum_{n=1}^{\infty} n \int_{-\infty}^{\infty} \sigma_n^p(\Lambda) d\Lambda. \quad (8.85)$$

Here,  $T$  is the temperature.

**Step 3** By minimizing the Gibbs free-energy functional  $f$ , we obtain the free energy at thermodynamic equilibrium. Since the hole densities are described in terms of the particle densities as (8.73)-(8.75), we have

$$\begin{aligned} 0 = \delta f &= \int_{-\pi}^{\pi} dk \left[ \frac{\delta f}{\delta \rho^p(k)} \delta \rho^p(k) + \frac{\delta f}{\delta \rho^h(k)} \delta \rho^h(k) \right] \\ &+ \sum_{n=1}^{\infty} \int_{-\infty}^{\infty} d\Lambda \left[ \frac{\delta f}{\delta \sigma_n^{\prime p}(\Lambda)} \delta \sigma_n^{\prime p}(\Lambda) + \frac{\delta f}{\delta \sigma_n^{\prime h}(\Lambda)} \delta \sigma_n^{\prime h}(\Lambda) \right] \\ &+ \sum_{n=1}^{\infty} \int_{-\infty}^{\infty} d\Lambda \left[ \frac{\delta f}{\delta \sigma_n^p(\Lambda)} \delta \sigma_n^p(\Lambda) + \frac{\delta f}{\delta \sigma_n^h(\Lambda)} \delta \sigma_n^h(\Lambda) \right]. \end{aligned} \quad (8.86)$$

Here, (8.73)-(8.75) are the variational constraints. Now we define the following ratios

$$\begin{aligned} \zeta(k) &= \rho^h(k) / \rho^p(k), \\ \eta_n(\Lambda) &= \sigma_n^h(\Lambda) / \sigma_n^p(\Lambda), \\ \eta_n'(\Lambda) &= \sigma_n^{\prime h}(\Lambda) / \sigma_n^{\prime p}(\Lambda). \end{aligned} \quad (8.87)$$

After some calculations we obtain a set of equations for these ratios

$$\begin{aligned} \ln \zeta(k) &= \frac{-2 \cos k - \mu - 2u - B}{T} \\ &+ \sum_{n=1}^{\infty} \int_{-\infty}^{\infty} d\Lambda a_n(\sin k - \Lambda) \ln \left( \frac{1 + \eta_n^{\prime -1}(\Lambda)}{1 + \eta_n^{-1}(\Lambda)} \right), \end{aligned} \quad (8.88)$$

$$\begin{aligned} \ln(1 + \eta_n(\Lambda)) &= - \int_{-\pi}^{\pi} dk \cos(k) a_n(\sin k - \Lambda) \ln(1 + \zeta^{-1}(k)) \\ &+ \frac{2nB}{T} + \sum_{m=1}^{\infty} A_{nm} * \ln \left( 1 + \frac{1}{\eta_m} \right) \Big|_{\Lambda}, \end{aligned} \quad (8.89)$$

and

$$\begin{aligned} \ln(1 + \eta'_n(\Lambda)) &= - \int_{-\pi}^{\pi} dk \cos(k) a_n(\sin k - \Lambda) \ln(1 + \zeta^{-1}(k)) \\ &+ \frac{4\text{Re}\sqrt{1 - (\Lambda - i\nu u)^2} - 2n\mu - 4\nu u}{T} + \sum_{m=1}^{\infty} A_{nm} * \ln(1 + \eta'_m)^{-1} \Big|_{\Lambda}. \end{aligned} \quad (8.90)$$

The equations (8.88)-(8.90) are called *Thermodynamic Bethe Ansatz equations* or TBA equations. In terms of solutions of the TBA equations we have a compact expression for the Gibbs free energy per site

$$\begin{aligned} f &= -T \int_{-\pi}^{\pi} \frac{dk}{2\pi} \ln(1 + \zeta^{-1}(k)) + u \\ &- T \sum_{n=1}^{\infty} \int_{-\infty}^{\infty} \frac{d\Lambda}{\pi} \ln(1 + \eta'_n)^{-1}(\Lambda) \text{Re} \frac{1}{\sqrt{1 - (\Lambda - i\nu u)^2}}. \end{aligned} \quad (8.91)$$

Using the identities given in Appendix A, this is transformed into

$$f = e_0 - T \int_{-\pi}^{\pi} dk \rho_0(k) \ln(1 + \zeta(k)) - T \int_{-\infty}^{\infty} d\Lambda \sigma_0(\Lambda) \ln(1 + \eta_1(\Lambda)), \quad (8.92)$$

where  $\sigma_0(\Lambda)$ ,  $\rho_0(k)$  and  $e_0$  are given by Eqs. (8.21), (8.22) and (8.23), respectively.

We can also recast TBA equations in a more useful form. Acting  $A^{-1}$  on (8.89) and (8.90) we have

$$\ln \eta_1(\Lambda) = s * \ln(1 + \eta_2) \Big|_{\Lambda} - \int_{-\pi}^{\pi} dk \cos(k) s(\Lambda - \sin k) \ln(1 + \zeta^{-1}(k)), \quad (8.93)$$

$$\ln \eta_n(\Lambda) = s * \ln([1 + \eta_{n-1}][1 + \eta_{n+1}]) \Big|_{\Lambda}, \quad n = 2, 3, \dots, \quad (8.94)$$

$$\ln \eta'_1(\Lambda) = s * \ln(1 + \eta'_2) \Big|_{\Lambda} - \int_{-\pi}^{\pi} dk \cos(k) s(\Lambda - \sin k) \ln(1 + \zeta(k)), \quad (8.95)$$

$$\ln \eta'_n(\Lambda) = s * \ln([1 + \eta'_{n-1}][1 + \eta'_{n+1}]) \Big|_{\Lambda}, \quad n = 2, 3, \dots. \quad (8.96)$$

Here, the convolution operation is defined by

$$s * f \Big|_x = \int_{-\infty}^{\infty} dy s(x - y) f(y), \quad (8.97)$$

where  $s(x)$  is given by Eq. (A.4). The ‘boundary conditions’ for Eqs. (8.94) and (8.96) are

$$\lim_{n \rightarrow \infty} \frac{\eta_n(\Lambda)}{n} = \frac{2B}{T}, \quad \lim_{n \rightarrow \infty} \frac{\eta'_n(\Lambda)}{n} = -\frac{2\mu}{T}. \quad (8.98)$$

Eq. (8.88) can also be recast as follows:

$$\begin{aligned} \ln \zeta(k) &= -\frac{2 \cos k}{T} - \frac{1}{T} \int_{-\infty}^{\infty} dy s(\sin k - y) \left[ 4\text{Re}\sqrt{1 - (y - i\nu)^2} \right] \\ &+ \int_{-\infty}^{\infty} dy s(\sin k - y) \ln \left( \frac{1 + \eta'_1(y)}{1 + \eta_1(y)} \right). \end{aligned} \quad (8.99)$$

To derive Eqs. (8.94), (8.96) and (8.99) we extensively used the equations of Appendix A.

### 8.4 Ha's solution to lowest order

Ha carried out the strong-coupling expansion of the TBA equations and obtained the Gibbs free energy [78] which is valid not only in the limit  $U, T \gg 1$  at fixed  $U/T$  but also for  $U \gg T$  at fixed  $T$ . In this section we review his calculation.

In order to use Eqs. (8.94) and (8.96) also for  $n = 1$ , we need to define  $\eta_0$  and  $\eta'_0$

$$\eta_0 = \exp \left[ - \int_{-\pi}^{\pi} dk \cos k \delta(\Lambda - \sin k) \ln(1 + \zeta^{-1}) \right] - 1, \quad (8.100)$$

$$\eta'_0 = \exp \left[ - \int_{-\pi}^{\pi} dk \cos k \delta(\Lambda - \sin k) \ln(1 + \zeta) \right] - 1. \quad (8.101)$$

Let us introduce a perturbation parameter  $\lambda$  and expand  $\eta_0$  as

$$\begin{aligned} \eta_0 &= -\lambda \int_{-\pi}^{\pi} dk \cos k \delta(\Lambda - \sin k) \ln(1 + \zeta^{-1}) \\ &\quad + \frac{\lambda^2}{2!} \left[ \int_{-\pi}^{\pi} dk \cos k \delta(\Lambda - \sin k) \ln(1 + \zeta^{-1}) \right]^2 \\ &\quad - \frac{\lambda^3}{3!} \left[ \int_{-\pi}^{\pi} dk \cos k \delta(\Lambda - \sin k) \ln(1 + \zeta^{-1}) \right]^3 \\ &\quad + \dots \end{aligned} \quad (8.102)$$

Then, the expansion to  $\eta_n$  can be carried out as

$$\eta_n = \eta_n^{(0)} + \lambda \eta_n^{(1)} + \lambda^2 \eta_n^{(2)} + \lambda^3 \eta_n^{(3)} + \dots \quad (8.103)$$

The expansion for  $\eta'$  is obtained from these equations with  $\ln(1 + \zeta^{-1})$  replaced by  $\ln(1 + \zeta)$ .

Substituting Eq. (8.103) into Eqs. (8.94) and (8.98), we can determine  $\eta_n^{(m)}$ . Since  $\eta_0^{(0)} = 0$ , the lowest-order equation and its boundary conditions reduce to

$$\left[ \eta_n^{(0)} \right]^2 = (1 + \eta_{n-1}^{(0)})(1 + \eta_{n+1}^{(0)}), \quad \lim_{n \rightarrow \infty} \frac{\ln \eta_n^{(0)}}{n} = \frac{2B}{T}, \quad (8.104)$$

because  $\eta_n^{(0)}$  is independent of  $\Lambda$ , and, thus, the operator  $s$  in (8.94) becomes just a factor  $1/2$ . The explicit solution to the lowest-order equation is ( $z = B/T$ )

$$\eta_n^{(0)} = \left\{ \frac{\sinh(n+1)z}{\sinh z} \right\}^2 - 1. \quad (8.105)$$

The  $m$ th-order equation can be written in general as

$$s * \Upsilon_{n+1}^{(m)} - \frac{\sinh^2(n+1)z}{\sinh n z \sinh(n+2)z} \Upsilon_n^{(m)} + s * \Upsilon_{n-1}^{(m)} = Z_n^{(m)}. \quad (8.106)$$

From Eq. (8.106), we obtain the first-order equation as

$$\Upsilon_n^{(1)} = \frac{\eta_n^{(1)}}{1 + \eta_n^{(0)}}, \quad Z_n^{(1)} = 0, \quad (8.107)$$

where the two corresponding boundary conditions are given by

$$\Upsilon_0^{(1)} = - \int_{-\pi}^{\pi} dk \cos k \delta(\Lambda - \sin k) \ln(1 + \zeta^{-1}), \quad \lim_{n \rightarrow \infty} \frac{\Upsilon_n^{(1)}}{n} = 0. \quad (8.108)$$

Now, we introduce the Fourier transform of  $\Upsilon_n(\Lambda)$  as

$$\tilde{\Upsilon}_n(\omega) = \int_{-\infty}^{\infty} d\Lambda \Upsilon_n(\Lambda) e^{i\omega\Lambda}. \quad (8.109)$$

Shifting  $n$  in Eq. (8.106) by one and carrying out the Fourier transform we obtain

$$\tilde{\Upsilon}_{n+2}^{(m)} - 2 \cosh u\omega \frac{\sinh^2(n+2)z}{\sinh(n+1) \sinh(n+3)z} \tilde{\Upsilon}_{n+1}^{(m)} + \tilde{\Upsilon}_n^{(m)} = \tilde{Q}_n^{(m)}, \quad (8.110)$$

where  $\tilde{Q}_n^{(m)} = 2 \cosh(u\omega) \tilde{Z}_{n+1}^{(m)}$ . The solution to the homogeneous part of the equation is

$$\tilde{\Upsilon}_n^{h(m)} = A^+(\omega) \tilde{\Upsilon}_n^+ + A^-(\omega) \tilde{\Upsilon}_n^-, \quad (8.111)$$

where  $A^\pm$  are some functions of  $\omega$  and

$$\tilde{\Upsilon}_n^\pm = \frac{\sinh nz}{\sinh(n+1)z} e^{\pm(n+2)u|\omega|} - \frac{\sinh(n+2)z}{\sinh(n+1)z} e^{\pm nu|\omega|}. \quad (8.112)$$

The full solution to Eq. (8.110) is

$$\tilde{\Upsilon}_n^{(m)} = \tilde{\Upsilon}_n^{h(m)} + \tilde{\Upsilon}_n^- \sum_{j=0}^{n-1} \frac{\tilde{\Upsilon}_{j+1}^+}{K_0} \tilde{Q}_j^{(m)} - \tilde{\Upsilon}_n^+ \sum_{j=0}^{n-1} \frac{\tilde{\Upsilon}_{j+1}^-}{K_0} \tilde{Q}_j^{(m)}, \quad (8.113)$$

where  $K_0 = \tilde{\Upsilon}_0^+ \tilde{\Upsilon}_1^- - \tilde{\Upsilon}_0^- \tilde{\Upsilon}_1^+$ . We can determine the constants by imposing the boundary conditions.

The solution to Eq. (8.110) for  $m = 1$  is

$$\tilde{\Upsilon}_n^{(1)} = \frac{\sinh z}{\sinh 2z} \left[ \frac{\sinh z}{\sinh(n+1)z} \int_{-\pi}^{\pi} dk \cos k e^{i\omega \sin k - (n+2)u|\omega|} \ln(1 + \zeta^{-1}) - \frac{\sinh(n+2)z}{\sinh(n+1)z} \int_{-\pi}^{\pi} dk \cos k e^{i\omega \sin k - nu|\omega|} \ln(1 + \zeta^{-1}) \right]. \quad (8.114)$$

The solutions for  $\eta'$  are also obtained by Eq. (8.114) with  $z$  and  $\zeta^{-1}$  replaced by  $z' (\equiv -\mu/T)$  and  $\zeta$ .

After the inverse Fourier transformation we obtain  $\Upsilon_n^{(1)}$  and  $\Upsilon_n'^{(1)}$  as follows:

$$\Upsilon_n^{(1)} = -G + \frac{1}{4 \cosh^2 z} \Delta G, \quad (8.115)$$

$$\Upsilon_n'^{(1)} = -G + \frac{4}{T} (\text{Re} \sqrt{1 - (\Lambda - iu)^2} - u) + \frac{1}{4 \cosh^2 z'} \left[ \Delta G - \int_{-\pi}^{\pi} dk \frac{2 \cos^2 k}{T} \Delta a \right], \quad (8.116)$$

where

$$G = \int_{-\pi}^{\pi} dk \cos k a_1 (\Lambda - \sin k) \ln(1 + \zeta^{-1}), \quad (8.117)$$

$$\Delta G = \int_{-\pi}^{\pi} dk \cos k \Delta a \ln(1 + \zeta^{-1}), \quad (8.118)$$

$$\Delta a = \int_{-\infty}^{\infty} \frac{d\omega}{2\pi} 2 \cosh(u\omega) e^{-2u|\omega| + i\omega(\Lambda - \sin k)}. \quad (8.119)$$

Restricting to  $\mathcal{O}(U^{-2})$ , i.e., approximating the kernel as  $a_n \approx 1/(n\pi u)$ , finally we have the following expression for the Gibbs free energy per site ( $U \gg \sin k$ ):

$$f = f^{(0)} + f^{(1)} + \dots \quad (8.120)$$

The  $\lambda$ -expansion can be sorted in terms of  $(U^{-n})f_n(1/T, U/T, \mu/T)$  if  $U \gg \sin k$ . The expansion for  $f$  in Eq. (8.120) is the reorganized  $\lambda$ -expansion.

Ha [78] used the expansion for  $U, T \gg 1$  at fixed  $U/T$  to verify the expansion for the Gibbs free energy  $f$  comparing with the expansion series given by Liu [84], and to compare other thermodynamic quantities like the magnetic susceptibility, specific heat, etc. with the numerical calculations by Kawakami *et al.* [85]. In the next chapter, we derive his expansions more compactly for  $\mu = B = 0$ , and study the limit  $U \gg T \gg t^2/U$  in more detail.

## 9 Solution in the spin-disordered limit

As explained in Chap. 7, the Mott–Hubbard transition in the single-band Hubbard model at half band-filling in infinite dimensions continues to pose an intriguing problem. Especially, the determination of the precise value of the critical interaction  $U_c$  is an unsolved problem. Therefore, it is desirable to have an example of a Hubbard-type model with a disordered spin background which can be solved exactly.

In this chapter, we analyze the TBA equations in the spin-disordered limit using Ha’s approach to solve the recursion equations in Sec. 8.4. Then, we calculate the internal energy and the effective dispersion of the charge degrees of freedom. Lastly, we interpret these results in terms of a putative interacting-electron system at zero temperature.

### 9.1 Defining equations

In this section, we first explain the spin-disordered limit more precisely. Then, we apply the limit to the TBA equations which are derived in last chapter. From these results, we can further obtain exact expressions in the spin-disordered limit, such as the dressed energy and the dressed momentum of the charge degrees of freedom, the effective dispersion for strong coupling, and the internal energy.

#### 9.1.1 Definition of the limit

We consider the TBA equations in the limit

$$J \ll T \ll \Delta \quad (9.1)$$

for  $B = 0$  and  $\mu = 0$ , i.e., the Hubbard chain at half band-filling.  $J(U/t \rightarrow \infty) = 4t^2/U$  is the coupling strength for the spin degrees of freedom, and  $\Delta$  is the gap for charge excitations,  $\Delta(U/t \rightarrow \infty) = U - 4t$ . In this limit, the spin degrees of freedom are ‘hot’, i.e., the charge degrees of freedom move in a random spin background.

The qualitative dependence of the internal energy as a function of temperature is shown in Fig. 9.1. In the temperature range given by (9.1) the internal energy is essentially independent of temperature because the spin degrees of freedom contribute maximally to the internal energy whereas there are exponentially few charge excitations. For the spin-disordered limit (9.1), the expansions for  $\zeta(k)$ ,  $\eta(\Lambda)$  and  $\eta'(\Lambda)$  considerably simplify.

#### Charge sector

We define the *dressed energy* for charge excitations by

$$\kappa(k, u, T) = T \ln(\zeta(k)). \quad (9.2)$$

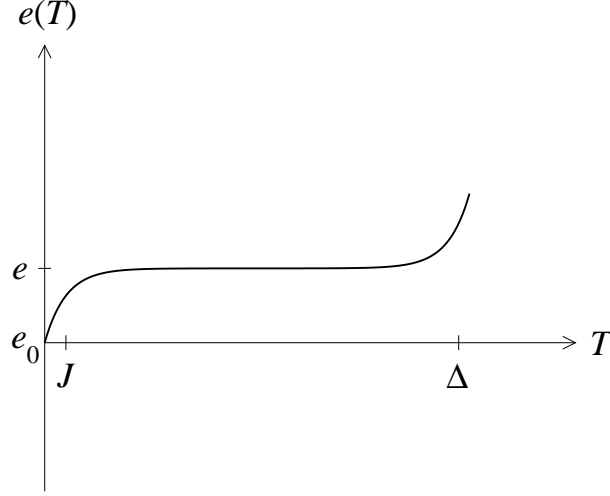


Fig. 9.1: Internal energy as a function of temperature for the Hubbard model at half band-filling and large interactions.

We will see that, in the spin-disordered regime, the dressed energy has an expansion of the form

$$\kappa(k, u, T) = \sum_{m=0}^{\infty} \left( \frac{1}{uT} \right)^m \kappa^{(m)} + \mathcal{O}(e^{-u/T}). \quad (9.3)$$

The leading term in this expression is temperature independent, negative and of order  $\mathcal{O}(u)$ . Hence

$$\zeta(k) = \mathcal{O}(e^{-u/T}) \ll 1, \quad (9.4)$$

$$\ln(1 + \zeta^{-1}(k)) = -\ln(\zeta(k)) + \mathcal{O}(e^{-u/T}). \quad (9.5)$$

Eq. (9.5) leads to a significant simplification of the TBA equations.

### **$k$ - $\Lambda$ Strings**

Neglecting terms of order  $\mathcal{O}(e^{-u/T})$ , the TBA equations (8.95) and (8.96) for  $k$ - $\Lambda$  strings take the form

$$\ln \eta'_n(\Lambda) = s * \ln(1 + \eta'_{n+1})(1 + \eta'_{n-1}) \Big|_{\Lambda}, \quad n = 1, 2 \dots, \quad (9.6)$$

where  $\eta'_0(\Lambda) = 0$  from Eq. (8.101). The solution to (9.6) under the boundary conditions (8.98) with  $\mu = 0$  [86] is

$$\eta'_n(\Lambda) = (n+1)^2 - 1. \quad (9.7)$$

The corrections to  $\eta'$  are of order  $\exp(\exp(-u/T))$ .

### $\Lambda$ Strings

Neglecting terms of order  $\mathcal{O}(e^{-u/T})$ , the TBA equations (8.93) and (8.94) for  $\Lambda$  strings take the form

$$\ln \eta_n(\Lambda) = s * \ln(1 + \eta_{n+1})(1 + \eta_{n-1})|_{\Lambda}, \quad n = 1, 2 \dots, \quad (9.8)$$

where  $\eta_0(\Lambda)$  is obtained from Eq. (8.100) as

$$\eta_0(\Lambda) = \exp\left(-\frac{4}{T} \operatorname{Re} \sqrt{1 - \Lambda^2}\right) - 1. \quad (9.9)$$

The solution to (9.8) under the boundary conditions (8.98) with  $B = 0$  can be obtained by iterative linearization, as shown in Sec. 8.4. The starting point is the solution  $\eta_n^{(0)}$  to the Eqs. (9.8) with  $\eta_0^{(0)} = 0$ , i.e.,

$$\eta_n^{(0)}(\Lambda) = (n + 1)^2 - 1. \quad (9.10)$$

One then linearizes (9.8) around the solution (9.10) by writing  $\eta_n = \eta_n^{(0)} + \eta_n^{(1)}$  and keeping only the terms linear in  $\eta_n^{(1)}$ . This gives the following set of linear integral equations, see Eqs. (8.106) and (8.107),

$$s * \Upsilon_{n+1}^{(1)} - \frac{(n+1)^2}{n(n+1)} \Upsilon_n^{(1)} + s * \Upsilon_{n-1}^{(1)} = 0, \quad \Upsilon_n^{(1)} = \frac{\eta_n^{(1)}}{1 + \eta_n^{(0)}}. \quad (9.11)$$

The boundary conditions are given by (8.98) and

$$\Upsilon_0^{(1)} = \eta_0^{(1)} = -\frac{4}{T} \operatorname{Re} \sqrt{1 - \Lambda^2}. \quad (9.12)$$

The set of linear integral equations (9.11) can be solved by Fourier transform as in Sec. 8.4. We find

$$\begin{aligned} \tilde{\Upsilon}_n^{(1)} &= \frac{1}{T(n+1)} \left[ n \int_{-\pi}^{\pi} dk \cos^2 k e^{i\omega \sin k} e^{-u(n+2)|\omega|} \right. \\ &\quad \left. - (n+2) \int_{-\pi}^{\pi} dk \cos^2 k e^{i\omega \sin k} e^{-un|\omega|} \right]. \end{aligned} \quad (9.13)$$

By inverse Fourier transforming Eq. (9.13) and using (A.2), we obtain

$$\begin{aligned} \eta_n^{(1)}(\Lambda) &= \frac{n+1}{T} \left[ n \int_{-\pi}^{\pi} dk \cos^2(k) a_{n+2}(\sin k - \Lambda) \right. \\ &\quad \left. - (n+2) \int_{-\pi}^{\pi} dk \cos^2(k) a_n(\sin k - \Lambda) \right] \\ &= \frac{2n(n+1)}{T} \operatorname{Re} \left[ \sqrt{1 - \{\Lambda - iu(n+2)\}^2} \right] \\ &\quad - \frac{2(n+1)(n+2)}{T} \operatorname{Re} \left[ \sqrt{1 - (\Lambda - iu)^2} \right] = \mathcal{O}\left(\frac{1}{uT}\right). \end{aligned} \quad (9.14)$$

Here we used (A.14) in the second equality. We see that we have

$$|\eta_1^{(1)}(\Lambda)| \ll \eta_1^{(0)}(\Lambda) = 3, \quad (9.15)$$

as required.

### 9.1.2 Dressed energy of the charge degrees of freedom

Combining the results for  $\eta_1(\Lambda)$  and  $\eta'_1(\Lambda)$  we obtain

$$\ln \left[ \frac{1 + \eta'_1(\Lambda)}{1 + \eta_1(\Lambda)} \right] \approx -\frac{1}{4} \eta_1^{(1)}(\Lambda). \quad (9.16)$$

Substituting this back into (8.99) and using (A.8) and (A.14), we obtain the first term of the expansion (9.3)

$$\kappa^{(0)}(k, u) = -2 \cos k - 2u - \frac{1}{2} \int_{-\infty}^{\infty} \frac{d\omega}{\omega} J_1(\omega) e^{i\omega \sin k} e^{-2u|\omega|}. \quad (9.17)$$

Crucially, the contributions of  $\eta_1$  and  $\eta'_1$  to  $\zeta(k)$  do not feed back into the integral equations for  $\eta_n$  and  $\eta'_n$ . The reasons for this are that

- (i) the corrections do not change the fact that  $\ln(\zeta)$  is of the order of  $u$  and terms involving  $\ln(1 + \zeta(k))$  can therefore be dropped from the TBA equations;
- (ii) The corrections to  $\ln(\zeta)$  depend only on  $\sin(k)$  and therefore do not contribute to

$$\int_{-\pi}^{\pi} dk \cos(k) s(\Lambda - \sin k) \ln \zeta(k). \quad (9.18)$$

Note that we also derived this result from Ha's equations (8.115)-(8.119) in the last chapter. The result (9.17) should be compared to the corresponding expression at zero temperature, see Eq. (7.10) of Ref. [5],

$$\kappa_0(k, u) = -2 \cos k - 2u - 2 \int_{-\infty}^{\infty} \frac{d\omega}{\omega} J_1(\omega) e^{i\omega \sin k} \frac{1}{1 + \exp(2|\omega|u)}. \quad (9.19)$$

Performing the integral in (9.17) we finally find ( $u = U/4$ )

$$\kappa^{(0)}(k, U) = \epsilon(k) - \frac{1}{2\sqrt{2}} \sqrt{[\epsilon(k)]^2 + U^2 + \sqrt{[\epsilon(k)^2 - U^2]^2 + (4U)^2}}, \quad (9.20)$$

where  $\epsilon(k) = -2 \cos k$  is the bare dispersion.

The interesting point is that  $\kappa^{(0)}(k) \neq \kappa_0(k)$  despite the fact that  $T \ll |\kappa_0(k)|$ . The reason for this is that spin and charge degrees of freedom are still coupled in the Hubbard model, as is obvious from the TBA equations and also from the known scattering matrix of elementary excitations [87], see Sec. 5.4 in Ref. [5]. We note that the modification of the dressed energy of the charge degrees of freedom by the spin sector is a general characteristic of the spin-disordered regime. In the asymptotic low-energy regime, spin and charge degrees of freedom decouple quite generically for one-dimensional interacting-electron systems. However, on the scale of the temperature in the spin-disordered regime such a decoupling no longer holds. This in turn is expected to lead to modifications in non-universal physical properties such as the charge velocity. Our result is in agreement with this expectation which we note equally applies to a less than half-filled band.

### 9.1.3 Dressed momentum of the charge degrees of freedom

The total momentum in thermal equilibrium is equal to zero by virtue of translational invariance. In order to determine the dressed momentum of our charge excitation, we start from the expression for the contribution of a charge excitation with real  $ks$  to the total momentum [88]

$$p(k) = k + \sum_{n=1}^{\infty} \int_{-\infty}^{\infty} d\Lambda \theta \left( \frac{\sin k - \Lambda}{nu} \right) [\sigma_n^p(\Lambda) + \sigma_n^h(\Lambda)] , \quad (9.21)$$

where  $\theta(x) = 2 \arctan(x)$ . The root densities for particles and holes with the ratios (8.87) obey Eqs. (8.73), (8.78), and (8.79). In addition, (8.78), and (8.79) can be recast as

$$\sigma_n^p(\Lambda) = -\sigma_n^h(\Lambda) + s * (\sigma_{n+1}^h + \sigma_{n-1}^h)|_{\Lambda} , \quad n = 1, 2, \dots , \quad (9.22)$$

and likewise for the primed distributions. Here,  $\sigma_0^h$  and  $\sigma_0^p$  are defined by the following equations

$$s * \sigma_0^h|_{\Lambda} = \int_{-\pi}^{\pi} dk s(\Lambda - \sin k) \rho^p(k) , \quad (9.23)$$

$$s * \sigma_0^p|_{\Lambda} = \int_{-\pi}^{\pi} dk s(\Lambda - \sin k) \left( \rho^p(k) - \frac{1}{2\pi} \right) . \quad (9.24)$$

As  $\zeta(k) = \mathcal{O}(\exp(-u/T))$  we can drop  $\rho^h(k)$  from Eq. (8.73) and substitute the resulting equation into (9.23) and (9.24). We obtain the following result:

$$s * \sigma_0^h|_{\Lambda} = \int_{-\pi}^{\pi} \frac{dk}{2\pi} s(\Lambda - \sin k) = \sigma_0(\Lambda) , \quad s * \sigma_0^p|_{\Lambda} = 0 . \quad (9.25)$$

The temperature-independent contribution to the particle and hole root densities is obtained by using (9.7) and (9.10) and then solving the resulting sets of coupled linear integral equations. We find  $\sigma_n^p = \sigma_n^h = \mathcal{O}(\exp(-u/T))$  and

$$s * \sigma_{n+1}^h - \frac{(n+1)^2}{n(n+2)} \sigma_n^h + s * \sigma_{n-1}^h = 0 \quad (9.26)$$

with the boundary condition

$$\sigma_0^h(\Lambda) = \frac{1}{\pi} \operatorname{Re} \frac{1}{\sqrt{1 - \Lambda^2}} . \quad (9.27)$$

Using Ha's approach in Sec. 8.4 to solve the recursion equation (9.26), we obtain

$$\begin{aligned} \sigma_n^p(\Lambda) &= \int_{-\infty}^{\infty} \frac{d\omega}{2\pi} \frac{J_0(\omega) e^{-i\omega\Lambda}}{2(n+1)} \left[ \frac{e^{-nu|\omega|}}{n} - \frac{e^{-(n+2)u|\omega|}}{n+2} \right] + \mathcal{O}(\exp(-u/T)) \\ &= -\frac{1}{2\pi(n+1)(n+2)} \left( \frac{1}{\sqrt{1 - (\Lambda - i(n+2)u)^2}} \right) \\ &\quad + \frac{1}{2\pi n(n+1)} \operatorname{Re} \left( \frac{1}{\sqrt{1 - (\Lambda - inu)^2}} \right) + \mathcal{O}(\exp(-u/T)) . \end{aligned} \quad (9.28)$$

Substituting this back into (9.21) we obtain the temperature-independent contribution to the dressed momentum

$$p(k) = k + \frac{1}{2} \arcsin \left[ \frac{2 \sin k}{\sqrt{4u^2 + (\sin k + 1)^2} + \sqrt{4u^2 + (\sin k - 1)^2}} \right]. \quad (9.29)$$

We note that the physical momenta of holons ( $h$ ) and anti-holons ( $\bar{h}$ ) are obtained from  $p(k)$  by  $p_h(k) = \pi/2 - p(k) = p_{\bar{h}} + \pi$ .

#### 9.1.4 Effective dispersion for strong coupling

The effective dispersion is given implicitly by Eqs. (9.20) and (9.29). In order to have a consistent expansion for the Hubbard model in the spin-disordered regime, we need to truncate these two equations at order  $1/u$  because the next subleading temperature-dependent contributions are of the order  $1/(uT)$ . Hence, the effective dispersion in the spin-disordered Hubbard model is given by

$$\kappa^{(0)}(p, u) = -2u - 2 \cos p - \frac{1}{4u} (3 - 2 \cos^2 p) + \mathcal{O}(u^{-2}). \quad (9.30)$$

For the Hubbard model at zero temperature we find instead

$$\kappa_0(p, u) = -2u - 2 \cos p - \frac{\ln 2}{u} (3 - 2 \cos^2 p) + \mathcal{O}(u^{-2}). \quad (9.31)$$

Both formulae can be cast into the form

$$\kappa(p, u, T) = -2u - 2 \cos p - \frac{1}{4u} (1 - 4\gamma_s(T)) (3 - 2 \cos^2 p) + \mathcal{O}(u^{-2}), \quad (9.32)$$

where

$$\gamma_s(T) = \langle \hat{\mathbf{S}}_i \hat{\mathbf{S}}_{i+1} \rangle_s \quad (9.33)$$

denotes the nearest-neighbor spin correlation function in the Heisenberg model at temperature  $T$ . Thermal averages of operators  $\hat{A}$  over spin configurations are defined by

$$\langle \hat{A} \rangle_s = \frac{\text{Tr} \left[ \exp \left( -\beta \hat{\mathcal{H}}_{\text{Heis}} \right) \hat{A} \right]}{\text{Tr} \left[ \exp \left( -\beta \hat{\mathcal{H}}_{\text{Heis}} \right) \right]} \quad (9.34)$$

with the Heisenberg Hamiltonian

$$\hat{\mathcal{H}}_{\text{Heis}} = \sum_i \frac{4t^2}{U} \left( \hat{\mathbf{S}}_i \hat{\mathbf{S}}_{i+1} - \frac{1}{4} \right). \quad (9.35)$$

In fact, we have  $\gamma_s(T=0) = 1/4 - \ln(2)$  from the Bethe-ansatz solution of the Heisenberg model [89] (see also Eq. (6.83) of Ref. [5]) and  $\gamma_s(T=\infty) = 0$  for uncorrelated spins.

The result (9.32) can be obtained within the  $1/U$ -expansion [65]. This approach can be used here because the one-dimensional lattice is a Bethe lattice with coordination number  $Z = 2$ . To leading order in  $1/u$  we must treat the Hamiltonian

$$\hat{h}_1 = -\frac{1}{U} \hat{P}_0 \hat{T} \hat{P}_1 \hat{T} \hat{P}_0, \quad (9.36)$$

where  $\hat{P}_0$  projects onto the subspace of zero double occupancies. At half band-filling,  $\hat{h}_1$  reduces to the Heisenberg model (9.35). The internal energy density of the Heisenberg model is given by

$$e_s(T) = \frac{1}{u} \left( \gamma_s(T) - \frac{1}{4} \right), \quad (9.37)$$

and can be calculated analytically in terms of the Thermodynamic Bethe Ansatz [80, 86] or, equivalently, via the solution of a set of coupled integral equations [90].

For the derivation of the effective dispersion we have to solve (see (43) of [65])

$$\begin{aligned} \frac{U}{L} \sum_{j,\sigma} \left\langle \hat{c}_{j,\sigma}^\dagger \left( \hat{h}_1 - L e_s(T) \right) \hat{c}_{j,\sigma} \right\rangle_s &= \frac{1}{L} \sum_{j,\sigma} \left\langle \hat{c}_{j,\sigma}^\dagger \left[ g_{1,2} (\hat{h}_0)^2 + g_{1,0} \right] \hat{c}_{j,\sigma} \right\rangle_s \\ &= 2g_{1,2} + g_{1,0}, \end{aligned} \quad (9.38)$$

where  $\hat{h}_0$  describes the hopping of holes in the spin background,  $\hat{h}_0 = \hat{P}_0 \hat{T} \hat{P}_0$ . The expectation value on the left-hand-side of (9.38) is readily calculated so that we find

$$-8 \left( \gamma_s(T) - \frac{1}{4} \right) = 2g_{1,2} + g_{1,0} \quad (9.39)$$

as our first equation. The second equation we obtain from the solution of Eq. (44) of [65],

$$\begin{aligned} \frac{U}{L} \sum_{j,\sigma} \left\langle \hat{c}_{j,\sigma}^\dagger \left( \hat{h}_1 - L e_s(T) \right) (\hat{h}_0)^2 \hat{c}_{j,\sigma} \right\rangle_s &= \frac{1}{L} \sum_{j,\sigma} \left\langle \hat{c}_{j,\sigma}^\dagger \left[ g_{1,2} (\hat{h}_0)^2 + g_{1,0} \right] (\hat{h}_0)^2 \hat{c}_{j,\sigma} \right\rangle_s \\ &= 6g_{1,2} + 2g_{1,0}. \end{aligned} \quad (9.40)$$

The expectation value on the left-hand-side of (9.40) is readily calculated and we find

$$4 \left( \gamma_s(T) - \frac{1}{4} \right) = 2g_{1,2} \quad (9.41)$$

as our second equation. From this  $g_{1,2} = -(1 - 4\gamma_s(T))/2$  and  $g_{1,0} = 3(1 - 4\gamma_s(T))$  result, and the effective Hamiltonian for the motion of a single hole in a spin background becomes

$$\hat{h}^{\text{eff}} = \hat{h}_0 + (1 - 4\gamma_s(T)) \frac{(-\hat{h}_0)^2/2 + 3}{U} + \mathcal{O}(U^{-2}). \quad (9.42)$$

Replacing  $\hat{h}_0 \rightarrow -\epsilon(p) = 2 \cos p$  and  $\omega + 2u = -\hat{h}^{\text{eff}}$  as in [65] we find for  $\kappa(p, u, T) \equiv \omega$

$$\kappa(p, u, T) = -2u - 2 \cos p - \frac{1}{4u} (1 - 4\gamma_s(T)) (3 - 2 \cos^2 p) + \mathcal{O}(u^{-2}), \quad (9.43)$$

as used in (9.30).

From the  $1/U$ -expansion we can determine the density of states of the lower Hubbard band. As in [65] the shape-correction factor to first order is found to be

$$S(\epsilon) = 1 - \frac{(1 - 4\gamma_s(T))\epsilon}{U} \quad (9.44)$$

so that we find  $(\alpha(T) = (1 - 4\gamma_s(T)))$

$$\begin{aligned} D_{\text{LHB}}^{(1)}(\omega) &= \int_{-2}^2 d\epsilon \rho_0(\epsilon) \left(1 - \alpha(T) \frac{\epsilon}{U}\right) \delta\left(\omega + U/2 + \epsilon + \alpha(T) \frac{6 - \epsilon^2}{2U}\right) \\ &= \rho_0 \left[ \left( U - \sqrt{(1 + \alpha(T))U^2 + 2\alpha(T)U\omega + 6\alpha(T)^2} \right) / \alpha(T) \right], \end{aligned} \quad (9.45)$$

where

$$\rho_0(\epsilon) = \frac{1}{\pi\sqrt{4 - \epsilon^2}} \quad \text{for } |\epsilon| < 2 \quad (9.46)$$

is the density of states for non-interacting electrons and  $\omega_- < \omega < \omega_+$  with  $\omega_{\pm} = -U/2 \pm 2 - \alpha(T)/U$ .  $D_{\text{LHB}}^{(1)}(\omega')$  is shown in Fig. 9.2 as a function of  $\omega' (\equiv \omega + U/2 + 1/U)$  for  $U/t = 10$  and  $T = \infty$ . In particular, for the single-particle gap we find

$$\Delta^{(1)}(u, T) = -2\omega_+ = 4u - 4 + \frac{1 - 4\gamma_s(T)}{2u}, \quad (9.47)$$

Finally, we note that the momentum distribution can also be determined along these lines. We find

$$\langle \hat{n}_p \rangle_s = \sum_{\sigma} \langle \hat{n}_{p\sigma} \rangle_s = 1 - \frac{\cos p}{2u} (1 - 4\gamma_s(T)) + \mathcal{O}(u^{-2}), \quad (9.48)$$

in agreement with Eq. (3.2) of Ref. [67].

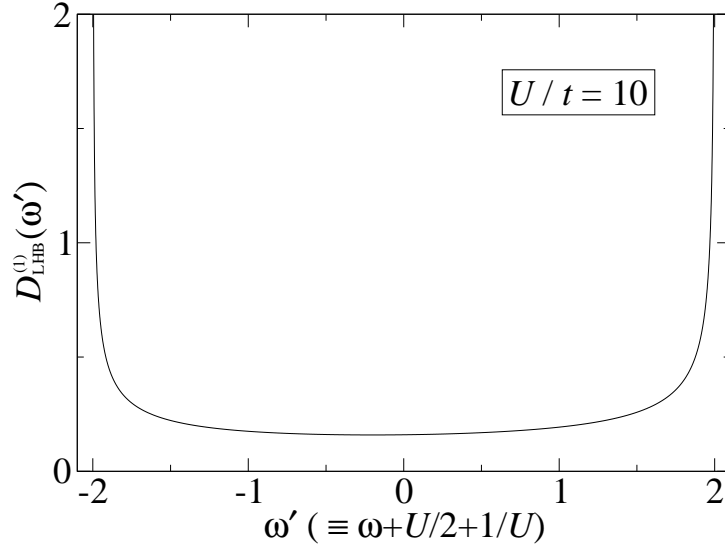


Fig. 9.2: Density of states of the lower Hubbard band, Eq. (9.45), as a function of  $\omega' (\equiv \omega + U/2 + 1/U)$  for  $U/t = 10$  in the spin-disordered regime.

### 9.1.5 Internal energy

The free-energy density (8.92) can be recast with the help of (8.99) into the form (see Eq. (4.21) of [78])

$$f(T) \equiv C - T\alpha(T) - T\beta(T), \quad (9.49)$$

$$C = 4 \int_{-\infty}^{\infty} d\Lambda \sigma_0(\Lambda) \operatorname{Re} \left[ \sqrt{1 - (\Lambda - iu)^2} \right] - u - \mu = -e_0 - \mu, \quad (9.50)$$

$$\alpha(T) = \int_{-\pi}^{\pi} dk \rho_0(k) \ln(1 + 1/\zeta(k)), \quad (9.51)$$

$$\beta(T) = \int_{-\infty}^{\infty} d\Lambda \sigma_0(\Lambda) \ln(1 + \eta'_1(\Lambda)). \quad (9.52)$$

With the help of (9.49) the internal energy

$$e(T, u) = f(T) - T \frac{\partial f(T)}{\partial T} \quad (9.53)$$

can be expressed as

$$e(T, u) = C + T^2 \left( \frac{\partial \alpha(T)}{\partial T} + \frac{\partial \beta(T)}{\partial T} \right). \quad (9.54)$$

We must evaluate (9.54) in the spin-disordered limit. We have

$$e_\alpha \equiv T^2 \frac{\partial \alpha}{\partial T} \approx \int_{-\pi}^{\pi} dk \rho_0(k) \kappa^{(0)}(k, u), \quad (9.55)$$

$$e_\beta \equiv T^2 \frac{\partial \beta}{\partial T} = 0. \quad (9.56)$$

The latter follows from the fact that  $\eta'_1$  is independent of temperature. From (9.17) and (9.55) we obtain

$$e_\alpha = e_0 - u - \int_0^\infty \frac{d\omega}{\omega} J_0(\omega) J_1(\omega) \exp(-2u\omega). \quad (9.57)$$

Finally, from (9.54) and (9.50) we find  $e(T, u) \equiv e(u)$  as

$$e(u) = -u - \int_0^\infty \frac{d\omega}{\omega} J_0(\omega) J_1(\omega) \exp(-2u\omega), \quad (9.58)$$

which is to be compared to the ground-state energy of the Hubbard model at half band-filling

$$e_0(u) = -u - 4 \int_0^\infty \frac{d\omega}{\omega} J_0(\omega) J_1(\omega) \frac{1}{1 + \exp(2u\omega)}. \quad (9.59)$$

The expression (9.58) can be simplified further,

$$e(u) = -\frac{2u}{\pi} \operatorname{EllipticE} \left( -\frac{1}{u^2} \right). \quad (9.60)$$

Here,  $\text{EllipticE}(m)$  is the complete elliptic integral of the second kind,

$$\text{EllipticE}(m) = \int_0^{\pi/2} d\theta \sqrt{1 - m \sin^2 \theta}. \quad (9.61)$$

From the internal energy we can derive the average double occupancy

$$\begin{aligned} d(u) &= \frac{1}{4} + \frac{1}{4} \frac{\partial e(u)}{\partial u}, \\ &= \frac{1}{4} - \frac{1}{2\pi} \text{EllipticK} \left( -\frac{1}{u^2} \right). \end{aligned} \quad (9.62)$$

Here,  $\text{EllipticK}(m)$  is the complete elliptic integral of the first kind. The corresponding result for the Hubbard model at zero temperature follows from the derivative of (9.59) with respect to the interaction strength.

## 9.2 Zero-temperature interpretation

Now we *interpret* our results in terms of a putative one-dimensional interacting-electron system at zero temperature. In practice, we use the results for the temperature-independent contributions to the internal energy and the effective dispersion derived for the spin-disorder regime in the Hubbard model,  $J \ll T \ll \Delta$ , for *any* value of  $U$ .

### 9.2.1 Mott–Hubbard transition

The one-dimensional Hubbard model at half band-filling describes a Mott–Hubbard insulator for all  $U > 0$ , i.e., the gap  $\Delta_0(U)/2$  for single-particle charge excitations is finite,  $\Delta_0(U) = -2\kappa_0(\pm\pi, U)$ . Using Eq. (9.19) we obtain again

$$\Delta_0(U) = 2 \left[ -2 + \frac{U}{2} + 4 \int_0^\infty \frac{d\omega}{\omega} J_1(\omega) \frac{1}{1 + \exp(\omega U/2)} \right], \quad (9.63)$$

which is equal to Eq. (8.30). We have a finite gap,  $\Delta_0(U) > 0$ , for all  $U > 0$ .

In our putative interacting-electron system umklapp scattering processes are rendered ineffective by the random spin background which, at zero energy cost, provides a mechanism to dissipate momentum in scattering processes involving charge degrees of freedom. Therefore, we expect that the charge gap will open at a critical interaction strength. Indeed, from (9.17) and (9.20) we find

$$\Delta(U) = 2 \left[ -2 + \frac{U}{2} + \int_0^\infty \frac{d\omega}{\omega} J_1(\omega) \exp(-\omega U/2) \right] = -4 + \sqrt{U^2 + 4}. \quad (9.64)$$

The gap opens linearly with slope  $\sqrt{3}/2$  at

$$U_c = 2\sqrt{3} = \frac{\sqrt{3}}{2} W \approx 0.866W, \quad (9.65)$$

where  $W = 4$  is the bandwidth of the Hubbard model. The gap is shown in Fig. 9.3.

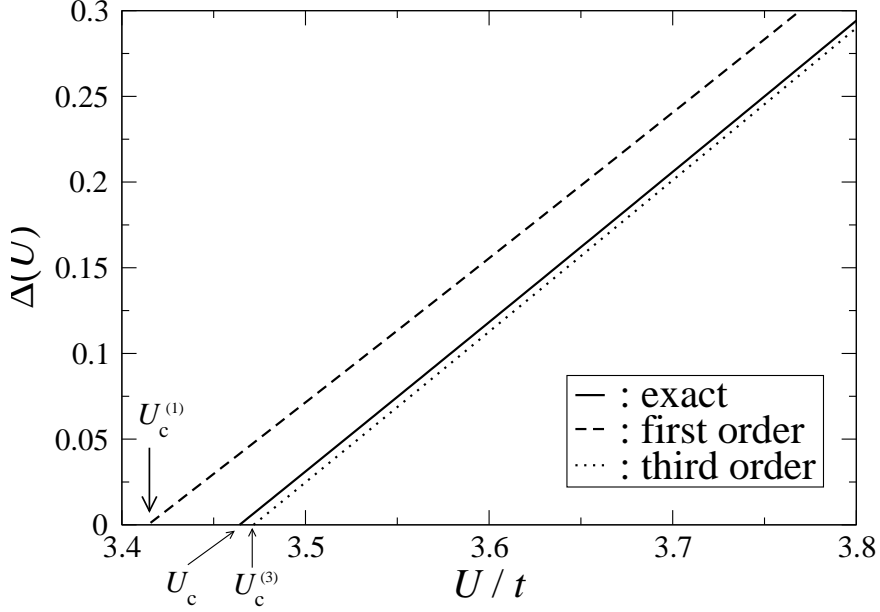


Fig. 9.3: Gap for single-particle excitations as a function of the interaction strength  $U$  for the putative interacting-electron system with a disordered spin background at half band-filling.

### 9.2.2 Average double occupancy

The analysis above shows that the approximation (9.4) finally breaks down at  $U_c$ . Therefore, we can expect that physical quantities such as the average double occupancy display unphysical behavior in the region  $U < U_c$ . In fact,  $d(u)$  contains a term proportional to  $u \ln(u)$  so that its derivative diverges logarithmically for  $u \rightarrow 0$ . This diverging slope is seen in Fig. 9.4 where we compare the average double occupancy of the interacting-electron system with a spin-disordered background with the double occupancy of the Hubbard model.

### 9.2.3 Strong-coupling expansions

The internal energy of the Hubbard model at zero temperature and in the spin-disordered case can be expanded in powers of  $1/U$ . In both cases, the radius of convergence is given by  $U_R^e = 4$ , see (6.83) of [5] for  $e_0(u)$  and (17.3.12) of [91] for  $e(u)$ .

Explicitly,

$$\begin{aligned} [e(U) + U/4]/U &= \sum_{m=1}^{\infty} a_{2m} U^{-2m} \\ &= -\frac{1}{U^2} + \frac{3}{U^4} - \frac{20}{U^6} + \frac{175}{U^8} - \frac{1764}{U^{10}} + \frac{19404}{U^{12}} \pm \dots, \end{aligned} \quad (9.66)$$

where  $a_{2m}$  is described by

$$a_{2m} = \frac{(-1)^m 2^{2m-2} (2m-1)!! (2m-3)!!}{(m!)^2}. \quad (9.67)$$

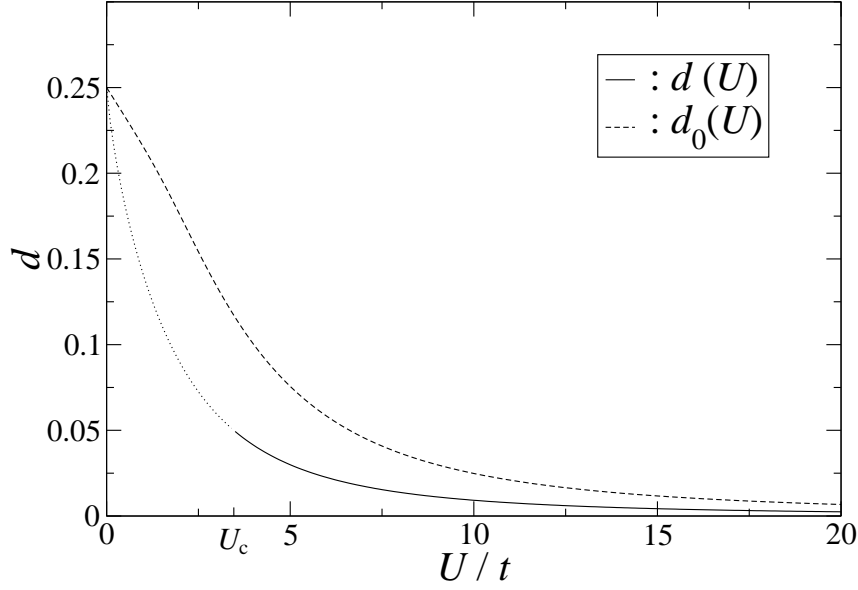


Fig. 9.4: Average double occupancy  $d_0(U)$  of the Hubbard model at half band-filling as compared to  $d(U)$  (9.62) for the putative interacting-electron system with a spin-disordered background.

In (9.37) we determined the coefficient  $a_2 = -1$  within the  $1/U$ -expansion. From the coefficients  $a_{2m}$ , one may actually deduce the radius of convergence of the series, as done in [68], by extrapolating the ratio of the coefficients  $r(m) = |a_{2m}/a_{2m-2}|$  ( $m \geq 2$ ) for  $m \rightarrow \infty$ . In our case  $r(m) = 4(2m-1)(2m-3)/m^2$  is a second-order polynomial in  $1/m$  and we correctly find

$$U_R^e = \lim_{m \rightarrow \infty} \left( \sqrt{r(m)} \right) = 4. \quad (9.68)$$

Note, however, that the radius of convergence of the energy is not related to the critical interaction strength of the metal-insulator transition,  $U_c = 2\sqrt{3}$ . Therefore, it may also be doubted that this approach [68] is justified for the case of the infinite-dimensional Hubbard model.

In contrast to the internal energy, the series expansion of the gap in the spin-disordered Hubbard model converges for  $U > U_R^{\text{gap}} = 2$ . The first terms of the expansion read

$$\Delta(U) = \sum_{m=-1}^{\infty} b_m U^{-m} = U - 4 + \frac{2}{U} - \frac{2}{U^3} \pm \dots \quad (9.69)$$

In (9.47) we determined the coefficients  $b_{-1} = 1$ ,  $b_0 = 4$ , and  $b_1 = 2$  within the  $1/U$ -expansion.

Now that  $U_c = 2\sqrt{3}$  is larger than the convergence radius of the series,  $U_R^{\text{gap}} = 2$ , the gap opens linearly and the first few orders of the  $1/U$ -expansion provide a very accurate description of the gap, as shown in Fig. 9.3. This is particularly true for the critical values

for the closing of the gap as inferred from the truncated  $1/U$ -expansion. Let us denote by  $\Delta^{(m)}(U)$  the  $m$ th-order truncation of the series, e.g.,

$$\begin{aligned}\Delta^{(0)}(U) &= U - 4, \\ \Delta^{(1)}(U) &= U - 4 - 2/U, \\ \Delta^{(3)}(U) &= U - 4 - 2/U - 2/U^3, \\ &\vdots\end{aligned}$$

Furthermore, let  $U_c^{(m)}$  be the critical interaction strength at which the  $m$ th gap opens,  $\Delta^{(m)}(U_c^{(m)}) = 0$ . We then find

$$\begin{aligned}U_c^{(0)} &= 4, \\ U_c^{(1)} &= 3.4142[1.4\%], \\ U_c^{(3)} &= 3.4717[0.2\%], \\ &\vdots \\ U_c &= 2\sqrt{3} = 3.4651.\end{aligned}\tag{9.70}$$

The numbers in square brackets give the percentage difference to  $U_c$ . It is seen that the series converges very fast to the exact value. This observation supports the application of this approach to the Hubbard model in infinite dimensions [65, 66]. We think that  $1/U$  expansion for the gap of the Mott–Hubbard insulator in infinite dimensions is equally reliable. This supports the value  $U_{c,1} \simeq 4.5t$  in the Hubbard model on a Bethe lattice with infinite connectivity.



## 10 Conclusions

In the second part of this thesis, we analyzed the Thermodynamic Bethe Ansatz equations for the half-filled one-dimensional Hubbard model in the spin-disordered regime. We motivated our investigations by two case studies, the single-band Hubbard model at half band-filling in infinite dimensions and the Harris–Lange model. The determination of the precise value of the critical interaction  $U_c$  at the Mott–Hubbard metal-insulator transition of the former model is still unsolved as various DMFT treatments lead to conflicting results. Therefore, we provide an example of a Hubbard-type model with a disordered spin background which can be solved exactly.

Starting from the TBA equations, we provided a compact reformulation of Ha’s approach to solve the recursion equations. We derived explicit expressions for the leading terms in the dressed energy, the dressed momentum, and the effective dispersion of the charge degrees of freedom. When interpreted in terms of a putative one-dimensional model at zero temperature, we found that the gap opens linearly at  $U_c = 2\sqrt{3}$  which is larger than the convergence radius of the series,  $U_R^{\text{gap}} = 2$ , and the first few orders of the  $1/U$ -expansion provide a good description of the gap. In contrast to that, the radius of convergence of the ground-state energy is only  $U_R^e = 4$  so that no conclusions about  $U_c$  can be drawn from a  $1/U$ -expansion of the ground-state energy of this Mott–Hubbard insulator. We believe that this observation also applies to the Mott–Hubbard insulator in infinite dimensions.



# 11 Summary and Outlook

## 11.1 Summary

In this thesis, we investigated one-dimensional strongly correlated electron systems using exact numerical and analytical methods.

In part I, we developed an accurate numerical method based on the DMRG to calculate the Tomonaga–Luttinger parameter  $K_\rho$  for generic quasi one-dimensional metallic systems. Another new method which is based on ED and DMRG works well but is less accurate. We demonstrated the accuracy of our DMRG approach by comparing our data with Bethe-ansatz results for spinless fermions and the one-dimensional Hubbard model and with predictions from field theory. Experiments indicate that the TLL parameter  $K_\rho$  is small,  $K_\rho < 0.2$ , in some quasi one-dimensional materials. Our detailed theoretical investigations show that neither a pure onsite interaction (Hubbard model) nor an additional dimerization (Peierls–Hubbard model) alone can account for  $K_\rho < 1/2$ . Instead, small values of  $K_\rho$  can only be obtained for slightly doped charge-density-wave insulators, i.e., within an extended (Peierls–)Hubbard model.

In part II, we analyzed the Thermodynamic Bethe Ansatz equations of the one-dimensional half-filled Hubbard model in the spin-disordered regime, which is characterized by the temperature being much larger than the magnetic energy scale but small compared to the Mott–Hubbard gap. We derived explicit expressions for the leading terms in the dressed energy and momentum of the charge degrees of freedom and the internal energy. The resulting effective dispersion of holons differs from the corresponding result in the half-filled Hubbard model at zero temperature. This effect is due to the coupling of charge and spin degrees of freedom and occurs at the expected energy scale. We then interpreted the entire temperature-independent part of the effective dispersion and the internal energy in terms of a putative interacting-electron system at zero temperature. From these results we find that strong-coupling expansions for the Mott–Hubbard insulator have a larger radius of convergence for the gap than for the ground-state energy, i.e., the critical interaction strength for the transition in the infinite-dimensional Hubbard model should be estimated from the  $1/U$ -expansion of the gap but not of the ground-state energy. Moreover, our exact analytical results provide a bench-mark test for approximate analytical and numerical techniques at finite temperatures.

## 11.2 Outlook

We end this thesis by giving an outlook on future developments.

### 11.2.1 $K_\rho$ -problem

In this work, we have concentrated on the band-fillings  $n = 2/m$  for even  $m$ . When  $m$  is odd, we should have  $K_\rho^* = 3/m^2$  and  $K_\rho^{\text{CDW}} = 1/(2m^2)$  according to field theory [17]. Therefore, we expect that in the  $t$ - $U$ - $V_1$ - $V_2$  model at  $n = 2/3$  we obtain  $K_\rho^* = 1/3$  and

$K_\rho^{\text{CDW}} = 1/18$ . Again, in the slightly doped system we could obtain very small values for  $K_\rho$  near  $n = 2/3$ . This situation could correspond to TTF-TCNQ, which has a band-filling  $n \approx 0.59$ , i.e., it has a doping of 8%. Starting from  $K_\rho^{\text{CDW}} = 1/18 \approx 0.06$  at infinitesimal doping, a value  $K_\rho(\delta = 0.08) < 0.17$  and, thus,  $\alpha \geq 1$ , appears to be within reach.

The extended Peierls–Hubbard model at quarter filling also has interesting physical properties [92–94]. In the presence of dimerization, the metallic region for  $t = t_1 = t_2$  in Fig. 5.6 changes into the Mott insulating state and the  $4k_{\text{F}}$ -CDW insulating region is slightly suppressed. Since dimerization reduces the values for  $K_\rho$  in general, it could be possible to obtain small TLL parameters  $K_\rho$  for intermediate interaction strengths in the slightly doped system.

Finally, we note that our method can also be applied to ladder systems. So far, a number of groups have tried to calculate the properties for  $K_\rho$  in ladder systems, e.g., see Ref. [19] and references therein. However, the accuracy of the studies is not satisfactory. Our new method makes it possible to investigate  $K_\rho$  quantitatively also for ladder systems.

### 11.2.2 Charges in a spin-disordered system

In this thesis, we obtained the leading term in the Hubbard model with a disordered spin background. It would be a natural extension to derive the next order in  $1/(UT)$ . For example, it is interesting to see how strongly the term in second order decreases the value of the critical interaction strength  $U_c$ .

Moreover, a detailed comparison of our analytical results with those from other methods is desirable. For instance, G. Jüttner *et al.* investigated the finite-temperature properties of the one-dimensional Hubbard model using a path-integral approach [95, 96], see also Chap. 13 of Ref. [5]. Their approach is independent of the string hypothesis behind the TBA equations and gives very accurate data for all physical quantities at finite temperature. Therefore, the method would provide an independent check of our results. In addition, our result can be used to assess the quality of approximate schemes which describe the effective charge dispersion in a random spin background, see, e.g., Ref. [97].

Finally, it would be desirable to compare our result with experiments. A one-dimensional optical lattice, essentially an artificial crystal of light [98], when filled with fermionic atoms could be a conceivable realization of our model system.

## A Mathematical Appendices

In this appendix, we list a number of useful formulae which we used in this thesis. We closely follow the list in chapter 17 of Ref. [5]. Some formulae are from Ref. [99].

### A.1 Symmetric integration

For any integrable function  $f(x)$  we have

$$\int_{-\pi}^{\pi} dk \cos k f(\sin k) = 2 \int_0^{\pi} \cos k f(\sin k) = 0. \quad (\text{A.1})$$

### A.2 Fourier transforms

For  $a > 0$  we have the following Fourier transforms:

$$\int_{-\infty}^{\infty} \frac{dx}{2\pi} \exp(-i\omega x) \frac{2a}{a^2 + x^2} = \exp(-a|\omega|), \quad (\text{A.2})$$

$$\int_{-\infty}^{\infty} \frac{dx}{2\pi} \frac{\exp(-i\omega x)}{2 \cosh ax} = \frac{1}{4a \cosh(\omega\pi/2a)}. \quad (\text{A.3})$$

### A.3 Identities involving the integral kernels

The definitions of the functions  $s(x)$ ,  $R(x)$ ,  $a_n(x)$ ,  $A_{nm}(x)$  are the following:

$$s(x) = \frac{1}{4u \cosh(\pi x/2u)} = \frac{1}{2\pi} \int_{-\infty}^{\infty} d\omega \frac{\exp(-i\omega x)}{2 \cosh(\omega u)}, \quad (\text{A.4})$$

$$R(x) = \int_{-\infty}^{\infty} \frac{d\omega}{2\pi} \frac{\exp(i\omega x)}{1 + \exp(2u|\omega|)}, \quad (\text{A.5})$$

$$a_n(x) = \frac{1}{2\pi} \frac{2nu}{(nu)^2 + x^2}. \quad (\text{A.6})$$

The following identities hold:

$$\begin{aligned} & \sum_{n=1}^{\infty} \int_{-\infty}^{\infty} dy A_{kn}^{-1}(x-y) \left( 4\text{Re} \sqrt{1 - (y - inu)^2} - 2n\mu - 4nu \right) \\ &= \delta_{k,1} \int_{-\pi}^{\pi} dk 2 \cos^2(k) s(x - \sin k). \end{aligned} \quad (\text{A.7})$$

$$\int_{-\infty}^{\infty} dy s(x-y)[a_{m-1}(y) + a_{m+1}(y)] = a_m(x). \quad (\text{A.8})$$

$$\sum_{n=1}^{\infty} \int_{-\infty}^{\infty} dy A_{kn}^{-1}(x-y) a_n(y - \sin k) = \delta_{k,1} s(x - \sin k). \quad (\text{A.9})$$

$$\int_{-\infty}^{\infty} d\Lambda a_1(x - \Lambda) s(\Lambda - y) = R(x - y). \quad (\text{A.10})$$

$$\int_{-\infty}^{\infty} d\Lambda a_1(x - \Lambda) [\delta(\Lambda - y) - R(\Lambda - y)] = s(x - y). \quad (\text{A.11})$$

#### A.4 Bessel functions

$$J_n(z) = \frac{1}{2\pi} \int_{-\pi}^{\pi} d\theta \exp(iz \sin \theta - in\theta). \quad (\text{A.12})$$

$$\int_{-\pi}^{\pi} dk \cos^2(k) \exp(i\omega \sin k) = \frac{2\pi J_1(\omega)}{\omega}. \quad (\text{A.13})$$

#### A.5 Useful relations

$$4\text{Re}\sqrt{1 - (\Lambda - inu)^2} - 4nu = \int_{-\pi}^{\pi} \frac{dk}{\pi} \frac{\cos^2 k(2nu)}{(nu)^2 + (\sin k - \Lambda)^2}, \quad u > 0. \quad (\text{A.14})$$

$$\int_{-\infty}^{\infty} \frac{d\mu}{2\pi} \frac{2a}{a^2 + (\lambda - \mu)^2} \frac{2b}{b^2 + (\mu - \nu)^2} = \frac{2(a+b)}{(a+b)^2 + (\lambda - \nu)^2}, \quad a, b > 0. \quad (\text{A.15})$$

$$2\text{Re}\frac{1}{\sqrt{1 - (\Lambda - ia)^2}} = \int_{-\pi}^{\pi} \frac{dk}{2\pi} \frac{2a}{a^2 + (\Lambda - \sin k)^2}, \quad a > 0. \quad (\text{A.16})$$

$$\arctan(z) = \frac{1}{2i} \ln \left( \frac{1+iz}{1-iz} \right). \quad (\text{A.17})$$

#### A.6 $k$ - $\Lambda$ string for two electrons

Here, we summarize the deviation of Eq. (8.37). From Eq. (8.35) and (8.36) we have

$$\sin(k_{\pm}) = \sin(q \pm i\xi) = \Lambda \mp iu + \mathcal{O}(e^{-\xi L}). \quad (\text{A.18})$$

Neglecting the exponential term, we have

$$\sin(q \pm i\xi) = \sin(q) \cosh(\xi) \pm i \cos(q) \sinh(\xi) = \Lambda \mp iu. \quad (\text{A.19})$$

Eq. (A.18) has two possible solutions:

- From the lowest branch of  $\arcsin(x)$ , we have

$$q \pm i\xi = \arcsin(\Lambda \mp iu), \quad -\frac{\pi}{2} \leq q \leq \frac{\pi}{2}. \quad (\text{A.20})$$

Since  $\cos(q) \geq 0$  and  $\xi > 0$ , we obtain  $u < 0$ .

- From the first branch of  $\arcsin(x)$ , we have

$$q \pm i\xi = \pi - \arcsin(\Lambda \mp iu), \quad \frac{\pi}{2} \leq q \leq \frac{3\pi}{2}. \quad (\text{A.21})$$

Since  $\cos(q) \leq 0$  and  $\xi > 0$ , we obtain  $u > 0$ .

Therefore, we conclude that the solution of Eq. (A.18) depends on the sign of interaction strength  $u$ :

$$k_{\pm} = \arcsin(\Lambda \mp iu), \quad \text{for } u < 0, \quad (\text{A.22})$$

$$k_{\pm} = \pi - \arcsin(\Lambda \mp iu), \quad \text{for } u > 0. \quad (\text{A.23})$$



## Bibliography

- [1] J. G. Bednorz and K. A. Müller, *Z. Phys. B* **64**, 189 (1986).
- [2] J. Hubbard, *Proc. R. Soc. London, Ser. A* **276**, 238 (1963).
- [3] N. F. Mott, *Metal-Insulator Transitions*, 2nd edition (Taylor & Francis, London, 1990).
- [4] F. Gebhard, *The Mott Metal-Insulator Transition* (Springer, Berlin, 1997).
- [5] F. H. L. Essler, H. Frahm, F. Göhmann, A. Klümper and V. Korepin, *The One-Dimensional Hubbard Model* (Cambridge University Press, Cambridge, 2005).
- [6] M. Nakamura, *J. Phys. Soc. Jpn.* **68**, 3123 (1999); *Phys. Rev. B* **61**, 16377 (2000).
- [7] M. Tsuchiizu and A. Furusaki, *Phys. Rev. Lett.* **88**, 056402 (2002); *Phys. Rev. B* **69**, 035103 (2004).
- [8] E. Jeckelmann, *Phys. Rev. Lett.* **89**, 236401 (2002); *ibid.* **91**, 089702 (2003).
- [9] A. W. Sandvik, L. Balents and D. K. Campbell, *Phys. Rev. Lett.* **92**, 236401 (2004).
- [10] F. Mila and X. Zotos, *Europhys. Lett.* **24**, 133 (1993).
- [11] K. Sano and Y. Ōno, *Phys. Rev. B* **70**, 155102 (2004).
- [12] P. Schmitteckert and R. Werner, *Phys. Rev. B* **69**, 195115 (2004).
- [13] D. Jérôme and H. J. Schulz, *Adv. Phys.* **31**, 299 (1982).
- [14] J. Sólyom, *Adv. Phys.* **28**, 209 (1979).
- [15] K. Schönhammer, *Phys. Rev. B* **63**, 245102 (2001).
- [16] T. Giamarchi and A. J. Millis, *Phys. Rev. B* **46**, 9325 (1992).
- [17] H. J. Schulz, *Strongly Correlated Electronic Materials*, edited by K. S. Bedell, Z. Wang and D. E. Meltzer (Addison-Wesley, New York, 1994) p. 187; cond-mat/9412036.
- [18] T. Giamarchi, *Physica B* **230-232**, 975 (1997).
- [19] T. Giamarchi, *Quantum Physics in One Dimension* (Clarendon Press, Oxford, 2004).
- [20] S. Iijima, *Nature* **354**, 56 (1991); S. Iijima, T. Ichihashi, and Y. Ando, *Nature* **356**, 776 (1992).
- [21] S. Iijima and T. Ichihashi, *Nature* **363**, 603 (1993).

- [22] D. S. Bethune, C. H. Kiang, M. S. de Vries, G. Gorman, R. Savoy, J. Vazquez and R. Beyers, *Nature* **363**, 605 (1993).
- [23] H. Ishii, H. Katsura *et al.*, *Nature* **426**, 540 (2003).
- [24] S. J. Tans, M. H. Devoret, H. Dai, A. Thess, R. E. Smalley, L. J. Geerligs and C. Dekker, *Nature* **386**, 474 (1997).
- [25] R. Egger and A. O. Gogolin, *Europ. Phys. J. B* **3**, 281 (1998).
- [26] V. Vescoli, L. Degiorgi, W. Henderson, G. Grüner, K. P. Starkey and L. K. Montgomery, *Science* **281**, 1181 (1998); A. Schwartz *et al.*, *Phys. Rev. B* **58**, 1261 (1998).
- [27] L. Ducasse, M. Abderrabba *et al.*, *J. Phys. C* **19**, 3805 (1986).
- [28] T. Giamarchi, *Phys. Rev. B* **44**, 2905 (1991).
- [29] F. Zwick, S. Brown, G. Margaritondo, C. Merlic, M. Onellion, J. Voit and M. Grioni, *Phys. Rev. Lett.* **79**, 3982 (1997).
- [30] R. Claessen, M. Sing, U. Schwingenschlögl, P. Blaha, M. Dressel and C. S. Jacobsen, *Phys. Rev. Lett.* **88**, 096402 (2002); M. Sing *et al.*, *Phys. Rev. B* **68**, 125111 (2003).
- [31] S. Kagoshima, H. Hasegawa and T. Sambongi, *One Dimensional Conductors* (Springer, Berlin, 1987).
- [32] F. Zwick, D. Jérôme, G. Margaritondo, M. Onellion, J. Voit and M. Grioni, *Phys. Rev. Lett.* **81**, 2974 (1998).
- [33] C. Lanczos, *J. Res. Nat. Bur. Stand.* **45**, 255 (1950).
- [34] T. Sebe and J. Nachamkin, *Ann. Phys.* **51**, 100 (1969).
- [35] H. Q. Lin, *Phys. Rev. B* **42**, 6561 (1990).
- [36] E. Dagotto, *Rev. Mod. Phys.* **66**, 763 (1994).
- [37] S. R. White, *Phys. Rev. Lett.* **69**, 2863 (1992); *Phys. Rev. B* **48**, 10345 (1993).
- [38] *Density-Matrix Renormalization*, edited by I. Peschel, X. Wang, M. Kaulke and K. Hallberg (Springer, Berlin, 1999).
- [39] U. Schollwöck, *Rev. Mod. Phys.* **77**, 259 (2005).
- [40] R. M. Noack, *The Density Matrix Renormalization Group: Method and Application to Strongly Interacting Electron Systems*, Habilitationsschrift (Fribourg, Switzerland, 1999).
- [41] W. H. Press, B. P. Flannery, S. A. Teukolsky and W. T. Vetterling, *Numerical Recipes: The Art of Scientific Computing* (Cambridge University Press, Cambridge, 1987).
- [42] E. Jeckelmann and S. R. White, *Phys. Rev. B* **57**, 6376 (1998).

- [43] E. R. Davidson, *J. Comp. Phys* **17**, 87 (1975); *Computers in Physics* **7**, No. 5, 519 (1993).
- [44] E. Jeckelmann, F. Gebhard and F. H. L. Essler, *Phys. Rev. Lett.* **85**, 3910 (2000).
- [45] E. Jeckelmann, *Phys. Rev. B* **66**, 045114 (2002).
- [46] E. Jeckelmann, *Dynamical Density-Matrix Renormalization Group*, Habilitationsschrift (Marburg, 2002).
- [47] S. Ejima, F. Gebhard, S. Nishimoto and Y. Ohta, *Phys. Rev. B* **72**, 033101 (2005).
- [48] H. J. Schulz, *Phys. Rev. Lett.* **64**, 2831 (1990).
- [49] N. Kawakami and S.-K. Yang, *Phys. Lett. A* **148**, 359 (1990).
- [50] H. Frahm and V. E. Korepin, *Phys. Rev. B* **42**, 10553 (1990).
- [51] H. Seo and M. Ogata, *Phys. Rev. B* **64**, 113103 (2001).
- [52] S. Nishimoto and Y. Ohta, *Phys. Rev. B* **68**, 235114 (2003).
- [53] A. K. Zhuravlev, M. I. Katsnelson and A. V. Trefilov, *Phys. Rev. B* **56**, 12939 (1997); A. K. Zhuravlev and M. I. Katsnelson, *ibid.* **61**, 15534 (2000).
- [54] S. Ejima, F. Gebhard and S. Nishimoto, *Europhys. Lett.* **70**, 492 (2005).
- [55] M. Dzierzawa, *The Hubbard Model*, edited by D. Baeriswyl, D. K. Campbell, J. M. P. Carmelo, F. Guinea and E. Louis NATO ASI Series B 343 (Plenum Press, New York, 1995) p. 327.
- [56] S. Daul and R. M. Noack, *Phys. Rev. B* **58**, 2635 (1998).
- [57] R. T. Clay, A. W. Sandvik and D. K. Campbell, *Phys. Rev. B* **59**, 4665 (1999).
- [58] V. Meden, W. Metzner, U. Schollwöck and K. Schönhammer, *Phys. Rev. B* **65**, 045318 (2002).
- [59] S. Andergassen, T. Enss, V. Meden, W. Metzner, U. Schollwöck and K. Schönhammer, *Phys. Rev. B* **70**, 075102 (2004).
- [60] T. Enss, Ph. D. thesis, Universität Stuttgart (2005); cond-mat/0504703.
- [61] S. Andergassen, T. Enss, V. Meden, W. Metzner, U. Schollwöck and K. Schönhammer, *Phys. Rev. B* **73**, 045125 (2006).
- [62] K. Penc and F. Mila, *Phys. Rev. B* **50**, 11429 (1994).
- [63] S. Nishimoto, M. Takahashi and Y. Ohta, *J. Phys. Soc. Jpn.* **69**, 1594 (2000); See also S. Nishimoto and Y. Ohta, *Physica C* **282-287**, 1911 (1997).
- [64] E. Economou, *Greens Functions in Quantum Physics*, 2nd edition (Springer, Berlin, 1983).

- [65] M. P. Eastwood, F. Gebhard, E. Kalinowski, S. Nishimoto and R. M. Noack, *Europ. Phys. J. B* **35**, 155 (2003).
- [66] S. Nishimoto, F. Gebhard and E. Jeckelmann, *J. Phys. Cond. Matt* **16**, 7063 (2004).
- [67] M. Takahashi, *J. Phys. C* **10**, 1289 (1977).
- [68] N. Blümer and E. Kalinowski, *Phys. Rev. B* **71**, 195102 (2005).
- [69] E. Kalinowski, private communication (2004).
- [70] R. Bulla, *Phys. Rev. Lett.* **83**, 136 (1999); R. Bulla, T. A. Costi and D. Vollhardt, *Phys. Rev. B* **64**, 045103 (2001).
- [71] D. J. García, K. Hallberg and M. J. Rozenberg, *Phys. Rev. Lett.* **93**, 246403 (2004).
- [72] R. M. Noack and F. Gebhard, *Phys. Rev. Lett.* **82**, 1915 (1999).
- [73] A. B. Harris and R. V. Lange, *Phys. Rev.* **157**, 295 (1967).
- [74] F. Gebhard, K. Bott, M. Scheidler, P. Thomas and S. W. Koch, *Phil. Mag. B* **75**, 13 (1997).
- [75] S. K. Lyo and J.-P. Gallinar, *J. Phys. C* **10**, 1963 (1977).
- [76] E. H. Lieb and F. Y. Wu, *Phys. Rev. Lett.* **20**, 1445 (1968).
- [77] M. Takahashi, *Prog. Theor. Phys.* **47**, 69 (1972).
- [78] Z. N. C. Ha, *Phys. Rev. B* **46**, 12205 (1992).
- [79] N. Kawakami and S.-K. Yang, *Conformal field theory and one-dimensional quantum systems* (Iwanami Shoten, Tokyo, in Japanese, 1997).
- [80] M. Takahashi, *Thermodynamics of one-dimensional solvable models* (Cambridge University Press, Cambridge, 1999).
- [81] A. A. Ovchinnikov, *Zh. Eksp. Teor. Fiz.* **57**, 2137 (1969); [*Sov. Phys. JETP* **30**, 1160 (1970)].
- [82] K. Schönhammer, O. Gunnarsson and R. M. Noack, *Phys. Rev. B* **52**, 2504 (1995).
- [83] F. H. L. Essler, V. E. Korepin and K. Schoutens, *Nucl. Phys. B* **384**, 431 (1992).
- [84] K. L. Liu, *Can. J. Phys.* **62**, 361 (1984).
- [85] N. Kawakami, T. Usuki and A. Okiji, *Phys. Lett. A* **137**, 287 (1989).
- [86] M. Takahashi, *Prog. Theor. Phys.* **46**, 401 (1971).
- [87] F. H. L. Essler and V. E. Korepin, *Phys. Rev. Lett.* **72**, 908 (1994); *Nucl. Phys. B* **426**, 505 (1994).
- [88] F. Woynarovich, *J. Phys. C* **15**, 97 (1982); *ibid.*, 6397 (1982).

- [89] H. Bethe, *Z. Phys.* **71**, 205 (1931).
- [90] A. Klümper, *Z. Phys.* **91**, 507 (1993).
- [91] M. Abramovitz and I. A. Stegun, *Handbook of Mathematical Functions* (Dover, New York, 1972).
- [92] H. Yoshioka, M. Tsuchiizu and Y. Suzumura, *J. Phys. Soc. Jpn.* **69**, 651 (2000).
- [93] M. Tsuchiizu, H. Yoshioka and Y. Suzumura, *J. Phys. Soc. Jpn.* **70**, 1460 (2001).
- [94] Y. Shibata, S. Nishimoto and Y. Ohta, *Phys. Rev. B* **64**, 235107 (2001).
- [95] G. Jüttner, A. Klümper and J. Suzuki, *Nucl. Phys.* **522**, 471 (1998).
- [96] A. Klümper, *Lect. Notes Phys.* **645**, 349 (2004).
- [97] A. Reischl, E. Müller-Hartmann and G. S. Uhrig, *Phys. Rev. B* **70**, 245124 (2004).
- [98] M. Köhl, H. Moritz, T. Stöferle, K. Günter and T. Esslinger, *Phys. Rev. Lett.* **94**, 080403 (2005).
- [99] I. S. Gradshteyn and I. M. Ryzhik, *Table of Integrals, Series, and Products*, edited by A. Jeffrey (Academic Press, New York, 1965).



## Danksagung

An erster Stelle danke ich sehr herzlich meinem Doktorvater Herrn Prof. Dr. Florian Gebhard. Er hat mich während meiner Promotion in jeder Hinsicht unterstützt und gefördert. Ohne seinen warmherzigen Beistand wäre diese Arbeit nicht möglich gewesen.

Besonders danke ich Herrn Dr. Satoshi Nishimoto, mit dem ich seit Beginn meiner Doktorarbeit zusammengearbeitet habe. Er stand mir stets freundschaftlich mit Rat und Tat zur Seite.

Herrn Dr. Fabian Eßler bin ich sehr verbunden für die Einladung an die Universität Oxford und für die intensive und freundliche Betreuung. Ein wesentlicher Teil dieser Arbeit ging aus diesen gemeinsamen Bemühungen hervor.

Herrn Prof. Dr. Peter Thomas danke ich sehr herzlich für die Übernahme des Zweitgutachtens und für seinen aufmunternden Zuspruch.

Bei der “Honjo International Scholarship Foundation” bedanke ich mich für die Gewährung eines Promotionsstipendiums, wodurch sich mir die einmalige Gelegenheit bot, drei Jahre als Doktorand in Deutschland zu verbringen. Die im Rahmen des Graduiertenkollegs “Electron-Electron Interactions in Solids” veranstalteten Seminare in Ráckeve, Riezlern und Marburg waren für mich ein schönes Erlebnis.

Vieles was ich über numerische Vielteilchenmethoden in den vergangenen drei Jahren gelernt habe, verdanke ich den beiden Meistern dieses Faches, Herrn Prof. Dr. Eric Jeckelmann und Herrn Prof. Dr. Reinhard Noack. Ich habe viel von unseren gemeinsamen Diskussionen und Projekten profitiert.

Bei allen Mitgliedern der Arbeitsgruppen Vielteilchenphysik möchte ich mich für die freundliche Atmosphäre und die stets vorhandene Hilfsbereitschaft bedanken.

Desweiteren bedanke ich mich bei allen meinen Freunden und vor allem bei meiner Familie für ihren langjährigen Rückhalt. Und schließlich danke ich ganz besonders Tomoko Taguchi für ihre liebe Unterstützung während meiner Promotion.



## Curriculum Vitae

Name	Satoshi Ejima
Nationality	Japanese
Date of birth	12 October 1977
Place of birth	Saitama, Japan

### Studies

05/2005 – 07/2005	Research visit, Oxford University, with Dr. F. H. L. Eßler
04/2003 – 03/2006	Studies of physics, Philipps-Universität Marburg
03/2003	Masters degree in physics, Chiba University, Japan <i>Anomalous physical properties associated with charge ordering in low-dimensional strongly correlated electron systems</i> with Prof. Dr. Y. Ohta
04/2001 – 03/2003	Studies of physics, Chiba University, Japan
03/2001	Bachelors degree in physics, Chiba University, Japan
04/2000 – 03/2001	Studies of physics, Chiba University, Japan
04/1999 – 03/2000	Studies of physics, Georg-August-Universität Göttingen
04/1996 – 03/1999	Studies of physics, Chiba University, Japan

### Scholarship

04/2003 – 03/2006	Honjo International Scholarship Foundation
-------------------	--